Lawrence Berkeley National Laboratory
Recent Work

Title
Ion Beam Synthesis of SiGe Alloy Layers

Permalink
https://escholarship.org/uc/item/7bh2c45t

Author
Im, S.

Publication Date
1994-04-01

eScholarship.org
Powered by the California Digital Library
University of California

LBL-35580
UC-404

Lawrence Berkeley Laboratory

UNIVERSITY OF CALIFORNIA

Materials Sciences Division

Ion Beam Synthesis of SiGe Alloy Layers

S. Im
(Ph.D. Thesis)

May 1994

LOAN COPY
Circulates
for 4 weeks
Bldg. 50 Library.
Copy 2
LBL-35580

Prepared for the U.S. Department of Energy under Contract Number DE-AC03-76SF00098

DISCLAIMER

This document was prepared as an account of work sponsored by the United States Government. While this document is believed to contain correct information, neither the United States Government nor any agency thereof, nor the Regents of the University of California, nor any of their employees, makes any warranty, express or implied, or assumes any legal responsibility for the accuracy, completeness, or usefulness of any information, apparatus, product, or process disclosed, or represents that its use would not infringe privately owned rights. Reference herein to any specific commercial product, process, or service by its trade name, trademark, manufacturer, or otherwise, does not necessarily constitute or imply its endorsement, recommendation, or favoring by the United States Government or any agency thereof, or the Regents of the University of California. The views and opinions of authors expressed herein do not necessarily state or reflect those of the United States Government or any agency thereof or the Regents of the University of California.

LBL-35580
UC-404

Ion Beam Synthesis of SiGe Alloy Layers

Seongil Im
Ph.D. Thesis

Dept. of Materials Science & Mineral Engineering
University of California

and

Materials Science Division
Lawrence Berkeley Laboratory
University of California
Berkeley, CA 94720

May, 1994

This work was supported in part by the Director, Office of Energy Research, Office of Basic Energy Sciences, Materials Science Division of the U.S. Department of Energy under Contract No. DE-AC03-76SF00098.

Ion Beam Synthesis of SiGe Alloy Layers

Copyright © 1994

by

Seongil Im

The U.S. Department of Energy has the right to use this thesis for any purpose whatsoever including the right to reproduce all or any part thereof

recycled paper

Abstract

Ion Beam Synthesis of SiGe Alloy Layers

by

Seongil Im

Doctor of Philosophy in

Engineering-Materials Science and Mineral Engineering

University of California at Berkeley

Professor Ronald Gronsky, Chair

A systematic study of the processing procedures required for minimizing structural defects generated during the ion beam synthesis (IBS) of SiGe alloy layers has been performed. The synthesis of 200 nm thick SiGe alloy layers by implantation of Ge ions with an incident energy of 120 keV into <100> oriented Si wafers yielded various Ge peak concentrations after the following doses, $2x10^{16}cm^{-2}$, $3x10^{16}cm^{-2}$, and $5x10^{16}cm^{-2}$. Following implantation, SPE annealing in a nitrogen ambient at 800°C for 1 hour resulted in only slight redistribution of the implanted Ge. Two kinds of extended defects were observed in alloy layers synthesized at doses over $3x10^{16}cm^{-2}$ at room temperature: end-of-range (EOR) dislocation loops and strain-induced stacking faults. The density of EOR dislocation loops was much lower in those alloys produced by liquid nitrogen temperature (LNT) implantation than by room temperature (RT) implantation. Decreasing the implantation dose to obtain 5 at% peak Ge concentration prevents strain relaxation, while those SPE layers with more than 7 at% Ge peak show high densities of misfit-

induced stacking faults. Sequential implantation of C following high dose ($5x10^{16}/cm^2$) Ge implantation (12 at% Ge peak concentration in the layer) brought about a remarkable decrease in density of misfit-induced defects (stacking faults). When the nominal peak concentration of implanted C was greater than 0.55 at%, stacking fault generation in the epitaxial layer was considerably suppressed. This effect is attributed to strain compensation by C atoms in the SiGe lattice. A SiGe alloy layer with 0.9 at% C peak concentration under a 12 at% Ge peak exhibited the best microstructure. The experimental results, combined with a simple model calculation, indicate that the optimum Ge/C ratio for strain compensation is between 11 and 22. The interface between the amorphous and regrown phases (a/c interface) showed a dramatic morphology change during its migration to the surface. The initial <100> planar interface decomposes into a <111> faceted interface, changing the growth kinetics. These phenomena are associated with strain relaxation by stacking fault formation on (111) planes in the a/c interface.

Ronald Gronsky 4/21/94

Table of Content

Acknowledgments v

1. Introduction

    1.1 Ion Beam Synthesis(IBS) and previous work 1

    1.2 Motivation for Ion Beam Synthesis of SiGe alloy layers 2

    1.3 Objectives of the present work 3

2. Background

    2.1 Amorphization of Si subsurface. 4

        2.1.1 Collision cascade 4

        2.1.2 Efftects of implantation temperature and dose rate 6

        2.1.3 Effects of ion mass 7

        2.1.4 Concept of the threshold damage density (TDD) 8

        2.1.5 Formation of end of range (EOR) defects 9

    2.2 Solid Phase Epitaxy (SPE) 11

        2.2.1 General characteristics 11

        2.2.2 SPE with medium. 12

        2.2.3 SPE without medium 12

        2.2.4 Strain relaxation in SPE of amorphous SiGe layers 15

    2.3 Schematic view of the defects generated in IBS of SiGe layers 17

3. Experimental results

    3.1 Design of experiments 27

    3.2 Starting materials and ion implantation 28

    3.3 SPE annealing 29

3.4 Characterization of SiGe alloy layers

3.4.1 Rutherford backscattering spectrometry (RBS) 30

3.4.2 Crossectional transmission electron microscopy (XTEM) . . . 35

3.4.3 X-ray diffraction (XRD) using monochromatic crystal (Ge) rocking . 38

3.4.4 Raman spectroscopy 39

4. Results

4.1 Ge profiles in SiGe layers and layer thickness 45

4.2 Amorphized layer thickness and damage beyond a/c interface. . . . 46

4.3 EOR dislocation loops in SPE regrown layers 47

4.4 Strain-induced stacking faults in SPE regrown SiGe layers. 48

4.5 Regrowth behavior of SiGe alloy layers. 49

4.6 SiGe layers SPE-regrown after C sequential implantation 50

5. Discussion

5.1 EOR dislocation loops. 71

5.2 Equilibrium critical thickness and kinetics for misfit defect generation . .72

5.3 Misfit-induced stacking fault generation and growth kinetics of SPE layer 76

5.4 Critical average strain for generating misfit-induced defects. 78

5.5 Strain compensation by C sequential implantation 79

5.6 Optimum Ge/C ratio for strain compensation 81

6. Conclusions 95

References 98

Appendix 105

Acknowledgments

I, firstly, would like to thank my Lord, Jesus Christ for His sincere lead to Ph.D, a small goal in my life. He taught me patience, wisdom, and, forgiveness through this short or long process of degree. Without His invisible help, I could not get a Ph.D, I confess. I also want to remember my spiritual brothers in Berkland Baptist Church. Due to the prayer and fellowship with them, I could not be dishartened in any trouble.

I want to express my appreciation to Professor Ron Gronsky for his help, advice and saving me particulary when I was dispirited. He has always encouraged me with trust and his wealth of knowledge.

I am also indebted to Professor Nathan Cheung in the Department of Electrical Engineering and Computer Sciences. Working on my research, I learned a lot from him, including materials science, device physics, how to approach research problems, even how to apply common sense or freshman physics to research, etc. His practical teaching has always been valuable and his tremendous passion for science and engineering has often given me internal challenges.

My fellow graduate students in EECS and MSME --- especially Erin C. Jones, Ski, Hyuncheol Sohn, Wan-Shik Hong, and Mike Brazil---- have given me a lot of scientific advice and emotional support. I am also grateful to Jiang Tao, Bill En, Jingbao Liu, Zara Weng, James Chan, and Tracy Fu who helped point me in the right direction.

I'd like to thank Professor Jack Washburn, Dr. Kin Man Yu, Dr. Joel Ager, Dr. Ian Brown, and Professor Eugene Haller in Lawrence Berkeley Laboratory for their help in using RBS, Raman spectroscopy, and Ion Implanters. Especially, I owed Dr. Kin Man Yu and Professor Washburn valuable discussion on my research.

Finally, I am so much grateful to my wife, Jihye, for her love, patience, and support, and for making my five years in Berkeley endurable. Many thanks to my boys, Jaehyung, Jaeho, and Jaeshin for no complaining about their poor daddy.

1. Introduction

1.1 Ion Beam Synthesis(IBS) and previous work

Ion implantation is an established technique for precise dopant control in the integrated circuit (IC) processing.[1-5] The technique has focused on supplying carriers to electrically defined layers using low dose implantation. However, high-dose implantation may also be useful in IC processing. Ion beam synthesis (IBS) is a subsurface film synthesis technique where high dose implantation is used to change the material's chemistry. [6,7] IBS consists of two steps: amorphization by high dose implantation and solid phase epitaxial (SPE) annealing. This subsurface modification technique has been employed for making compound layers such as $CoSi_2$, $FeSi_2$, and buried layers of oxide, known as SIMOX (Separated by IMplanted Oxygen)[8-15]. In recent years, this technique has lead to the formation of SiGe alloy layers, which are not compounds but layers of soluble constituents. [16-18] Paine et al[16,17] performed a systematic study to estimate critical thicknesses of strained SiGe alloy layers formed by IBS. Taking account of ion beam energy and implanted doses, they assumed that Ge distribution after ion implantation was Gaussian-like for modelling of the critical thickness. The strain relaxation of the film was studied and the observed strain-induced defects were mostly stacking faults. However, their equilibrium condition for critical thickness does not explain why stacking faults are dominant in the resulting layers. Kinetic limitations on misfit dislocation generation were not clearly considered in their work, and strain measurements were not made. Even so,

they observed interesting properties of misfit dislocations in the solid phase epitaxial SiGe/Si and SiGe/Ge systems.

1.2 Motivation for Ion Beam Synthesis of SiGe alloy layers

There are several motivations for the present work. First, IBS can be a possible candidate among thin film growth techniques to grow SiGe layers which are used as the base materials for heterojunction bipolar transistors (HBT). Heterojunction bipolar transistors are expected to have outstanding transistor properties since SiGe has a narrower band gap than Si. Even though IBS layers have a Gaussian distribution of Ge atoms (not a uniform distribution), the properties of SiGe HBTs made by IBS are still promising. They have shown a higher injection of minority carriers and higher emitter efficiency than Si homojunction bipolar transistors. [19,20] Second, unlike other thin film growing techniques, IBS can be used with a two-dimensional mask to plant thin layers in selected device areas. In contrast, molecular beam epitaxy (MBE) or other vapor phase epitaxy can not match the lateral resolution of two dimensional patterning available with the ion beam method. Much work has been done to make the most of this advantage. [21,22] In those studies, PN diodes, instead of HBTs, have been fabricated by using IBS. Diodes made with p-type SiGe layer and n-type Si were compared to Si homojunction PN diodes. The SiGe diodes were found to have much higher leakage current by more than 10 times under reverse bias. This high leakage current under reverse bias rendered the device inadequate for the real applications of heterojunctions. The leakage must be caused by lattice defects in the SiGe alloy layers formed by IBS because deep-level impurities tend to

gather around extended lattice defects such as dislocations which have strong strain fields and charges in their cores. These defects may act as recombination or generation centers during device operation. [23,24] In addition to the problem of the leakage current, the pipe-diffusion of dopants along dislocation cores can lead to critical failure in devices if emitter dopants diffuse through the line to the base or collector regions in bipolar transistors. [25] Only when those defects are clearly identified and understood in aspects of their origins, those failures may be avoided.

1.3 Objectives of the present work

The main objectives of this work are to solve the device problems introduced by usual ion beam synthesis. The problems are caused by both implantation defects and strain-induced defects. Those two kinds of defects are spatially separated in two different regions of a layer, and will be suppressed if the implantation and strain-induced defects are eliminated. To minimize the density of the defects, the formation mechanism of each defect has to be clearly understood. The goals of the present work are therefore to understand the formation of the defects and to minimize them by optimizing the IBS processing conditions.

2. Background

2.1 Amorphization of Si subsurface

2.1.1 Collision cascade

An energetic ion is subject to two major mechanisms of energy loss during penetration into a solid: screened coulombic collisions with target atoms and interactions with bound or free electrons (excitation of electrons). [1-4] The former is called nuclear stopping and the latter called electronic stopping. Lindhard, Scharff and Schiott have developed a universal relationship, the LSS theory for nuclear stopping, $(d\varepsilon/d\rho)_n$, and electronic stopping, $(d\varepsilon/d\rho)_e$, in terms of a dimensionless length, ρ, and a dimensionless energy, ε. Both parameters, ρ and ε, include a mass dependence on the masses of both target atom and incident ion). [26,27] The relationship is shown in plots of $(d\varepsilon/d\rho)$ vs. $\varepsilon^{1/2}$ in fig. 1. The ion implantation regime and ion beam analysis regime can be approximately defined according to projectile ion mass and energy as shown in fig. 1. The ion beam analysis regime will be explained in detail in the discussion of Rutherford backscattering spectrometry (RBS) in Chapter 3.

The Si lattice is damaged to a depth related to the implantation energy during the energy loss process in ion implantation because the energy loss mainly results from nuclear stopping of penetrating ions rather than electronic stopping in this regime. Incident ions in the implantation regime of the LSS plot (fig. 1) make a series of collisions with lattice atoms. In most of these collision events, sufficient energy and momentum are transferred to displace or recoil the target atom from its lattice site. This displaced atom may displace

other atoms in turn, until a cascade of atomic collisions with vacancies and interstitials are created. Cascades usually overlap during long implantation processes and eventually change a crystalline subsurface into an amorphous phase as shown in fig. 2. This is a general description of amorphous layer formation by overlap of the damage clusters or cascades. If the amorphization is considered in terms of the number of displaced atoms in the collisions, Kinchin-Pease relationship may be introduced to explain the process of amorphization:

$$N_d = E/2E_d \tag{1}$$

where N_d is the number of target atoms displaced by a primary recoil, E is the energy of the incident ion and E_d is the displacement energy which is 15eV ~ 50eV. [1] If the electronic stopping is negligible and only a primary collision of the implanted ion with a target atom is allowed, the critical dose for amorphization is approximately worked out from the Kinchin-Pease equation:

$$\text{Critical dose} = 2E_d D(N_d)/(dE/dx)_n \tag{2}$$

, where $D(N_d)$ is the density of displaced atoms required for amorphization, approximated by the atomic density of target assuming that the criterion for amorphization is complete displacement or disorder of crystalline target atoms, and $(dE/dx)_n$ is the energy deposited

by one ion per unit distance in a nuclear collision. However, in actuality, this equation overestimates the amount of disorder by taking a higher density of displaced atoms, $D(N_d)$ than the actual density for amorphization. In spite of that overestimation, however, the critical dose is always underestimated because dynamical annealing effects that result in a higher E_d usually intervene. [28,29]

2.1.2 Effects of implantation temperature and dose rate

During implantation, some of ion beam energy is converted into thermal energy heating the target wafer. This thermal energy from beam heating will increase the wafer temperature. The dynamical annealing causes a recombination of vacancies and recoiled interstitials by thermal diffusion in an implantation temperature which is obtained by the beam heating effects added to an original wafer temperature. Amorphization or lattice damage may be prevented by this annealing effect if the recombination is very active with an enough thermal energy. [28,29] Therefore, implantation temperature of wafer can be an important factor in controlling the critical dose. Displacement energy, E_d is then a function of implantation temperature, increasing with temperature. If the implantation is performed at high temperature, the amorphization will be very hard to achieve, even with a very high dose of ions. In other words, the critical dose will be very high. If the implantation is done at a very low temperature by using a heat sink, amorphization may be enhanced with little dynamical annealing effect. Since this dynamical annealing accompanies diffusion phenomena of vacancies or interstitials and the diffusion distance depends on time and temperature, ion beam current density or dose rate in implantation

should affect the total damage. With an increase in dose rate, the critical dose decreases in most cases. It is comprehensible that the amorphous layer thickness formed over the critical dose of ions increases with dose rate but decreases with the implantation temperature.

2.1.3 Effects of ion mass

A schematic diagram in fig. 3 shows the difference in a cascade through an ion track when a light ion and a heavy ion are implanted in the same crystalline target. With the same amount of kinetic energy, light ions penetrate deeper than heavy ions which have more lateral distribution of both ions and damages as shown in fig. 3. Although the light ion will lose some portion of its energy by nuclear stopping in the ion implantation regime of the LSS relationship, the heavy ion will lose more energy by nuclear stopping through the target material. Therefore, more lattice damage will be created by implanting heavy ions and the critical dose of ions for amorphization will be lower. Since amorphization is more effective when using heavy ions, even local amorphization during cascade overlapping may be possible with heavy ions. Light ion implantation does hardly show local amorphization. In light ion implantation, the accumulation of point defects or clusters in a critical value lead a crystal structure to a sudden amorphous state during casacade overlapping. [27] According to the phase transformation mechanism discussed in previous studies, it is likely that the nucleation of amorphous phase is gradually and heterogeneously proceeded by increasing number of local amorphous regions in the case

of heavy ion implantation while the nucleation is abrupt and homogeneous in light ion implantation. [27] The latter is very similar to a first order transformation while the former is to a second order transformation. The plot in fig. 4 shows the effects of temperature and ion mass on the critical dose. [1,27] As mentioned above, light ions have a higher critical dose than heavy ions for amorphization and the critical dose increases with the implantation temperature.

2.1.4 Concept of the threshold damage density (TDD)

The energy deposition in a unit of eV/Å/ion, $(dE/dx)_n$, has a Gaussian-like depth profile that can be simulated by a program, TRIM, which is a Monte-Carlo simulation for projected ion range and energy deposition per ion in implantation. [29] In fig. 5, TRIM profiles of energy deposition by a heavy ion (Ge^+) and a light ion (O^+) are compared. With the same energy (120keV) of implantation, they are quite different from each other. Much higher energy can be deposited by the nuclear stopping of the heavy ion as noted in the scale of energy deposition while light ion damage shows a longer track than heavy ion damage. The total energy deposition, the damage density (DD) can be found as the product of energy deposition and the total dose, i.e., $(dE/dx)_n$*total dose = DD, with a unit of eV/cm^3. If the critical doses are known, the critical energy deposition can be calculated simply as $(dE/dx)_n$*critical dose. This amount is called the threshold damage density (TDD). From equation (2), the following relationship is also established,

$$\text{TDD} = \text{Critical dose} * (dE/dx)_n = 2E_d D(N_d) \qquad (3)$$

where TDD is a function of temperature, ion mass, ion energy, and dose rate if the target material is fixed. As expected, early research showed that the TDDs for As, P, and B implantation are different in value ($2.5x10^{20}$keV/cm^3, $1.0x10^{21}$keV/cm^3, and $5.0x10^{21}$keV/cm^3 respectively).[31,32] Schematic plots in fig. 6 show the damage density (DD) profiles and the threshold damage density (TDD) for Ge and O ions under the same implantation conditions. Amorphized thickness is defined at the depth locations where TDD and DD lines cross.[33] Therefore, a higher dose will make a thicker amorphous layer during implantation. Moreover, a buried amorphous layer can be formed by implanting light ions at an elevated temperature as shown in the same figure. The Separation by IMplanted OXygen(SIMOX) technique has been used previously to form a buried layer of by using this phenomenon.

2.1.5 Formation of end of range (EOR) defects

For many years, it has been well known that ion implantation introduces many kinds of extended lattice defects.[33-36,40-41] Generally speaking, Frenkel pairs are created during ion implantation and the concentration of these pairs of self-interstitials and vacancies determines the density of extended lattice defects.[2] Particular among those defects are end-of-range (EOR) defects which are formed only after amorphization.[33] End of range (EOR) defects always develop near the initial interface between the amorphous layer and the crystalline substrate (a/c interface). EOR defects have previously been described in terms of TDD or distribution of recoiled self-interstitials beyond the a/c interface.[33,37,38] In the present work, a similar theory is followed, using schematic concentration profiles of

interstitials and vacancies as shown in fig. 7 (a). The most probable location of vacancies created by the incident ion is apart from that of recoiled interstitials and the probable locations are also dependent on the energy loss (energy deposition) curve. The effective distance (peak-to-peak) between vacancy and interstitial distributions is strongly dependent on ion mass and energy. [27] For light ions with small energy, the peaks are not sufficiently separated, so that the vacancies will easily recombine with the interstitials. Further, amorphization or extreme lattice disorder is not easily achieved with this condition as mentioned in 2.1.3. The projected range of implanted ions is expected to be located between the vacancies and the interstitials in the depth profile. This has been confirmed previously. [39] After the amorphous layers form, the point defect profiles are as expected (fig. 7 (b)). The interstitial density is higher than vacancies in the region just beyond the a/c interface. If they are mobile at some temperature, interstitials may recombine with vacancies near them. Even after the recombination, a high density of interstitials may remain at this location and they may form clusters or extended defects such as extrinsic stacking faults when the remaining interstitials are supersaturated enough to cluster. This is the origin of EOR defects.

Freezing the mobile interstitials and vacancies by using a low substrate temperature during implantation results in both thicker amorphous layers and smaller densities of extra interstitials which results in a lower density of EOR defects than cases implanted at high temperatures. This is easily recognized in fig. 7(b). Therefore, this freezing or low temperature processing will be an effective method for minimizing EOR defects. This

explanation also makes sense considering the TDD concept where the amorphous thickness was defined by the cross over point between the TDD line and DD curve. Since the displacement energy, E_d, and TDD both become smaller in the case of low temperature implantation, the amorphous layer will increase and a smaller amount of interstitials beyond a/c interface will be produced. The schematic picture in fig. 7(c) illustrates the EOR loops grown during solid phase epitaxial (SPE) annealing of an amorphous layer. End of range (EOR) dislocation loop density is higher after room temperature implantation than after low temperature implantation. Low temperature implantation, then, is preferable for growing device-quality films. [35,36]

2.2 Solid phase epitaxy(SPE)

2.2.1 General characteristics

The defining characteristic of SPE is that the epitaxial growth or the phase transformation occurs in the solid state. Solid phase epitaxial (SPE) growth can be classified into two kinds: SPE with medium and SPE without medium. [7] Both kinds involve a transformation from a metastable phase to a stable phase with the lowest free energy, and both usually have an amorphous phase as the initial unstable state. The most stable state is defined by the equilibrium phase diagram. Figure 8 shows the equilibrium phase diagram of the Si-Ge system in which both elements are totally soluble in each other over the entire composition range. [42] SiGe alloy layer formation in IBS belongs to SPE without medium and the unstable amorphous structure regrows by duplicating the surface

structure of substrate and migrates into the stable crystalline phase at about a half of its melting temperature.

2.2.2 SPE with medium

Solid phase epitaxial regrowth proceeds by long-range diffusion and interfacial reaction. The best example of SPE with medium may be the case of c-Si/Pd_2Si/α-Si where c-Si is a (001) Si substrate and α-Si is an amorphous Si layer. Pd_2Si is a transport medium for the crystallization of α-Si film on Pd_2Si layer as shown in fig. 9(a). In the regrowth process, not only the Si atoms at the α-Si/ Pd_2Si interface migrate into the c-Si/Pd_2Si interface for epitaxial growth, but also Pd_2Si at the interface with c-Si decomposes into Pd and Si. The Si after decomposition grows epitaxially at the interface between c-Si and Pd_2Si while Pd diffuses across the Pd_2Si layer to α-Si interface, so that a new layer of Pd_2Si can form at the other interface(Pd_2Si/α-Si). In other words, the Pd_2Si layer moves up to the surface until the amorphous Si layer is consumed by means of interacial reaction and long-range diffusion of Pd. [7]

2.2.3 SPE without medium

A subsurface amorphized layer can be obtained by ion implantation as mentioned in 2.1. This amorphized layer will recrystallize at an elevated temperature without any transport medium. This is the case of SPE without medium and is shown in fig.9(b). In the figure, a Si ion beam was used for amorphization. Growth behavior of the layer is dependent on substrate temperature, substrate orientation, implanted species, and ion dose

used in the amorphization process. Si preamorphization has been extensively studied. During the regrowth following Si^+ ion implantation in a (100) substrate, the planar a/c interface moves towards the surface with a uniform velocity and an activation energy of about 2.68 eV for interface migration. The growth rate is expressed as

$$v = v_o \exp(-\Delta H_G/kT) \tag{4}$$

and where ΔH_G= 2.68 eV and v_o= $3x10^{-8}$cm/sec for (100) Si. The growth rate is also observed as a function of substrate orientation as shown in fig. 10. [43] The rate of regrowth on (100) orientation is about 25 times faster than the growth rate on (111) orientation. (111) growth often includes significant densities of microtwins and stacking faults. Physical understanding of both the generation of those defects and their slow growth rate has been provided by a model in which two complete bonds are required on the crystalline surface for layer formation, confirmed by observation of stacking faults in (111) layer growth using transmission electron microscope (TEM) . [44-46] An atomic model in fig. 11 illustrates the effects of surface orientations on regrowth behavior. Formation of two complete bonds is easy on a (100) orientation because only one atom is required to obtain two bonds on the surface. However, on a (111) surface, three atoms in a row must sit on the surface to form a new layer. If they sit in the proper way (N), no stacking faults form but if they sit in the other way (T), faults or twins are generated as shown in fig. 11. Note both ways of sitting, N and T in fig.11.

In addition to the surface or regrowth orientation effect, other interesting parameters are the ion species and their implantation doses. Figure 12 shows plots of regrowth rate as a function of ion species and their concentrations. [47-51] If the implanted dose or concentration is too high in amorphized layers, the epitaxial growth rate decreases. Moreover, polycrystalline regrowth occurs instead of epitaxial growth if the impurity concentration is well above the solubility limit. This phenomenon is frequently seen in (111) Si while it is less likely in (100) Si. Nucleation of polycrystals usually occurs at impurity precipitates or aggregrates in the amorphous phase formed by high dose implantation. [7] According to Williams et al [49], polycrystalline nucleation is thought to arise either from precipitates of the fast diffusing impurity species already present in the amorphous phase, or as a result of slow regrowth and impurity segregation at the moving interface for the impurities of low diffusity. Since (111) growth is very slow, there is sufficient time for the nucleation and growth of the precipitates or interface aggregrates during (111) growth. If the density of precipitate nuclei is high enough, epitaxial growth is difficult and poor epitaxial growth occurs because those precipitates have different orientation relationships with the Si substrate.

In the case of low dose amorphization, regrown crystalline layers are known to be of better quality than the crystalline subsurface when implanted without amorphization and then annealed. [1,3] Electrical activation of dopants was much better in the case of preamorphization before dopant implantation than in the case of normal dopant implantation which usually shows a negative annealing effect. [1,3] In the case of boron

implantation in crystalline Si, the electrical activation curve during isochronal annealing shows a negative curvature or a sudden deactivation at 600°C while steady activation has been shown at the same implantation and annealing condition in the case of preamorphized Si. This is because boron atoms form pairs or aggregrates at temperatures near 600°C. Recrystallization may not allow such pairing of boron atoms. [3]

2.2.4 Strain relaxation in SPE of amorphous SiGe layers

In the thermodynamics of thin film growth, strain energy is not a critical factor for nucleation and growth, although the thermodynamic driving force and surface energy terms are very important. But the strain energy term becomes important when considering the strain relaxation by defect generation in heteroepitaxial layers, that is, when the epilayer formation is allowed with large enough driving force and wettability. [7,52] The formation of strained or strain-relaxed SiGe layers has been extensively studied using molecular beam epitaxy (MBE) or other vapor phase epitaxy (VPE). Misfit strain or tetragonal distortion have been measured by x-ray diffraction and other methods in commensurate SiGe layers. [53,54] Recently, strain relaxation of SiGe layers formed by IBS has also gained some attention by several researchers. [16,17,55] SiGe layers made by IBS have Gaussian-like Ge concentration profiles while strained layers made by VPE have uniform Ge concentrations. Unlike the strain relaxation in VPE SiGe layers in which mainly 60° perfect dislocations are generated as misfit dislocations near the (100) growing film surface, strain relaxation in SPE SiGe layers on (100) Si results primarily in stacking faults with partial dislocations. A perfect dislocation has the largest burger's vector, and

therefore the most effective strain relaxation in (100) oriented film growth. In order to understand the stacking fault generation in SPE, the concept of equilibrium critical thickness was modified to consider Gaussian strain profile in the SiGe layers formed by high dose ion implantation. [16,17,55] Without considering the activation barrier for the nucleation of strain-induced defects, the stacking fault generation could not be well explained. In group 4 materials such as Si, and Ge, the nucleation barrier is as important as the strain energy to be relieved (The barrier is usually regarded as the migration barrier for misfit dislocation which is a typical strain-induced defect, because dislocation migration creates new segments of dislocation line). Moreover, because stacking faults do not appear between the Ge peak location and the EOR region, the energy balancing equation for the critical thickness may not be correct in the estimation of total stacking fault energy or dislocation self-energy. Therefore, stacking fault generation must be understood differently by considering both the kinetic barrier opposing stacking fault nucleation and the morphology of the a/c interface where (111) habit planes exist and also where the stacking faults or dislocations are nucleated. According to a recent report, dissociation of perfect misfit dislocations into partial dislocations is possible in strain relaxation on surfaces other than (100) oriented surfaces under compressive stresses. [56] It is likely that the a/c interface of SPE layers in microscopic view contains (111) planes in high density while the growing surface of VPE film is relatively flat in (100) orientation. This information can clarify why SPE growth even on a (100) substrate shows a high density of stacking faults.

2.3 Schematic view of the defects generated in IBS of SiGe layers

From the context of 2.1 and 2.2, it is presumed that the SiGe layers formed by IBS contain two different lattice defects that are located at different depths: EOR defects and strain-induced stacking faults. A schematic picture in fig. 13 illustrates these two defects. Strain-induced defects are located near the projected range (R_p) of implanted Ge ions, while EOR defects are closer to the Si substrate.

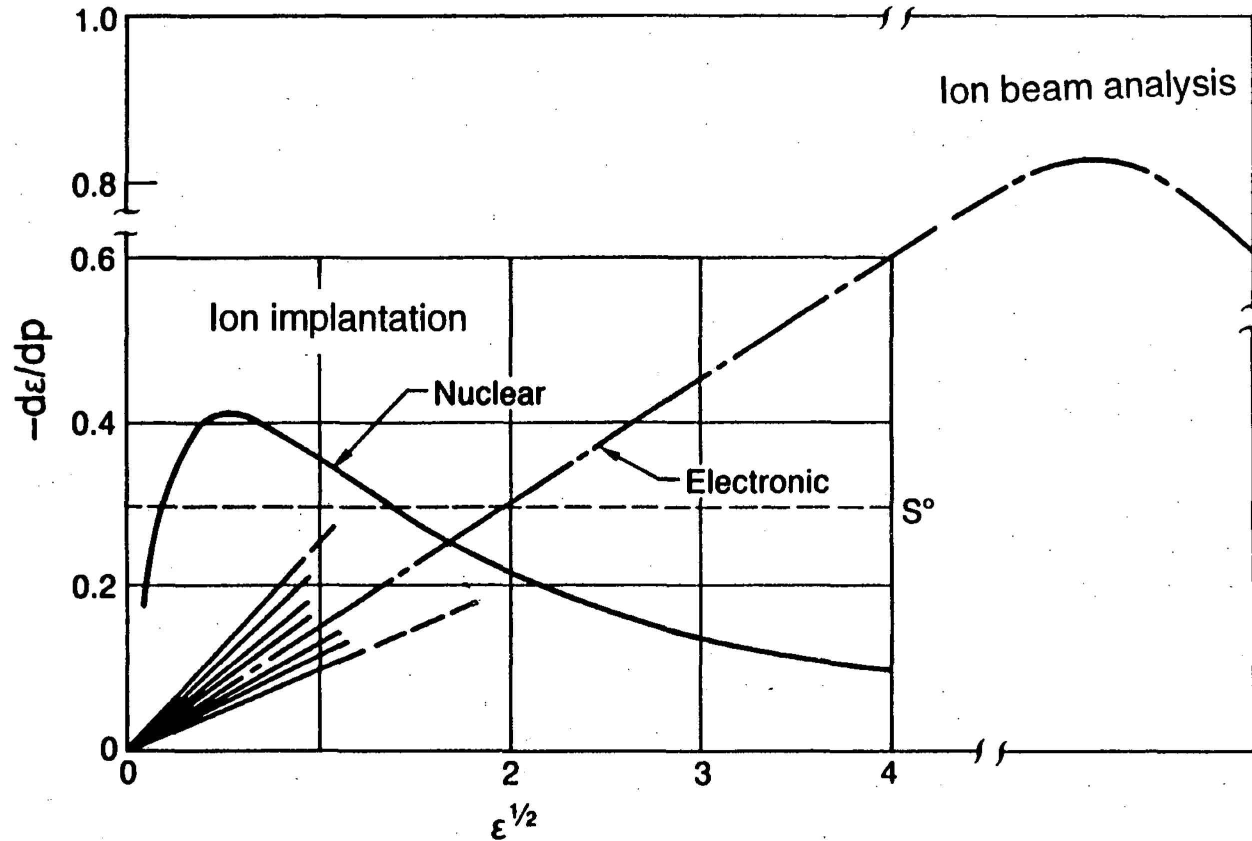

Fig. 1. Nuclear stopping and Electronic stopping in LSS theory. Implantation regime and ion beam analysis regime are distinguished from each other in $\varepsilon^{1/2}$ axis. The slope of electronic stopping curve decreases with a projectile ion mass, which signifies that nuclear stopping is more dominant with higher mass of projectile. (After Shih[27])

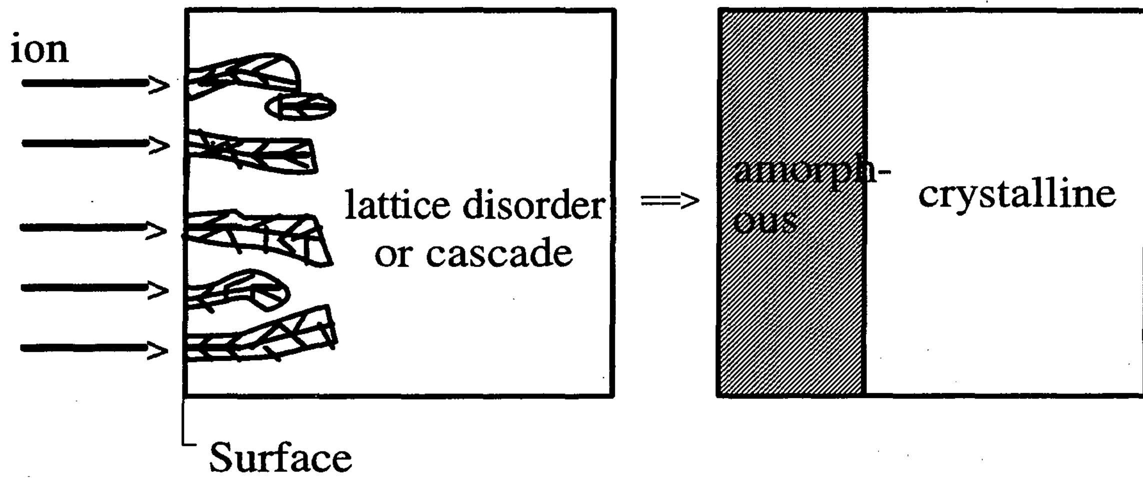

Fig. 2. Cascade overlapping and subsurface amorphization by implanting ions

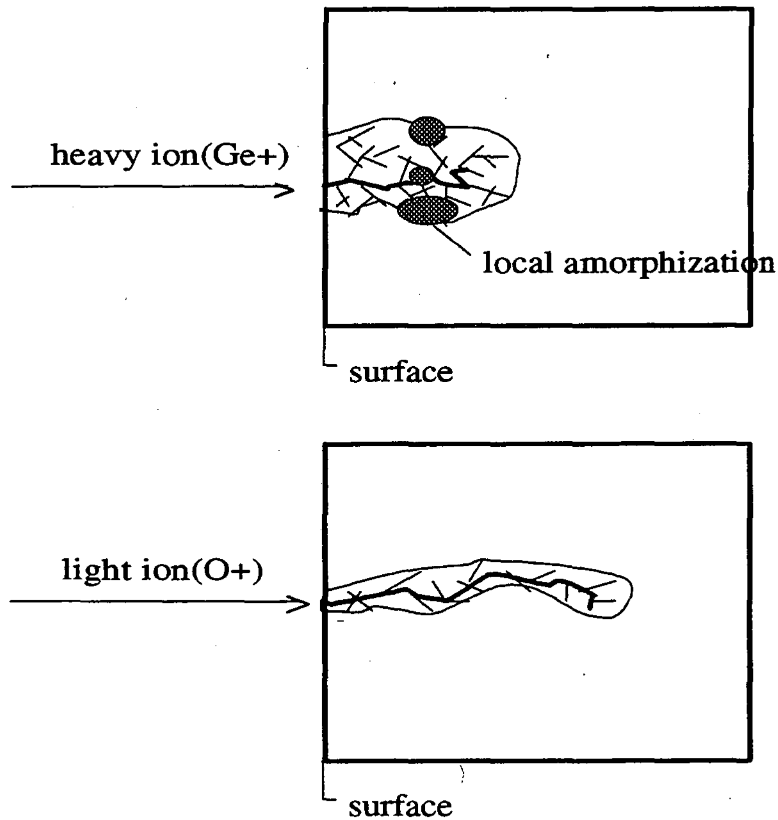

Fig. 3. Difference in cascade track between a heavy ion and a light ion. During the cascade overlap by heavy ions, local amorphized region may form in some regions of crystalline subsurface.

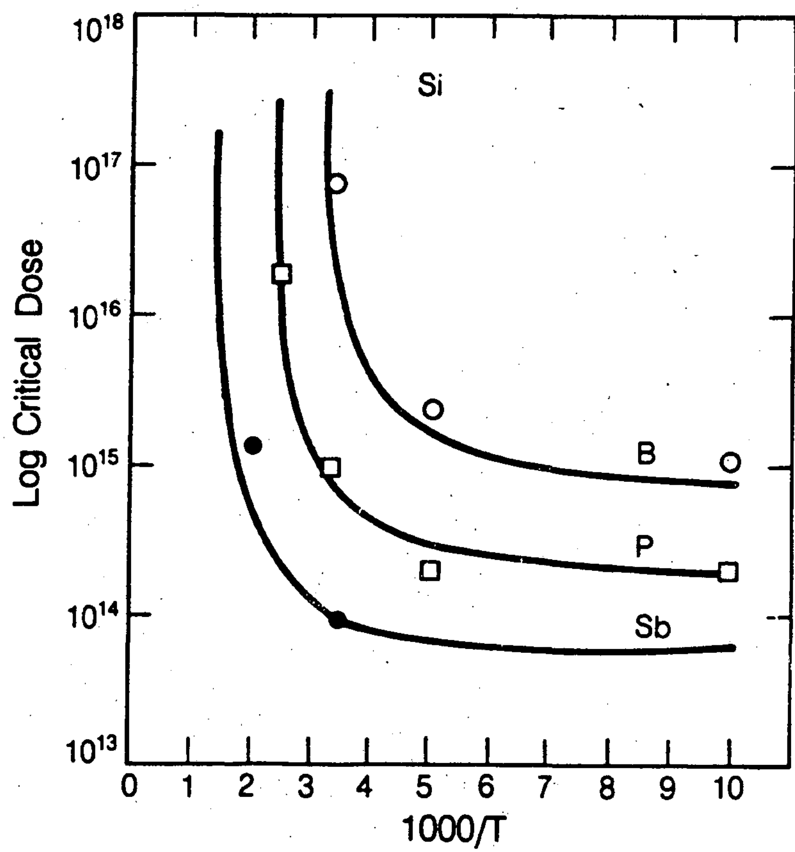

Fig. 4. Effect of temperature and ion mass(ion species) on critical dose for amorphization of Si. (After Ryssel[1])

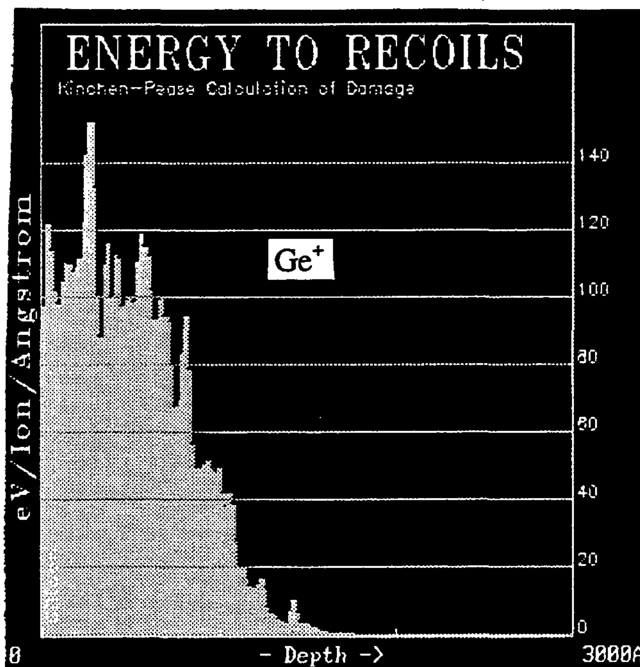

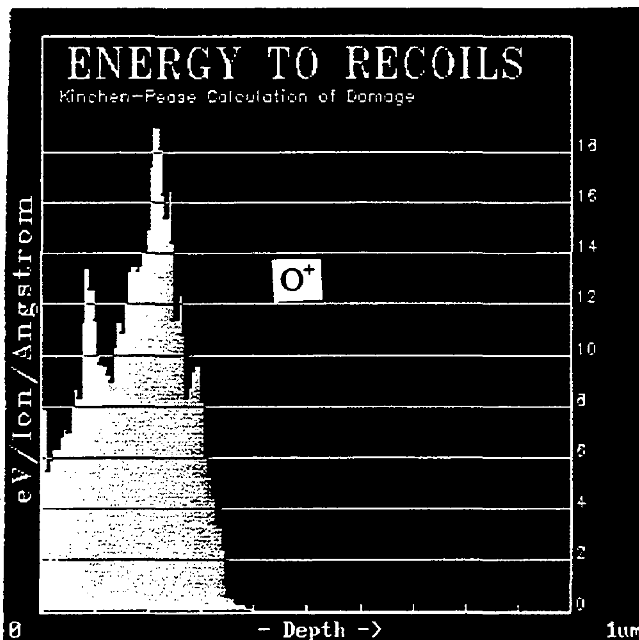

Fig. 5. Energy deposition profiles by nuclear stopping $(dE/dx)_n$ of Ge^+ and O^+ with an energy of 120 keV as simulated in TRIM. Unit in energy deposition is expressed in eV/Å. Note the different scales of both energy loss and depth in two simulations.

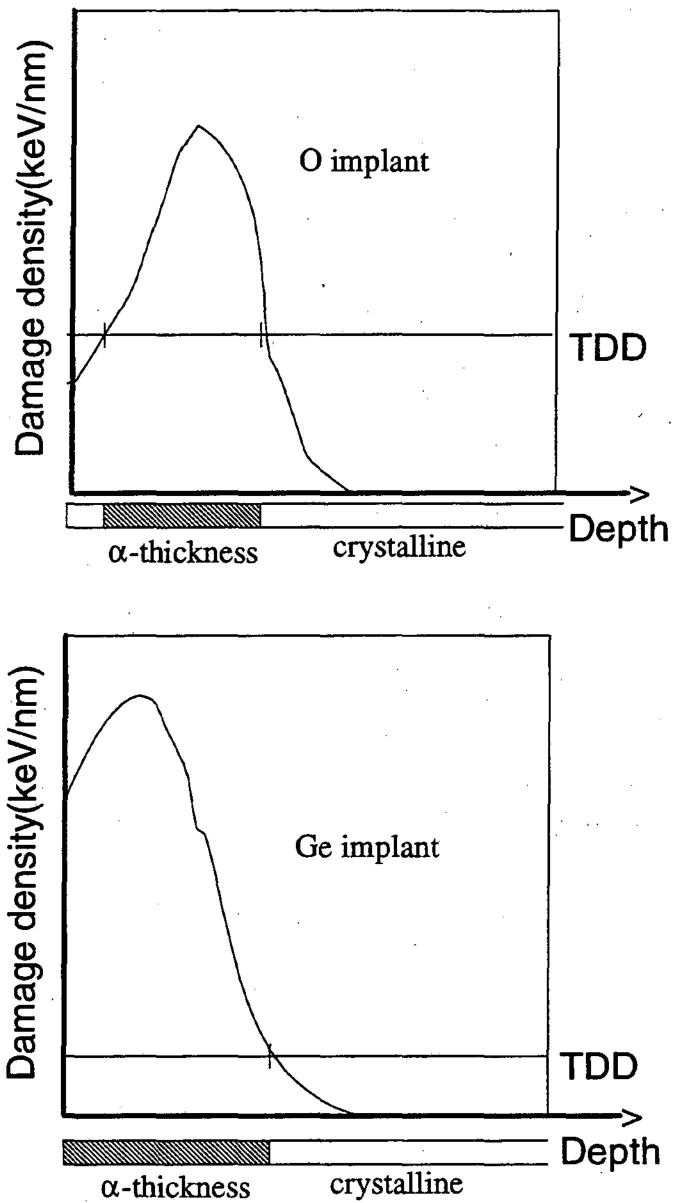

Fig. 6. Damage density(DD) curve after high dose implantations. Amorphous thickness in heavy ion or light ion implantation is determined by TDD line crossing the DD curves. Buried laryer may form in a proper condition of light ion implantation.

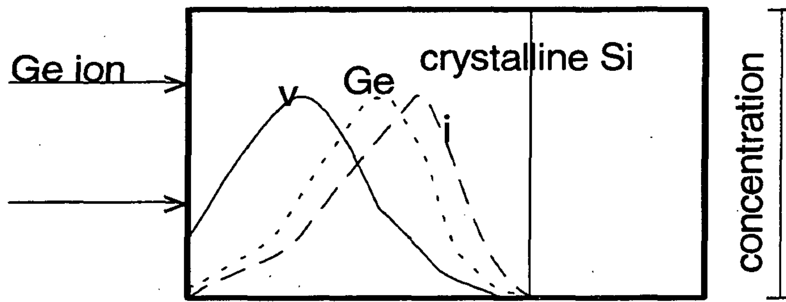

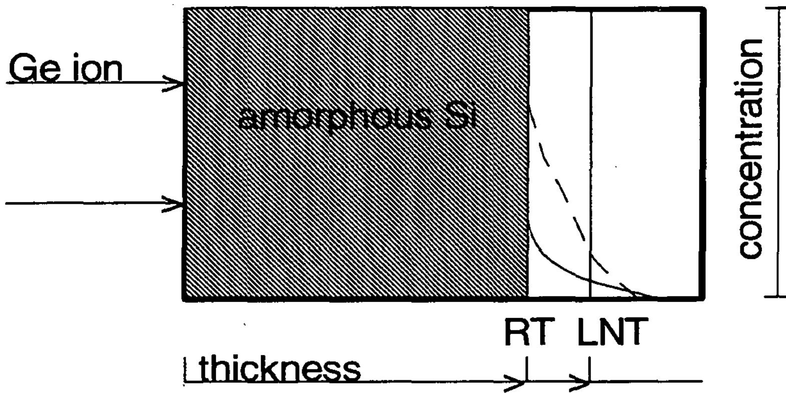

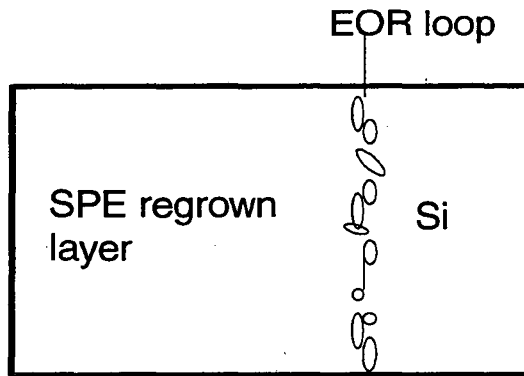

Fig. 7. Origin and formation of EOR dislocation loops.

(a) vacancy and interstitial profiles in implantation process before amophization

(b) vacancy and interstitial profiles beyond a/c interface after amorphization. Thicker α layer is achieved by LNT implantation than by RT implantation.

(c) Developed EOR loops after SPE annealing

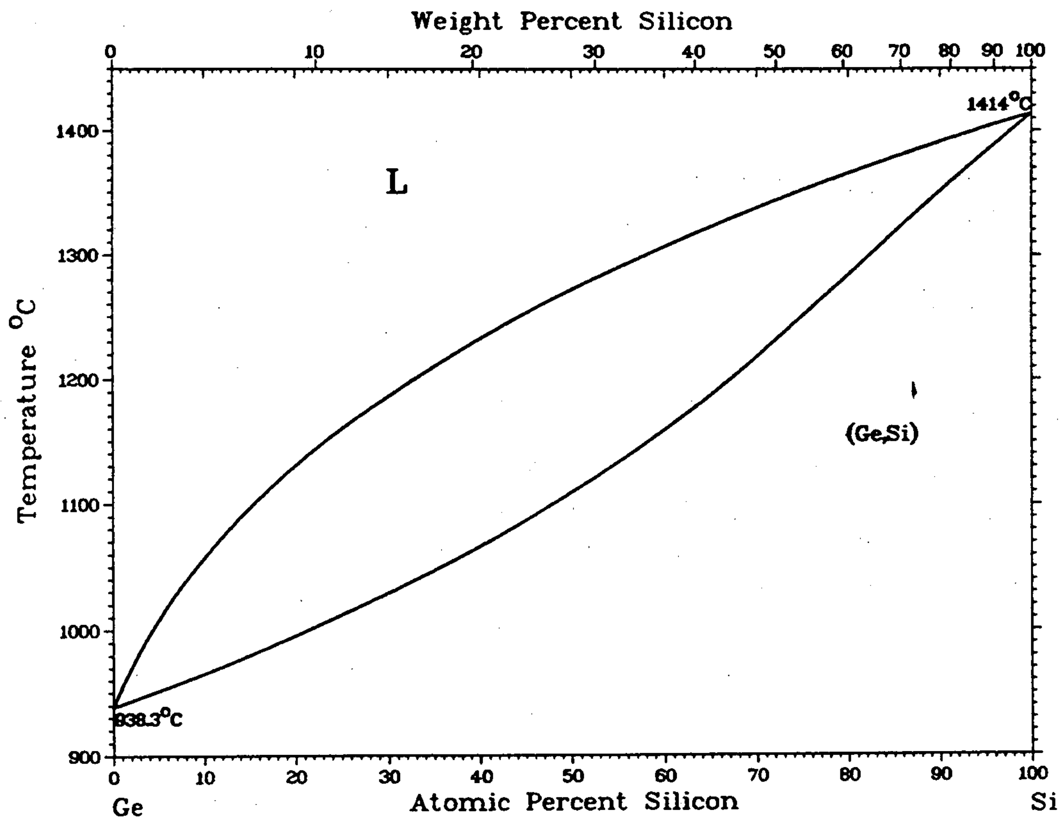

Fig. 8 Equilibrium phase diagram of Si-Ge binary alloy system. (After Olesinski[42])

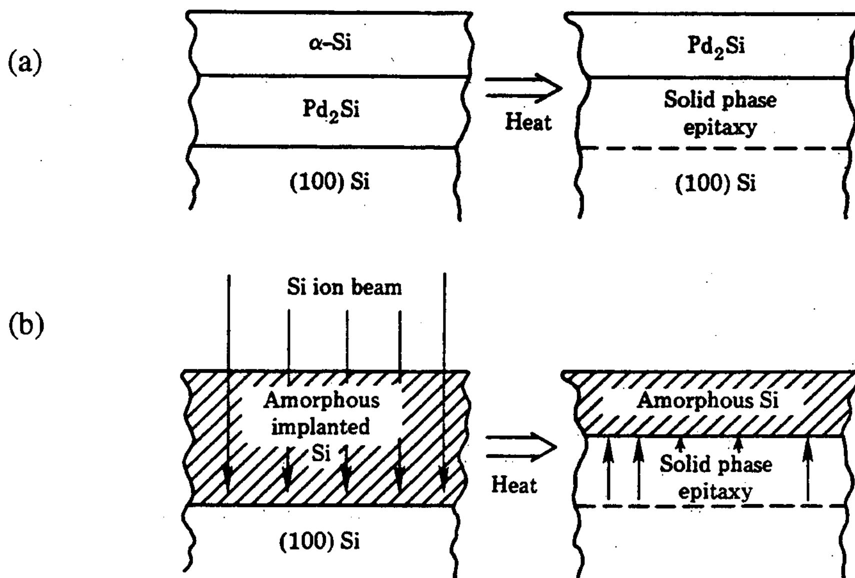

Fig. 9. (a) SPE process with medium (Pd_2Si layer on Si),
(b) SPE process without medium (preamorphization by Si ion beam).

Fig. 10. SPE regrowth rate of Si as a function of substrate orientation. (After Sigmon[43])

Fig. 11. Effect of substrate orientation on atomic layer formation. (After Drosd and Washburn[44])

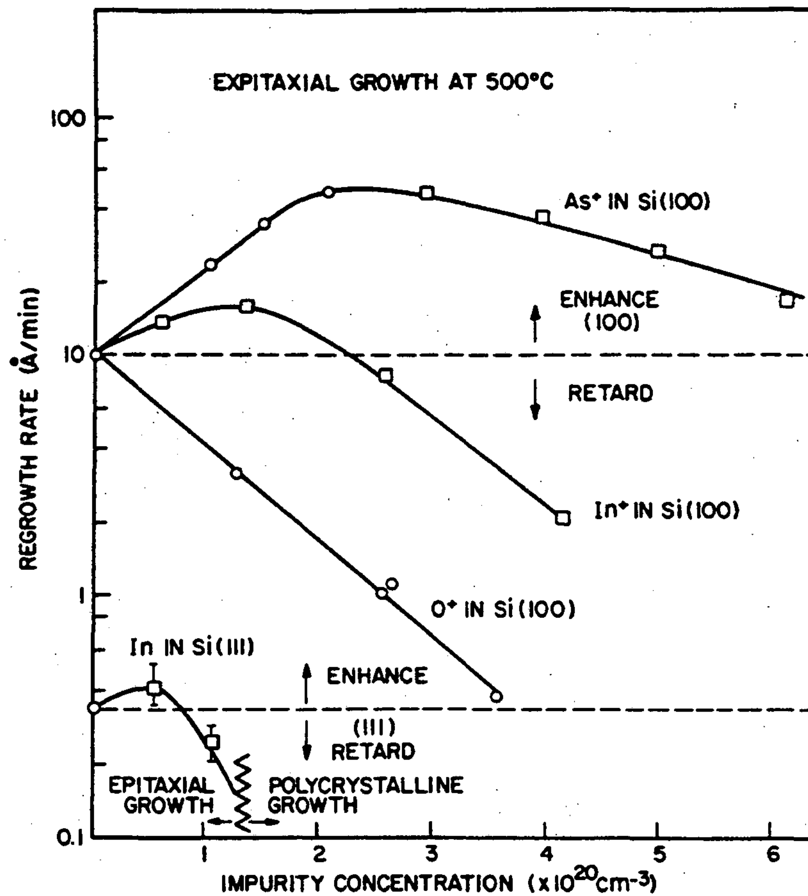

Fig. 12. Effect of ion species and dose(impurity concentration) on SPE regrowth rate of (100) and (111) oriented Si. High dose implantation may lead to retarded regrowth rate. (After Williams[47])

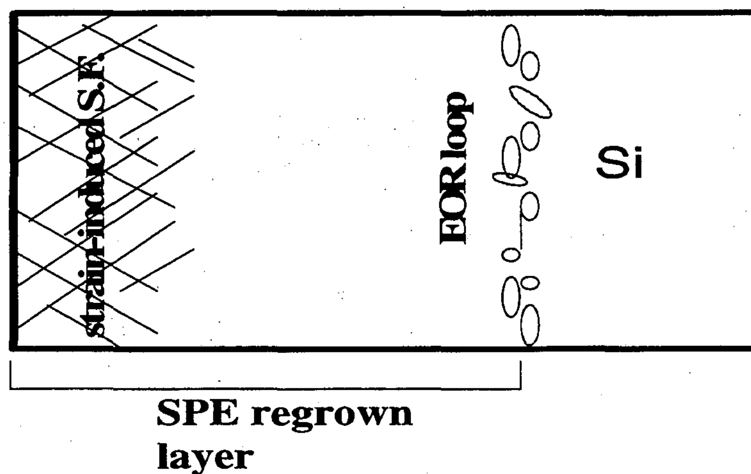

Fig. 13. A schematic picture illustrating EOR loops and strain-induced stacking faults in a SPE grown SiGe layer with a high Ge peak concebtration.

3. Experiments

3.1 Design of experiments

Experimental conditions were determined to isolate or spatially distinguish EOR defects and strain-induced stacking faults in layer images achieved by cross-sectional transmission electron microscopy (XTEM). According to previous work, if an As^+ ion beam energy of 120keV is used, an amorphous layer thickness of 1500Å results when the total dose is on the order of $10^{16}/cm^2$.[31,32] Since the mass of Ge^+ (73amu) is nearly the same as that of As^+ (74.9amu), we can still use a reference equation for the amorphous thickness formed by As^+ implantation as follows,

$$\text{Thickness}(\alpha) = R_p + 3\Delta R_p \tag{5}$$

The projected range of Ge, R_p, and the Ge ion straggle, ΔR_p, at that ion energy are about 820Å and 250Å, respectively, as shown in table 1 of the Appendix. Assuming that the Ge concentration profile is Gaussian-like, the total dose to achieve a certain Ge peak concentration can be determined. Practically, 1500Å is a thick enough layer to be observed by conventional transmission electron microscopy (CTEM) which is used to resolve the two different spatial depths where EOR loops and strain-induced stacking faults are located in the SiGe layers (the amorphous layer thickness is almost the same as the SPE-regrown layer thickness). After fixing the implant energy for achieving sufficient layer thickness at 120 keV, IBS experiments to minimize EOR dislocation loops and

strain-induced stacking faults were designed as shown in table. 1. Room temperature (RT) implantation and liquid nitrogen temperature (LNT) implantation are obvious methods to study the reduction of EOR loop density. To reduce the stacking faults generated in the Ge peak region, lowering the Ge dose and sequential C implantation for strain compensation were also tried.

3.2 Starting materials and ion implantation

The starting materials were 4-inch Si wafers with (100) oriented surface and n-type doping to resistivities of 1 to 5 ohm-cm. Ge ion (Ge^+) implantations were performed to obtain three high-Ge doses which were $2x10^{16}cm^{-2}$, $3x10^{16}cm^{-2}$, and $5x10^{16}cm^{-2}$. Corresponding Ge peaks in units of atomic concentration were determined to be 5%, 7%, and 12%, respectively, by using Rutherford backscattering spectrometry (RBS) after implantation. Both RT and LNT implantation were done at these three doses and an implantation energy of 120 keV. The as-implanted alloy layers with 12% Ge peak concentration (LNT) were then subjected to sequential implantations of C ions (C^+) at room temperature, using a beam energy of 22keV to position the C ion peak at the same depth as the Ge peak. Three different C doses of $1x10^{15}cm^{-2}$, $2x10^{15}cm^{-2}$, and $3.5x10^{15}cm^{-2}$ were used to yield three anticipated C peak concentrations of 0.3, 0.55, and 0.9 at%, respectively. Germanium ion (Ge^+) implantation was done by using a Varian 200-DF4 implanter at the Lawrence Berkeley Laboratory (LBL). The ion current was about 60μA for all Ge implantations. The wafer station had an about 1cm thick aluminum plate

which was used for wafer loading in one side, so the plate could contact liquid nitrogen on the other side. Since the total dose measured by Faraday cup in the implanter included secondary electron yield as well as ion yield, calibrations by using RBS were always performed to obtain exact ion doses. For C ion implantation, a metal-vapor vacuum-arc (MEVVA) ion source at LBL was used. Although the MEEVA ion source has no mass analysis for selecting charges and isotopes, time of flight spectra showing the charge state for a graphite cathode proved monojetic ion (C^+) behavior. [57-59]

Table. 1. Experimental approaches for minimizing defects

Defect kinds	Approaches
EOR loops	1. RT implant 2. LNT implant
Misfit Dislocations (stacking faults)	1. Lower Ge doses to get lower peak at%(12, 7, 5 at% in peak) 2. C sequential implantation 12 at% peak of Ge implanted layers(nominal C peaks 0.3, 0.55, 0.9 at%)

3.3 SPE annealing

For the study of defect minimization, furnace annealing for SPE was performed at 800°C for 1 hour in a nitrogen ambient although the usual temperature for amorphized Si

regrowth is only 550 to 600°C.[16-18] Since these amorphized layers have very high dose of Ge as an alloying element, the regrowth rate is expected to decrease as explained in 2.2.3. In order to achieve full regrowth, a higher temperature than the regrowth temperature for amorphized pure Si was selected in this work. A nitrogen ambient was used for preventing specimen surface oxidation.

Separately, lower temperature (550°C) annealing of the amorphous alloy layer with the highest dose was done to observe the migration behavior of a/c interface. In other words, partial regrowth annealing of the SiGe alloy layer with 12 at% Ge peak was performed at that temperature for different time periods (1 hour and 5 hours).

3.4 Characterization of SiGe alloy layers

3.4.1 Rutherford backscattering spectrometry (RBS)

In order to measure Ge doses, RBS was performed on as-implanted specimens. Depth profiles for Ge composition in the alloy layers were also obtained by using Ge signals from random or channeled RBS spectra. Amorphized Si thicknesses were measured from Si signals by ion channeling. With SPE annealed samples, <110> ion channeling was employed to quantize the relative crystallinity of the annealed layers by measuring minimum backscattering yields, χ_{min}. For all RBS measurements including ion channeling in this study, specific spectrometry conditions were employed and schematic diagrams of backscattering conditions in fig. 14 illustrate the conditions. Scattering angle, θ and detector angle, θ_d, were fixed at 165° and 15°, respectively. An identical $^{4}He^{+}$ ion

energy of 1.95 MeV was also used in every experiment. Spectra conditions for each specimen are summarized in table. 2. Since in RBS, a light ion is used as a projectile with a very high kinetic energy (MeV), energy loss is dominated by electronic stopping in target materials. Ion beam analysis regime of LSS plots in fig. 1 meets this condition of ion mass and energy. However, a small amount of elastically backscattered ions are counted as signals in a detector channel which linearly corresponds to backscattered energy of ions. The examplary spectrum of fig. 15 shows the two signals obtained from the two elements of a binary compound film (SiO_2) on a substrate(Si). [60] The backscattered ion energy is so dependent on target material and scattering angle that the dose and depth profile of impurity atoms may be measured with impurity signal profiles separated from substrate signals. In the case of a compound thin film (Si_mO_n) of uniform composition, the following well-known equation is used for composition calculation,

$$m/n = (H_{Si}/H_O)\,(Z_O/Z_{Si})^2[\varepsilon_{Si}]/[\varepsilon_O] \tag{6}$$

where H_{Si} and H_O are heights of signals from Si and O in the film Si_mO_n, Z_O and Z_{Si} are atomic numbers of Si and O element in the film Si_mO_n, and $[\varepsilon_{Si}]$ and $[\varepsilon_O]$ are electronic stoppings by element Si and O in the film. The ratio $H_{Si}[\varepsilon_{Si}]/H_O[\varepsilon_O]$ is same as the ratio of the area under the signals which can be directly measured from the spectra, so that m/n can be simply determined. [60] Using these concepts, implanted Ge doses in SiGe alloy layers were measured from the spectra by integrating Ge signals and Si signals.

Ion channeling was performed in a <100> or <110> orientation after a random scattering yield was obtained. The channeling effect arises because rows or planes of atoms can steer energetic ions by means of a series of small-angle collisions resulting in very small amount of backscattering yields. When the specimen is slightly tilted from the right collimated orientation, channeling will be ruined by large-angle scattering events. Channeling measurements have three major applications in backscattering analysis: amount and depth distribution of lattice disorder, location of impurity or interstitial atoms in the lattice sites, and composition and thickness of amorphous surface layers. In the present work, the channeling was performed mainly for measuring amounts of lattice disordering. Ion channeling was useful because the strain-relaxed SiGe layer has high density of planar defects (stacking faults) which may effectively dechannel helium ions. Spectra in fig. 26 and fig. 32 show both random and channeled spectra in a SPE annealed SiGe alloy layer. The surface peak in the channeling spectra may be due to reconstructed surface atoms or a very thin surface layer of SiO_2 formed during nitrogen annealing. Backscattered signals from Si and Ge at the surface are indicated in the spectra, where the buried Ge peak is clearly recognized. The minimum backscattering yield, χ_{min}, was determined as a percentage ratio of channeled backscattering yield to random backscattering yield in the Si signal in the spectra.

Table. 2. RBS spectra conditions on each specimen

specimen	type of spectra	keV/channel	peak at% of elements, dose
RT, α5	random	3.86	5 at% Ge, 2E16/cm^2
RT, α5	<100> channel	3.86	5 at% Ge, 2E16/cm^2
LNT, α5	random	3.5	5 at% Ge, 2E16/cm^2
LNT, α5	<100> channel	3.5	5 at% Ge, 2E16/cm^2
LNT, α7	<110> channel	3.86	7 at% Ge, 3E16/cm^2
LNT, α12	random	3.86	12 at% Ge, 5E16/cm^2
LNT, α12	<100> channel	3.86	12 at% Ge, 5E16/cm^2
LN+SPE5	random	3.86	5 at% Ge, 2E16/cm^2
LN+SPE5	<110> channel	3.86	5 at% Ge, 2E16/cm^2
LN+SPE7	random	3.86	7 at% Ge, 3E16/cm^2
LN+SPE7	<110> channel	3.86	7 at% Ge, 3E16/cm^2
LN+SPE12	random	3.86	12 at% Ge, 5E16/cm^2
LN+SPE12	<110> channel	3.86	12 at% Ge, 5E16/cm^2
Ge+C.55	<110> channel	3.86	12 at% Ge, 0.55 at% C
Ge+C.9	random	3.5	12 at% Ge, 0.9 at% C
Ge+C.9	<110> channel	3.5	12 at% Ge, 0.9 at% C
Ge+C.3	<110> channel	3.5	12 at% Ge, 0.3 at% C

* A constant $^{4}He^{+}$ ion beam energy, 1.95 MeV was used. In specimen description, RT,α5 means as-implanted layer(RT) with 5 at% Ge peak. LN+SPE5 means the 5 at% Ge peak layer which is SPE annealed after LNT implantation. Ge+C.55 means a SPE annealed layer with 12 at% Ge and 0.55 at% C peaks.

Rutherford bachscattering spectrometry (RBS) analysis has a depth resolution which depends upon detector resolution, beam detector geometry, ion energy variation with depth, and the identity of elements in the target. Depth resolution refers to the ability to sense composition changes with depth variation. Just as the energy scale of detected particles is translated into a depth scale, the lowest resolvable energy can be translated into the smallest resolvable depth interval. From RBS spectra, the depth resolution of the system or the energy resolution at the specimen surface can be measured as $\delta E(=E_{88\%} - E_{12\%})$ shown in fig. 18. Since the energy resolution, δE is equal to $[S]\delta x$, the depth resolution, δx is worked out as $\delta E/[S]$ at the surface of the target, where [S] is called the energy loss factor or electronic stopping power that the projectile ions experience. When the specimen is properly tilted to increase the ingoing and outgoing path of the projectile ions, the effective depth resolution increases. [60] Under the SiGe analysis conditions of table. 2 and fig. 14, the depth resolution at the surface was found to be about 200Å, depending on the channeling direction, if the density of target material (SiGe) is assumed to be $5x10^{22}/cm^2$. The energy loss factor, [S] for <110> direction was about 82.25 eV/Å in calculation. [60] Besides depth resolution, RBS has limited mass resolution and limited sensitivity to trace elements in the target. Under the fixed analysis conditions of table. 2, however, the mass resolution limit is not critical. Moreover, because the implanted Ge dose is very high in this IBS work, the sensitivity limits can also be ignored. According to an empirical equation of Chu, [60] the minimum detectable Ge dose at 2MeV of $^4He^+$ ion energy is about $2x10^{13}cm^{-2}$.

3.4.2 Cross-sectional transmission electron microscopy (XTEM)

In order to observe the defect generation and the migration behavior of the a/c interface, XTEM studies were performed using a Philips 301 TEM in the Department of Materials Science and Mineral Engineering and a JEOL 200CX in LBL. Prior to XTEM observation, specimens were prepared according to the following steps and the illustrations in fig. 16:

1. Cleave the wafer.
2. Make a sandwich of two cleft wafers using an adhesive epoxy.
3. Slice the sandwich using a diamond saw.
4. Attach a slice on a polishing die using wax.
5. Polish one side of the slice using silicon carbide papers and diamond pastes.
6. Attach a Cu grid on the polished side using an adhesive epoxy.
7. Turn the polished side over and polish the other side of the slice.
8. Continue polishing until the polished slice is thin enough to produce a yellowish-red color under an optical microscope observation.
9. Ion-mill the thin specimen at liquid nitrogen temperature to produce a perforation.

For the adhesive, M-Bond 610, which can withstand high temperature, was used. Usual ion milling time was about 2 ~ 3 hours to finalize the sample preparation. The ion milling

rate for Si is estimated to be 9 μm/hour when two Ar^+ ion beams with 5 keV of energy are used at 15 degree of beam tilt. [61]

Ion milling was always performed at liquid nitrogen temperature to avoid beam heating effects.

Transmission electron microscope observations were performed by using <220> two beam conditions and symmetrical orientations along the <110> zone axis. The symmetrical conditions were used to measure the amorphous thicknesses in as-implanted specimens. A few plan-view TEM (PTEM) samples as well as XTEM samples were prepared to observe EOR dislocation loops remaining after LNT implantation followed by SPE annealing. The observed specimens are summarized in table. 3. The spatial resolution of the Philips 301 microscope was about 5Å and that of JEOL 200CX was about 2.5Å, at which resolution, lattice imaging could be performed. Mainly diffraction imaging was used in this work because diffraction contrast using the principle of vector product, $\mathbf{g} \cdot \mathbf{R}$ is the most convincing way to observe and analyze such lattice defects as stacking faults and EOR dislocation loops. [62] In the vector product, **g** is the reciprocal lattice vector associated with the real-space diffraction planes and **R** is the displacement vector of the lattice distortion induced by defects. If $\mathbf{g} \cdot \mathbf{R}$ is zero, no contrast will be obtained in image plane.

Table. 3. Prepared TEM specimens

Specimen	XTEM	PTEM	Annealing condition
RT,α5	yes	no	N/A
LNT,α5	yes	no	N/A
LNT,α12	yes	no	N/A
LN+SPE5	yes	yes	800°C , 1 hour
LN+SPE7	yes	no	800°C , 1 hour
LN+SPE12	yes	no	800°C , 1 hour
RT+SPE12	yes	no	800°C , 1 hour
Ge+C.55	yes	no	800°C , 1 hour
Ge+C.9	yes	yes	800°C , 1 hour
LN+SPE12'	yes	no	550°C , 1 hour
LN+SPE12"	yes	no	550°C , 5 hours

* Specimen description is same as used in RBS spectra except for LN+SPE12' and LN+SPE12" (partially regrown SiGe layers obtained from different annealing conditions). "yes" means that the specimen was prepared and observed. "no" means that the specimen was not prepared for TEM observation.

3.4.3 X-ray diffraction (XRD) using monochromatic crystal (Ge) rocking

Strain measurements were performed on various SiGe alloy layers after SPE annealing using XRD. A 4-bounce Ge crystal monochromator was used with Cu Kα radiation at a wavelength of 1.54Å. The smallest step angle allowed during a rocking-curve sweep in the XRD machine was 0.001 degree or 3.6 arcsec and diffracted X-ray signals from (400) planes of the SiGe samples were analyzed for calculating strains in the layers. Separate (400) peaks were obtained from Si and SiGe when the spectra were plotted on a logarithmic scale as shown in fig. 28. The difference between separate Bragg angles, $\Delta\theta$ has a fixed range between -800 and 100 arcsec in the spectra. Strain can be deduced from following equations when a tetragonal distortion is assumed:

$$\lambda = 2d \sin\theta = \text{constant} \tag{7}$$

If the derivative of equation (7) is taken,

$$\Delta d \sin\theta + d \cos\theta \, \Delta\theta = 0 \tag{8}$$

$$\varepsilon_T = \Delta d/d = -(\cos\theta / \sin\theta)\, \Delta\theta \tag{9}$$

where ε_T is a tetragonal strain, d is the distance between two (400) planes, θ is the Bragg diffraction angle from the planes, Δd is the difference between d_{Si} and d_{SiGe} which are the

interplanar spacings between two (400) planes in the Si substrate and the SiGe layer, respectively, while $\Delta\theta$ is the difference between two Bragg diffraction angles. Tetragonal strain or tetragnal distortion, ε_T is always bigger than the misfit strain and has the following relationship with misfit strain, ε_{misfit}:

$$\varepsilon_T = \varepsilon_{misfit}(1 + \nu)/(1 - \nu) \quad (10)$$

where ε_{misfit} is estimated as 0.042 X_{Ge}(Ge composition in Si). ν is the Poisson's ratio of a thin film layer grown on a substrate.

3.4.4 Raman spectroscopy

Raman spectroscopy was performed on the SiGeC alloy layer at room temperature using an Ar laser with a wavelength of 488nm. This experiment was done to confirm the substitutionality of sequentially-implanted C atoms. The analyzed sample had 12 at% Ge peak and 0.55 at% C peak at the same depth in the layer. Phonon absorption by the vibration of main lattice or local vibration were plotted as Raman shift from the incident photon energy and the scanning range of the Raman shift was 300 ~ 1000 cm^{-1}. The spectral resolution of Raman spectroscopy was 2 cm^{-1}. The phonon absorption process can be explained by following equations for the conservation of photon energy and momentum.

$$\omega=\omega'+\Omega \; ; \; k=k'+K \quad (11)$$

where Ω and K are phonon frequency and wavevector respectively. The incident photon from the laser has a frequency, ω, and a wavevector, k, while the emitted photon from a crystal with optical phonons shows different values of wavevector, k', and frequency, ω', due to phonon absorption or emission. All crystals are not Raman-active, but can be Raman-active if they have optical phonons. Because diamond cubic materials have optical phonons, signals from Si or SiGe can be expected in Raman spectra. [63] The difference (Ω) between ω and ω', is the Raman shift, which is measured.

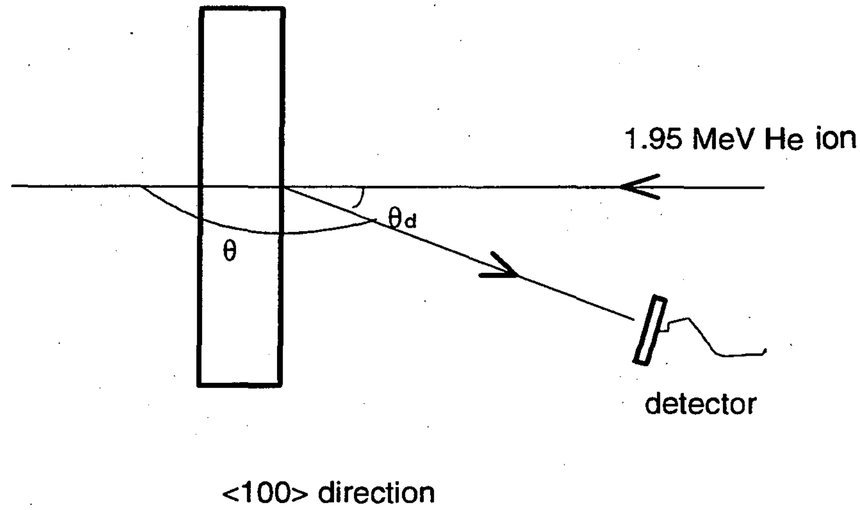

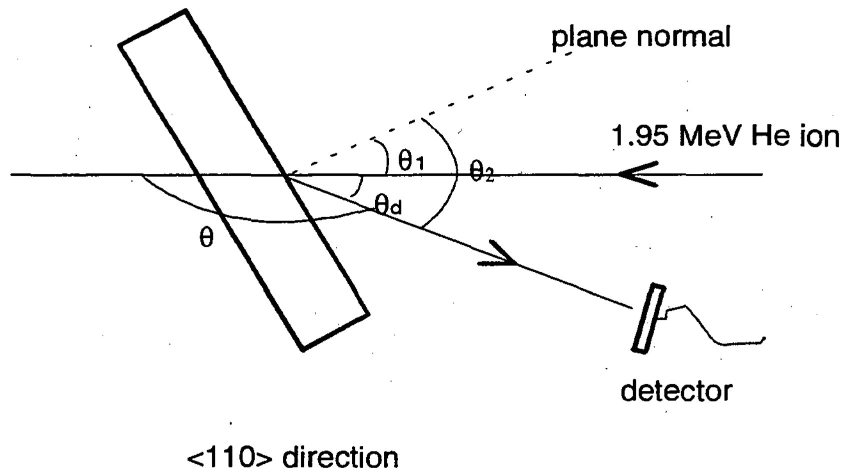

Fig. 14. Backsacttering conditions in RBS study. Scattering angle, θ is fixed as 165 degree and ion beam energy is 1.95MeV. Detector angle, θ_d is fixed as 15 degree. Tilt angle, θ_1 is 0 degree for normal <100> direction and 45 degree for <110> direction. Therefore, another geometrical angle, θ_2 is determined by summing θ_i to θ_d.

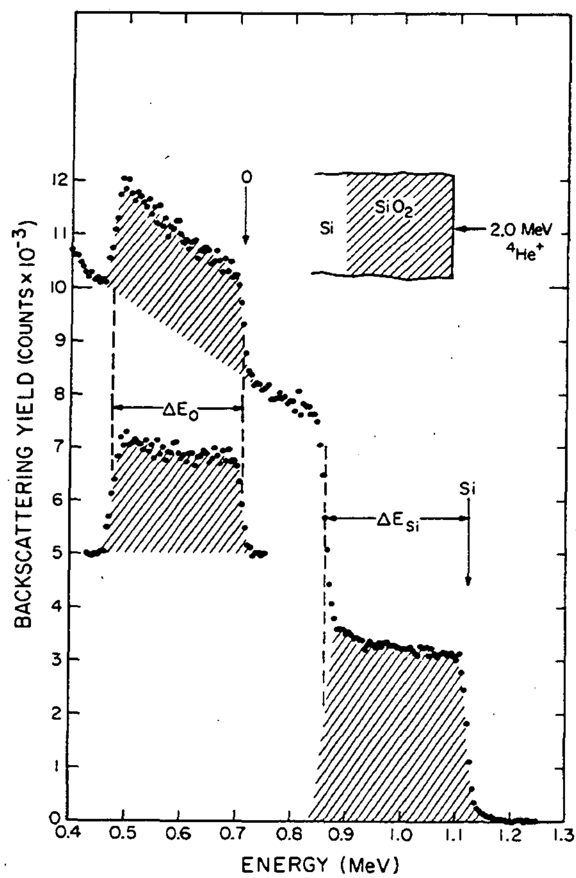

Fig. 15. Random backscattering spectra of SiO_2 film on Si substrate. 2 MeV $^4He^+$ ions are used. O signal and Si signal are integrated for composition determination. (After Chu[60])

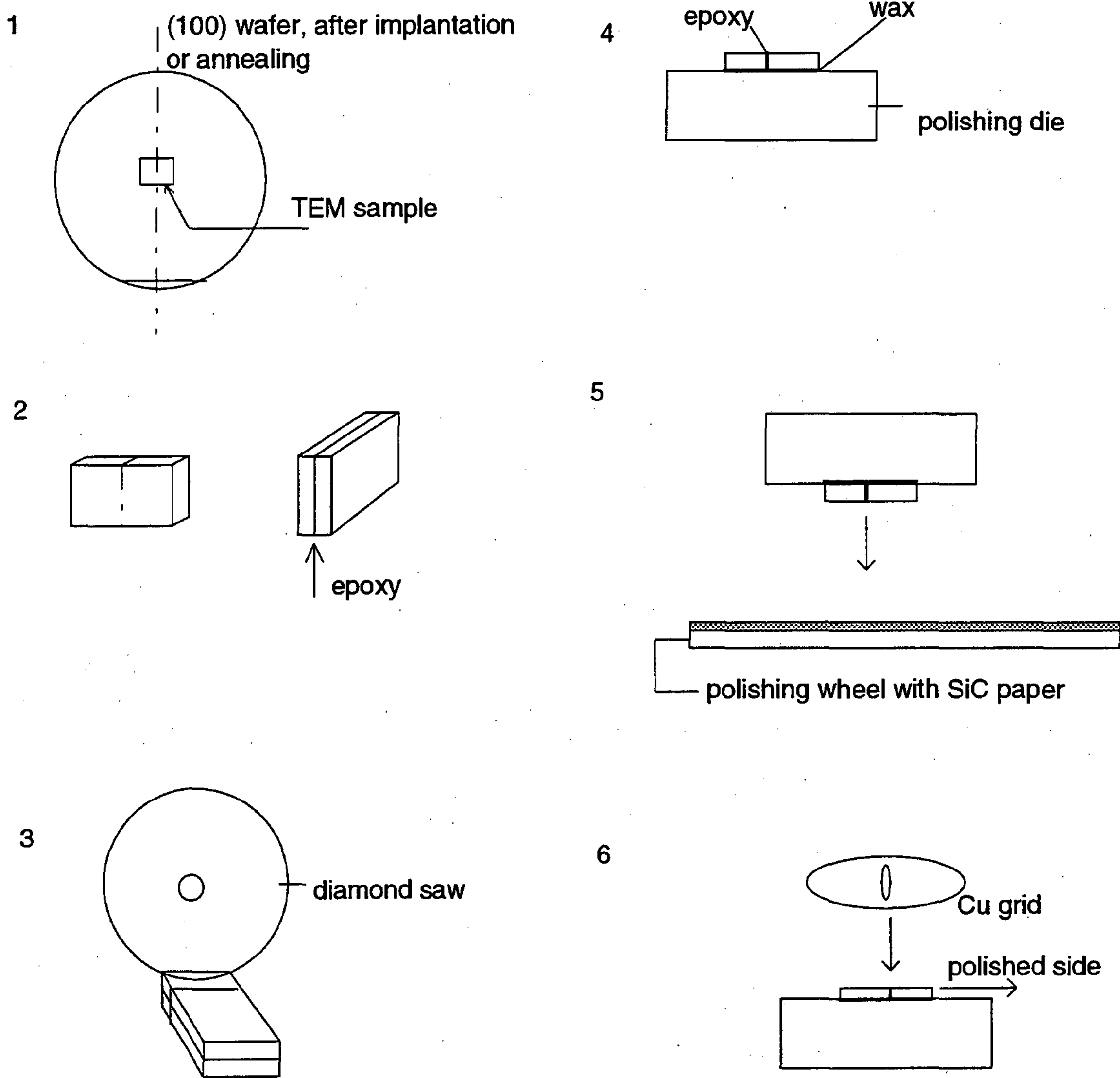

Fig. 16. Procedure of XTEM specimen preparation(1 ~ 6).

7

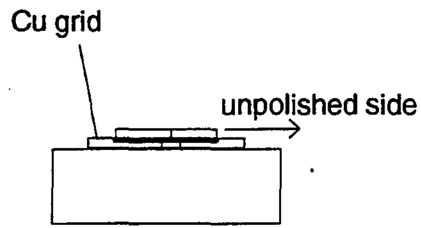

8

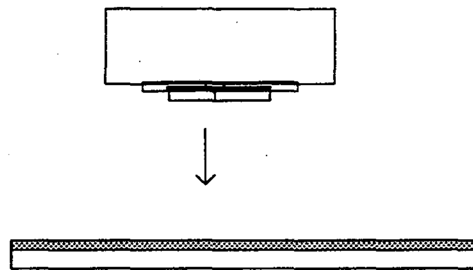

9

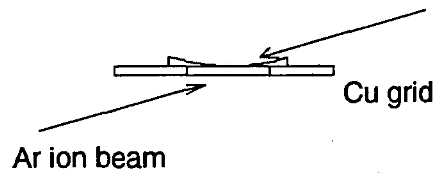

Fig. 16. Procedure of XTEM specimen preparation(7 ~ 9).

4. Results

4.1 Ge profiles in SiGe layers and layer thicknesses

As shown in fig. 17 and fig. 18, Ge concentration profiles of LNT implanted SiGe layers were obtained from Ge signals in the RBS spectra. The Ge peak concentration of a selected specimen, for example, was 7 at% and the corresponding dose was $3x10^{16}/cm^2$. The profiles were observed with both an as-implanted specimen and an annealed one as indicated in the plot of fig.17. They show a projected ion range (R_p) of 650Å to 700Å and an ion straggle of about 250Å to 300Å. These values slightly deviate from TRIM-simulated numbers in table 1 of the Appendix. In particular, R_p from the TRIM simulation is about 150Å larger than experimental value. However, if surface sputtering during Ge implantation is included, a smaller R_p is expected in experiment. Since the diffusivity of Ge is low at the annealing temperature of 800°C, it is reasonable that the Ge depth profiles before and after annealing do not show any significant redistribution in the plot of fig. 17. The SiGe layer thickness shown in fig. 17 is about 1700Å. The amorphous (α) layer thickness was also calculated to be about 1800Å from Si signals in <110> channeling spectra of the as-implanted specimen in fig. 18, while the Ge depth profile was obtained by converting the Ge signals in the spectra. For amorphous layer thickness calculations, full width half maximum(FWHM) of amorphous Si signal peak indicated in fig. 18 was converted into energy units and then the energy was converted to thickness using the energy loss factor (electronic stopping), [S] in Si. The energy loss factor, [S] was about 82.25 eV/Å as mentioned in section 3.4. Due to ion energy straggle,

the calculation of amorphous layer thickness using RBS spectra contains some amount of error which increases the depth resolution value, δx. [61]

4.2 Amorphized layer thickness and damage beyond a/c interface.

Amorphized layer thickness was measured again by using XTEM images, because the <110> ion channeling method has a low depth resolution. The smallest α thickness among all the SiGe layers was measured to be about 1550Å in the as-implanted SiGe layer (RT) with 5 at% Ge peak. Cross-sectional TEM micrographs in fig. 19 and RBS spectra in fig. 20 are used for the thickness measurement. In spite of the low depth resolution, a nearly identical amorphous thickness was obtained from RBS spectra and the XTEM micrograph. This may be because the thickness of interest in the present research is so thin that [S] does not change much in the layer. Symmetrical diffraction conditions were used in XTEM for more accurate measurement of thickness. An XTEM image with higher magnification in fig. 19(b) showed small dislocation loops of 100Å diameter beyond the a/c interface although the diffraction contrast method used for defect observation has a minimum identifiable diameter of dislocation loops in the 100Å range.[64] Because this layer was formed during RT implantation, any dynamical annealing effect was combined with the formation of interstitial clusters; these are the origin of EOR loops as mentioned in Chaper 2. It is well known that large clusters of recoiled interstitials are converted into extrinsic stacking fault loops by dynamical annealing or SPE annealing. [33,34] These dynamical annealing effects can be reduced by employing LNT implantation instead of RT implantation. [35,36,65] The XTEM micrograph in fig. 21 shows the

amorphous thickness and a/c interface obtained by using LNT implantation with the same dose as used in RT implantation. A thicker amorphous layer of about 1700Å was obtained and the substrate near the a/c interface did not show any recognizable dislocation loops but tiny dots, which are likely to be small clusters obscured by the resolution limits of the Philips 301. The initial signature of lattice damage is expected to increase in magnitude and become large dislocation loops after high temperature annealing as mentioned in Chapter 2. The Ge dose as well as the temperature were seen to affect the α layer thickness. These effects was experimentally observed in the present work by XTEM and RBS. A plot in fig. 22 shows the Ge dose dependence of the amorphous layer produced during LNT implantation. The LNT-implanted layer with 12 at% Ge peak showed a 2000Å amorphous layer thickness as measured by RBS channeling and XTEM micrograph in fig. 23. The XTEM image inset in the RBS channeling spectra also shows no lattice defects beyond the a/c interface as a result of LNT implantation.

4.3 EOR dislocation loops in SPE regrown layers

The EOR loops in both LNT and RT implanted SiGe layers were observed after annealing at 800°C for 1 hour. As shown in the XTEM micrograph in fig. 24(a), a RT-implanted SiGe layer with 5 at% Ge peak showed a high density of EOR dislocations after recrystallization while an LNT-implanted layer showed a considerably reduced density of dislocations. In the XTEM micrograph of fig. 24(b), similar results were shown in the other RT-implanted SiGe layer with 12 at% Ge peak, although the layer showed

not only EOR loops in high density but also strain-induced stacking faults developed from about 700Å depth. However, LNT-implanted SiGe layers revealed a minimized density of EOR loops as shown in the XTEM micrographs of fig. 25. These results could be anticipated from the observation of as-implanted specimens discussed in 4.2, because the density of EOR loops depends on the density of supersaturated Si interstitials beyond the a/c interface as explained in 2.1.5.

4.4 Strain-induced stacking faults in SPE regrown SiGe layers

Strain-induced stacking faults with misfit dislocations showed up in the SiGe layers with more than 7 at% Ge peak. The three micrographs shown in fig. 25 present the SPE regrown SiGe layers with different Ge peak concentrations. They were LNT implanted layers and the layer with only 5 at% peak did not show any stacking fault and a small amount of EOR dislocation loops. These results were also confirmed by <110> ion channeling. The two spectra in fig. 26 represent the channeling results obtained from SiGe layers with 5 and 7 at% Ge peaks. The layer with 5 at% Ge peak showed very good crystallinity with a low χ_{min}(= 5%) while the layers with 7 at% Ge peak had a χ_{min} of about 9 to 10%. A plot in fig. 27 shows the dependence of χ_{min} on Ge peak concentrations in SPE grown layers. Note that the χ_{min} of a pure Si wafer is 3.5% in <110> ion channeling. As confirmed in both ion channeling and XTEM observation, there is a threshold peak concentration of Ge at about 6 at% for the generation of misfit dislocations and stacking faults. X-ray diffraction (XRD) using rocking crystals shows a secondary (400) peak for a strained or commensurate SiGe layer with 5 at% Ge peak in a

diffraction spectra of fig. 28. Measured mean tetragonal strain(ε_T) from the secondary peak was about 0.25% which could be converted into 0.14% of misfit strain (ε_{misfit}) using equation (10) with a Poisson's ratio of Si (ν=0.27). From the X-ray diffraction spectra, the residual strain is shown to be compressive because the $\Delta\theta$ in arcsec is negative. The peak intensity is about hundred times smaller than main Si substrate peak, comparable to previous reports. [66] Due to the nonuniformity of the strain in the SiGe layer, the peak was somewhat broad, but there is no doubt that the layer with 5 at% Ge peak is commensurate with compressive residual strain as is observed in the XTEM results of fig. 25.

4.5 Regrowth behavior of SiGe alloy layers

The XTEM micrographs in fig. 29 show the results from low temperature (550°C) annealing of SiGe layers with 12 at% Ge peak for 1 and 5 hours. Regrowth was incomplete after these annealing conditions. The a/c interface grows in a planar mode up to a certain height from the initial position but then changes growth morphology from that height on, breaking the planar morphology into a faceted one. Moreover, the regrowth rate near the Ge concentrated region is considered very slow compared with the initial regrowth rate of SPE. Note that the initial growth rate is at least 1000Å/hour while the rate goes down to less than 100Å/hour as deduced from the XTEM results. The break point was about 800Å below the wafer surface. A high resolution XTEM image in fig. 30 clearly shows the region and the stacking faults generated near the region. The stacking

faults are developed from the Ge peak concentration region and one end of the stacking faults is terminated at an a/c interface.

4.6 SiGe layers SPE-regrown after C sequential implantation

XTEM micrographs in fig. 31(a) and fig. 31(b) show SiGe layers with C concentrations and 12 at% Ge peak in the layers. Stacking faults were considerably reduced in density, compared to the SiGe layers with no C but high Ge peak concentration (fig. 31(c)). One layer in fig. 31(a) has 0.55 at% peak C and another layer in fig. 31(b) has 0.9 at% peak C. Only the surface region of the layers shows a limited amount of stacking faults due to strain relaxation. Fewer stacking faults were shown in the SiGe layer with 0.9 at% C peak than the layer with 0.55 at% C peak. The <110> ion channeling spectra in fig. 32 reconfirm the results from XTEM micrographs in fig. 31. A χ_{min} of 5% was obtained from the spectra with C peak of 0.9 at%. However, 15% (= χ_{min}) was obtained from a SiGe layer with 0.3 at% C and 12 at% Ge as shown in a plot of χ_{min} vs. C peak concentration (fig.33). It is likely that there is also a threshold C peak concentration to suppress the generation of stacking faults or misfit dislocations, as similar results of a threshold Ge peak concentration were shown in 4.4 and fig. 27. Therefore, from both ion channeling and XTEM, the best crystallinity is obtained from the SiGe layer with 0.9 at% C peak, in the present experimental specimen series.

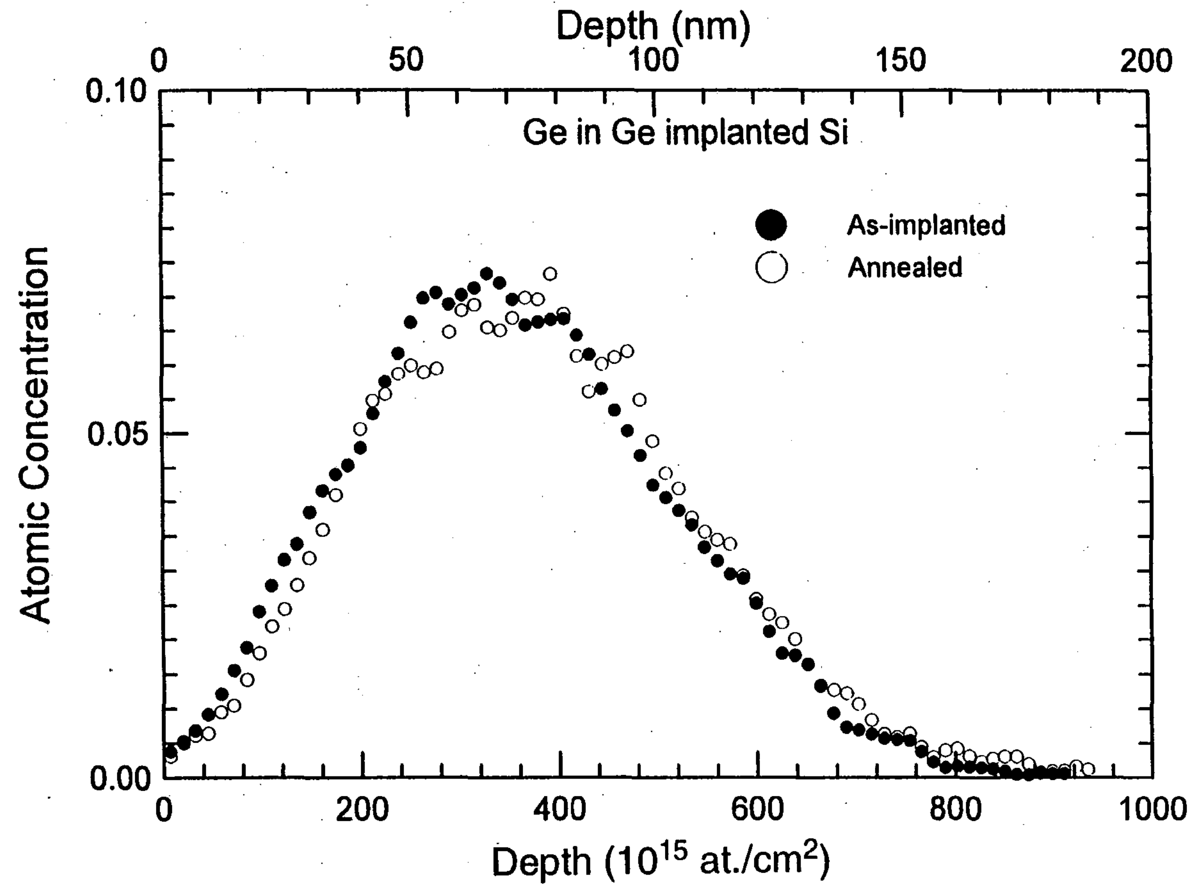

Fig. 17. Ge distribution in LNT-implanted SiGe layer with Ge dose, $3x10^{16}/cm^2$. Ge peak concentration was 7 at% and after SPE annealing, Ge redistribution was negligible.

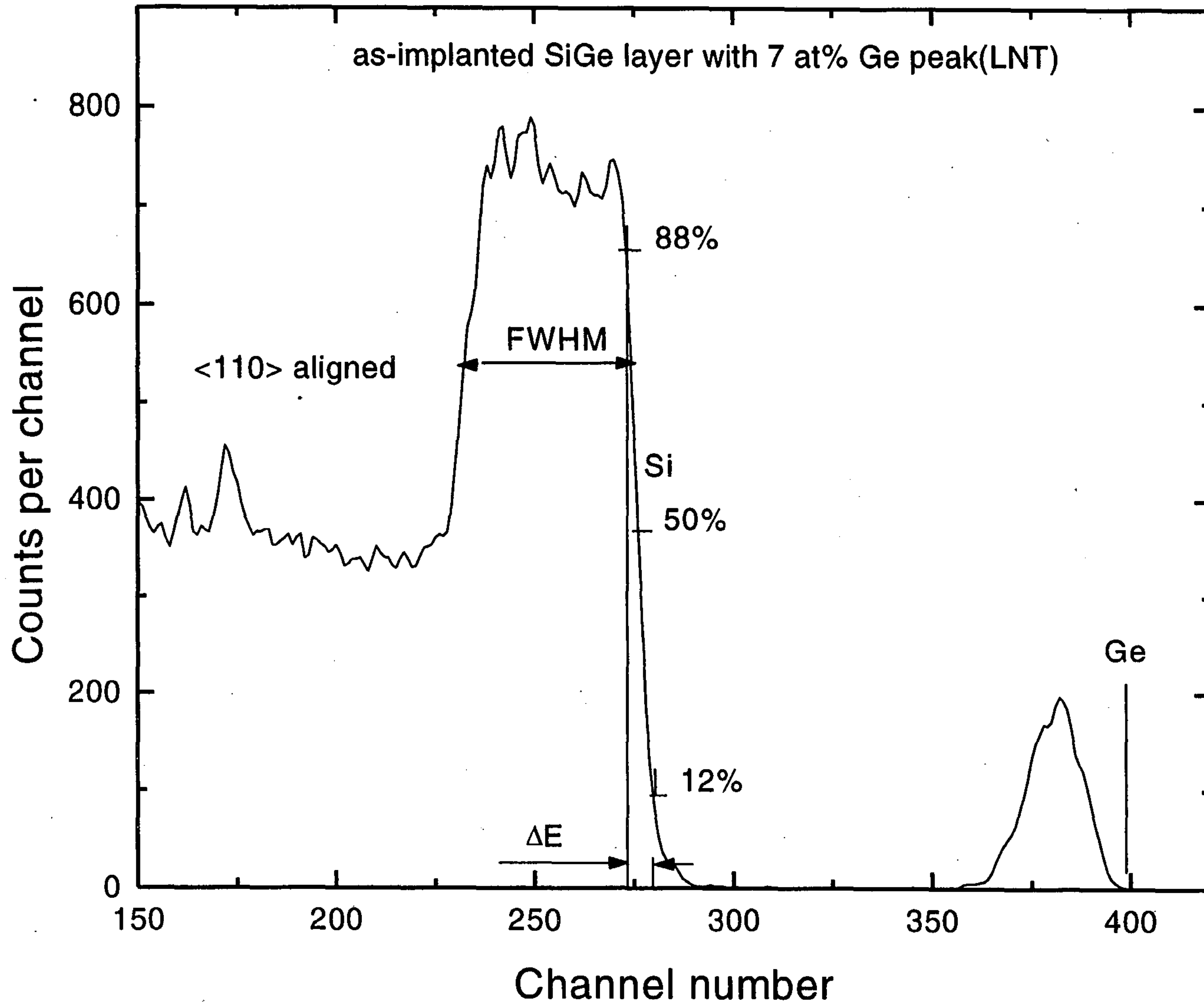

Fig. 18. <110> ion channeling spectra of as-implanted SiGe layer (LNT) with a dose, $3x10^{16}/cm^2$.

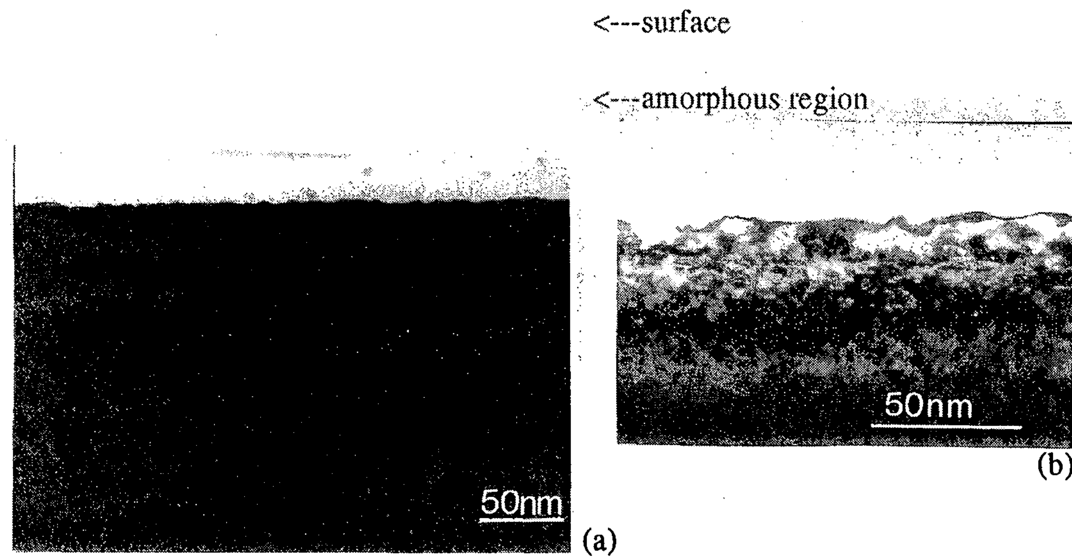

Fig. 19. XTEM micrographs show the a/c interface and α-layer thickness in the RT-implanted SiGe layer with 5 at% Ge peak. Micrograph (b) with higher magnification than (a) shows very small dislocation loops dynamically formed beyond the a/c interface.

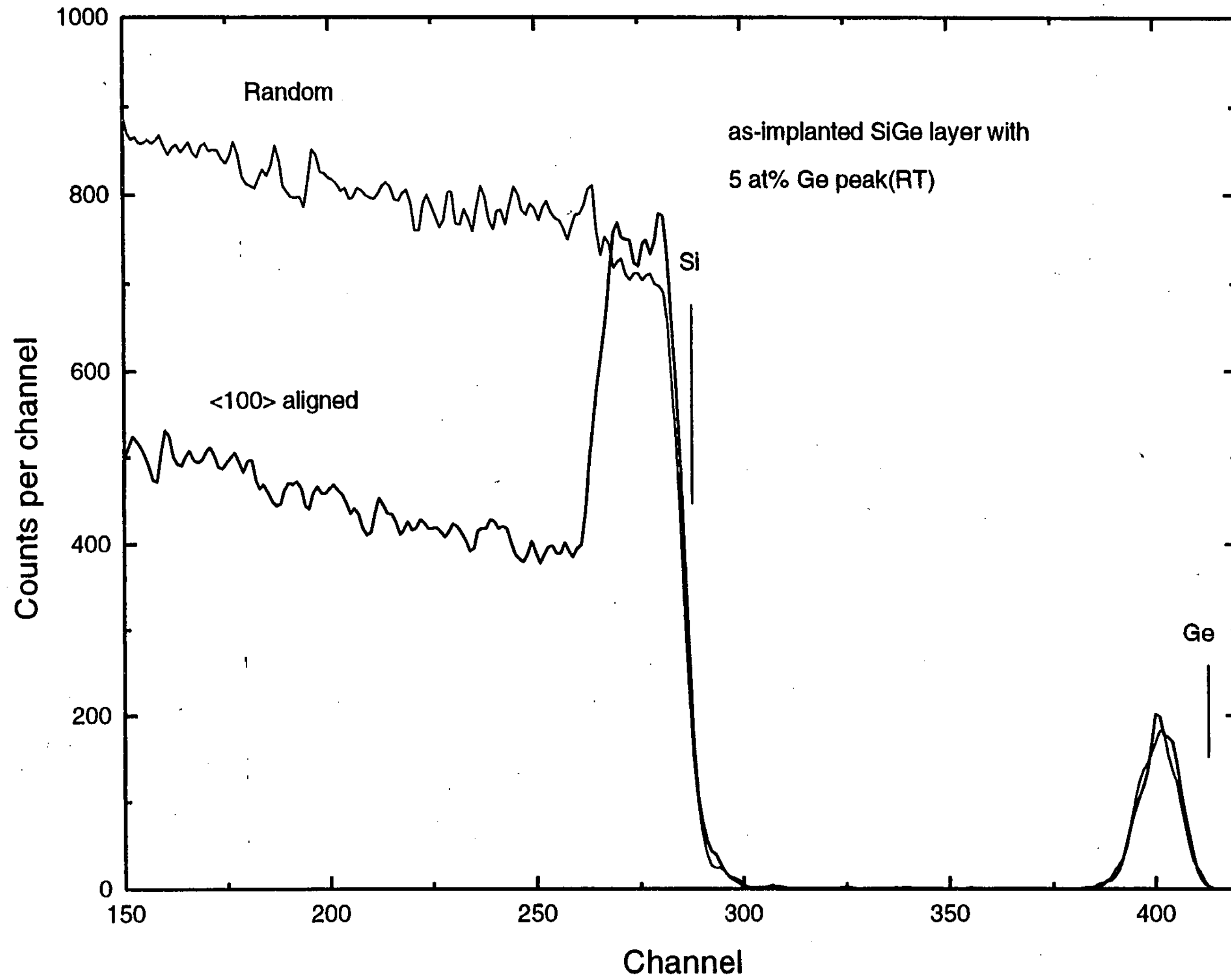

Fig. 20. Random and <100> ion channeling spectra of as-implanted SiGe layer (RT) with a dose, $2x10^{16}/cm^2$.

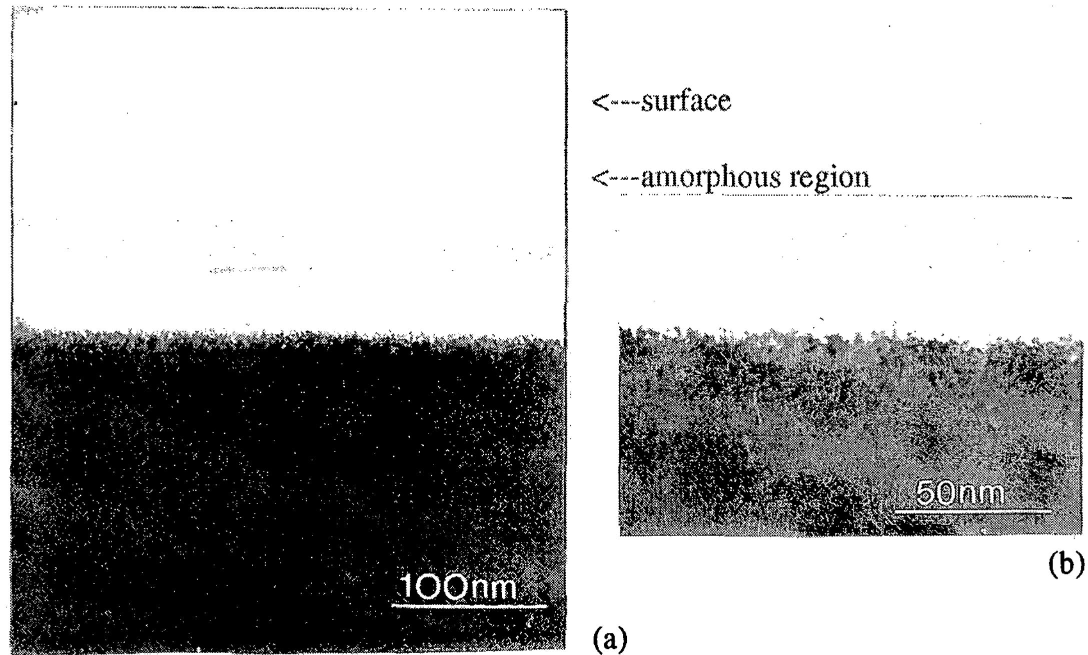

Fig. 21. XTEM micrographs show the a/c interface and α-layer thickness in the LNT-implanted SiGe layer with 5 at% Ge peak. Micrograph (b) with a higher magnification shows no dislocation loops but small dots beyond the a/c interface. Thickness was thicker than α-layer thickness formed by RT-implantation.

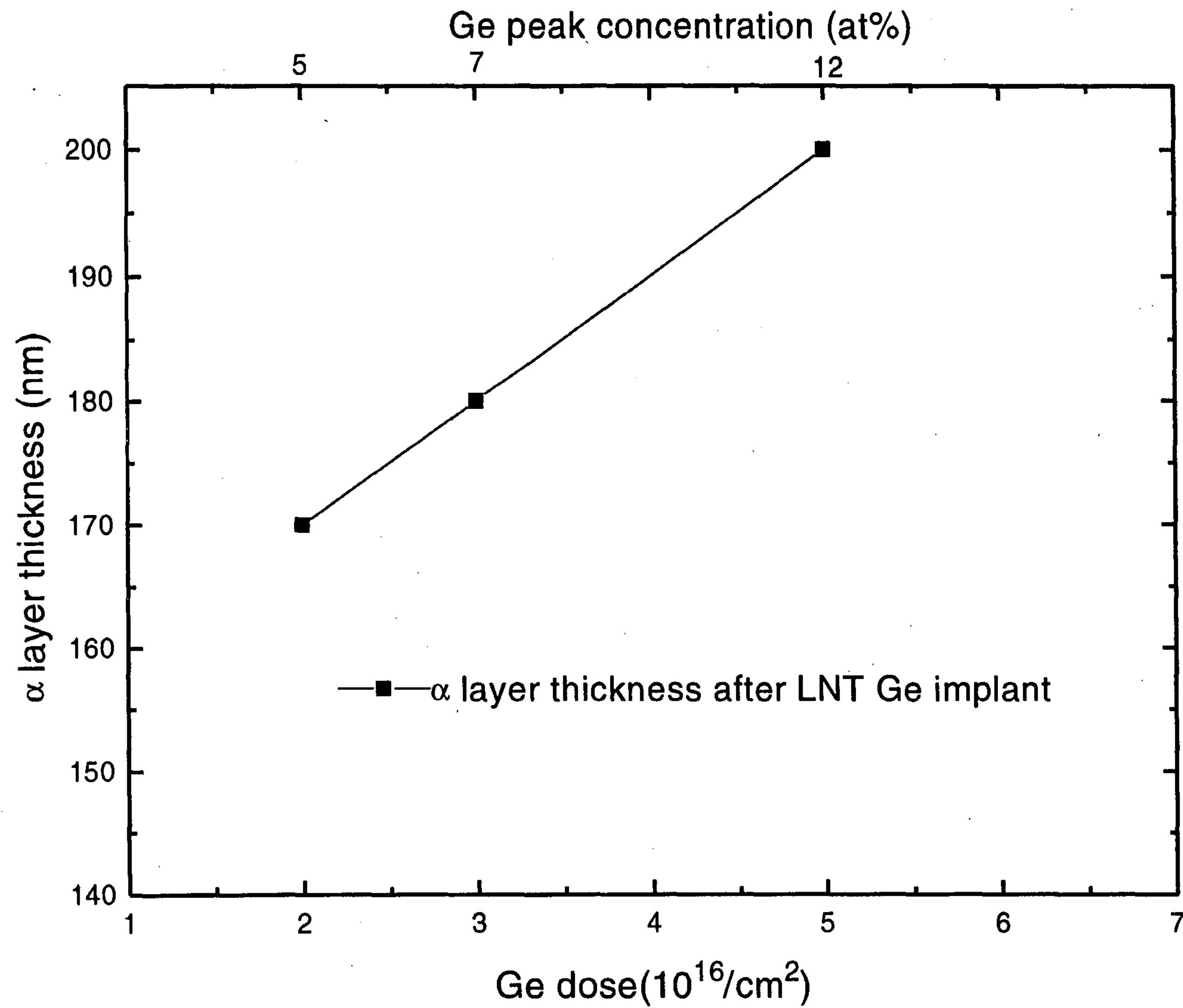

Fig. 22. Plot of α-layer thickness vs. Ge dose in LNT-implanted SiGe layers.

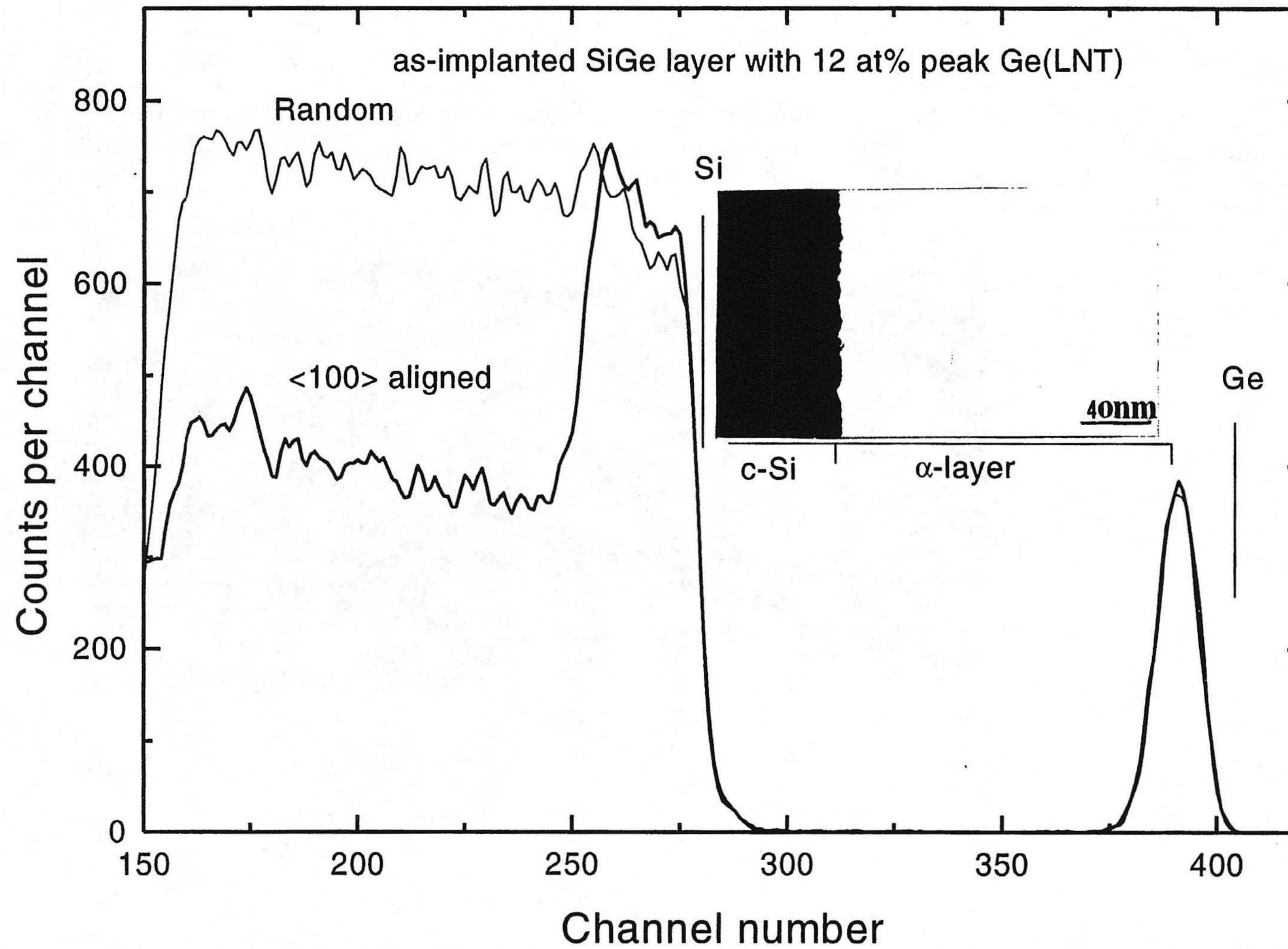

Fig. 23. Random and <100> ion channeling spectra of as-implanted layer with a dose, $5x10^{16}/cm^2$. Inset is a corresponding XTEM image of α-SiGe layer on a Si substrate.

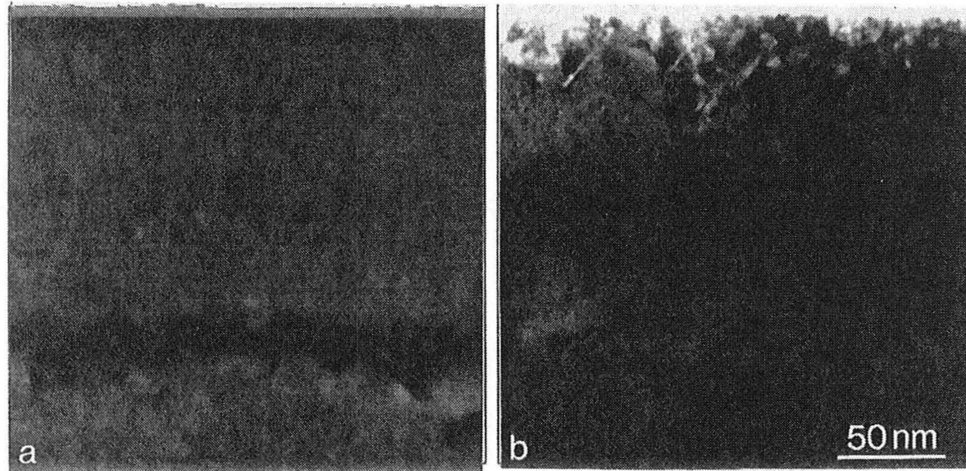

Fig. 24. XTEM micrographs of SPE-grown SiGe alloy layers annealed at 800°C for 1 hour after RT implantation. (a) Ge dose = $2x10^{16}$ cm^{-2} (5 at% Ge peak), (b) Ge dose = $5x10^{16}$ cm^{-2} (12 at% Ge peak).

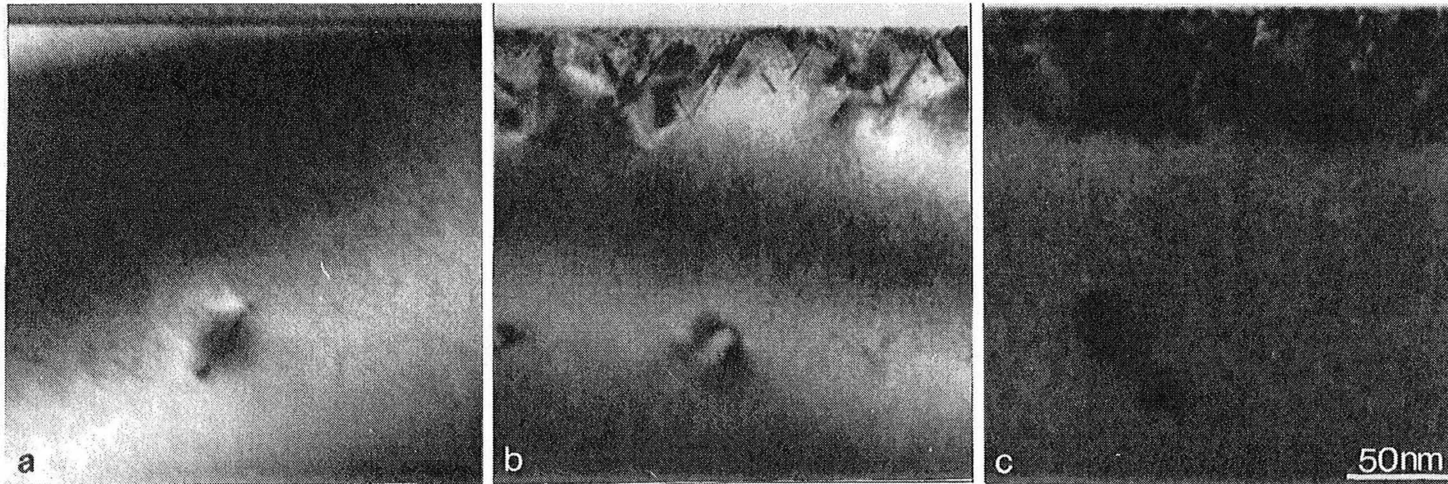

Fig. 25. XTEM micrographs of LNT-implanted SiGe layers after SPE annealing at 800°C for 1 hour.
(a) Ge dose = $2x10^{16}$ cm^{-2} (5 at% Ge peak), (b) Ge dose = $3x10^{16}$ cm^{-2} (7 at% Ge peak).
(c) Ge dose = $5x10^{16}$ cm^{-2} (12 at% Ge peak).

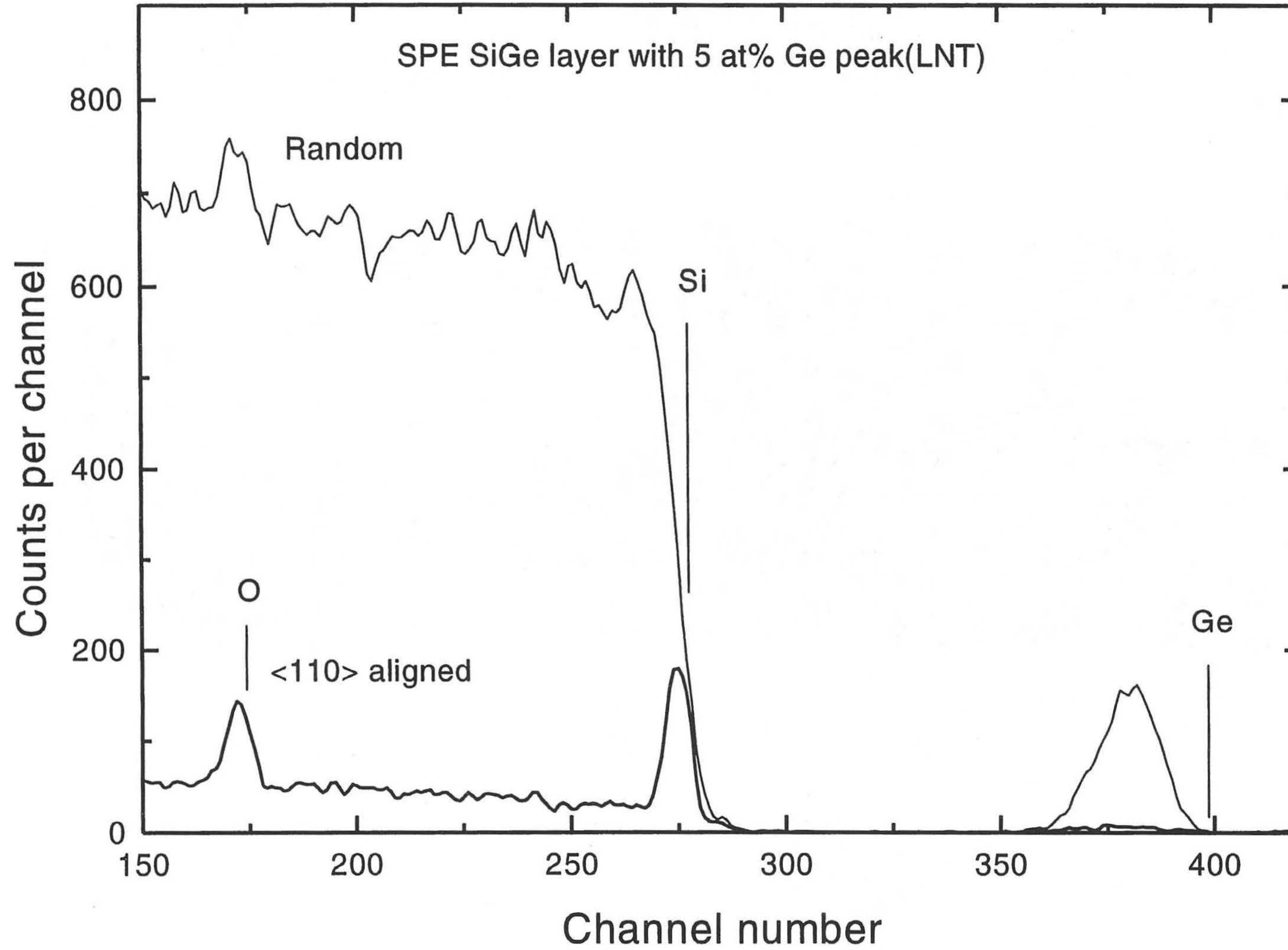

Fig. 26 (a). Random and <110> ion channeling spectra of SPE SiGe layer with 5 at% peak Ge.

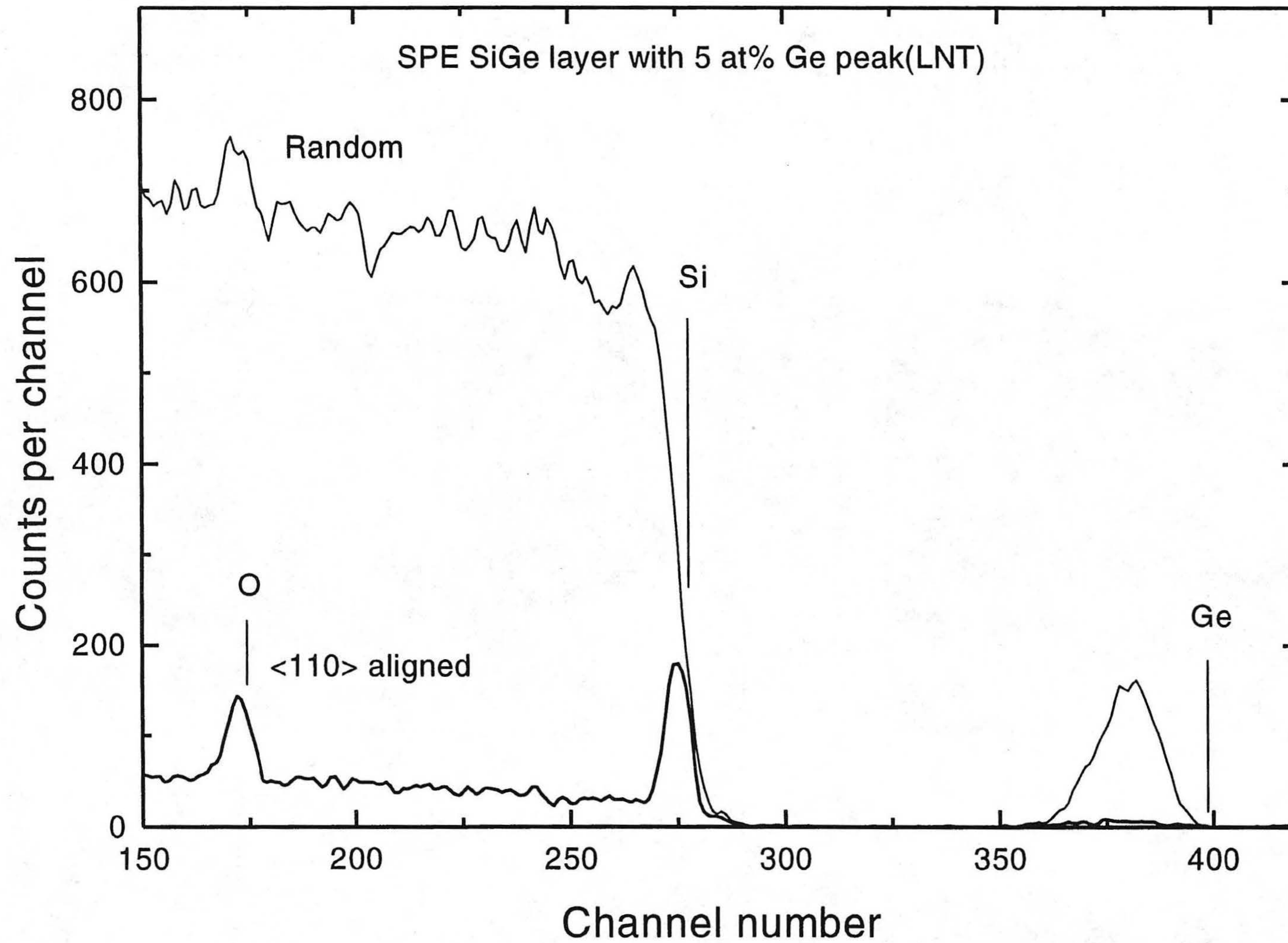

Fig. 26 (a). Random and <110> ion channeling spectra of SPE SiGe layer with 5 at% peak Ge.

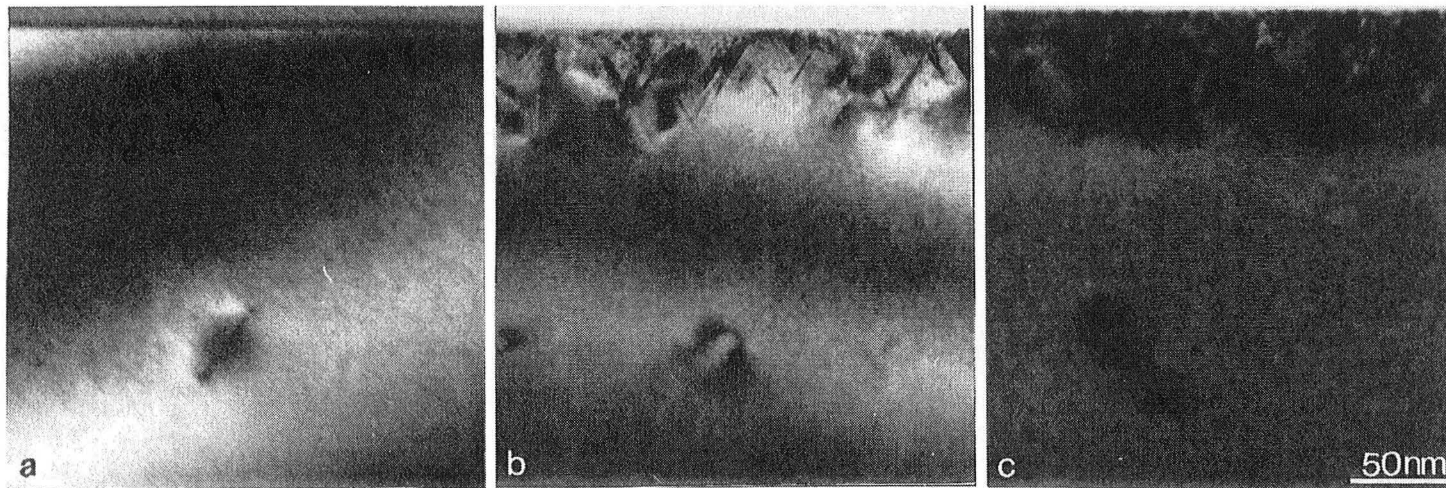

Fig. 25. XTEM micrographs of LNT-implanted SiGe layers after SPE annealing at 800°C for 1 hour.
(a) Ge dose = $2x10^{16}$ cm^{-2} (5 at% Ge peak), (b) Ge dose = $3x10^{16}$ cm^{-2} (7 at% Ge peak).
(c) Ge dose = $5x10^{16}$ cm^{-2} (12 at% Ge peak).

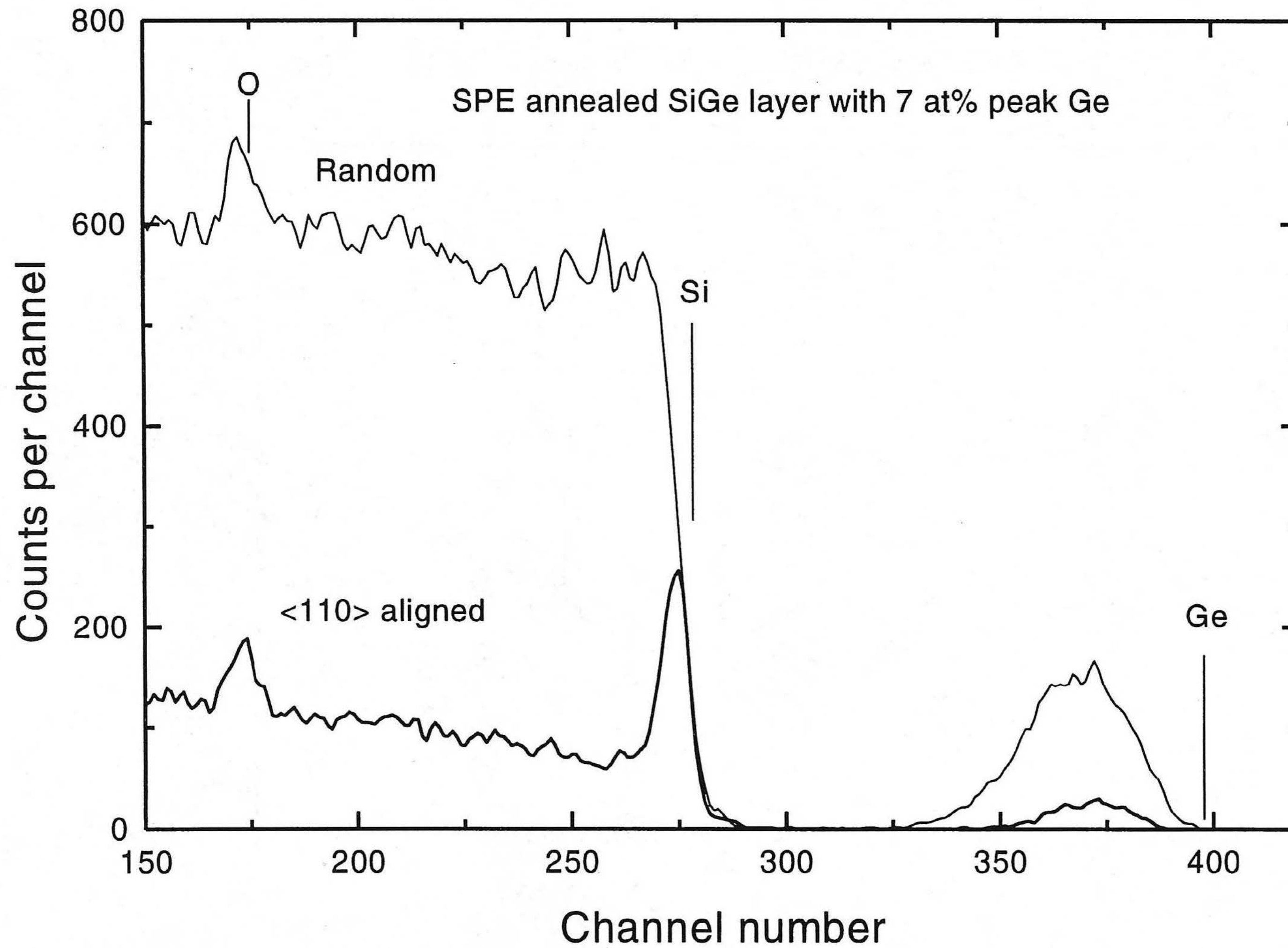

Fig. 26 (b). Random and <110> ion channeling spectra of SPE SiGe layer with 7 at% peak Ge.

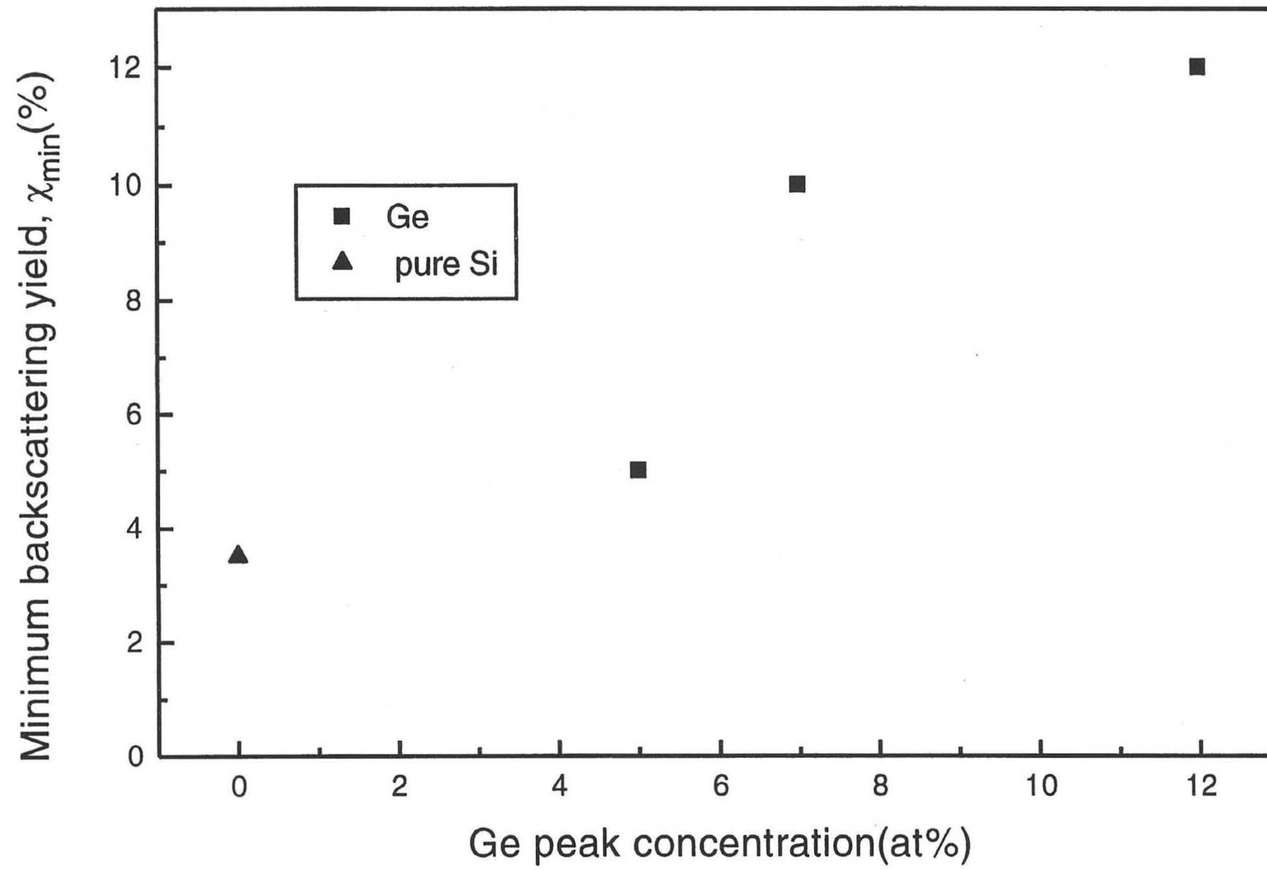

Fig. 27. Plot of χ_{min} vs. Ge peak concentration in SPE regrown layers

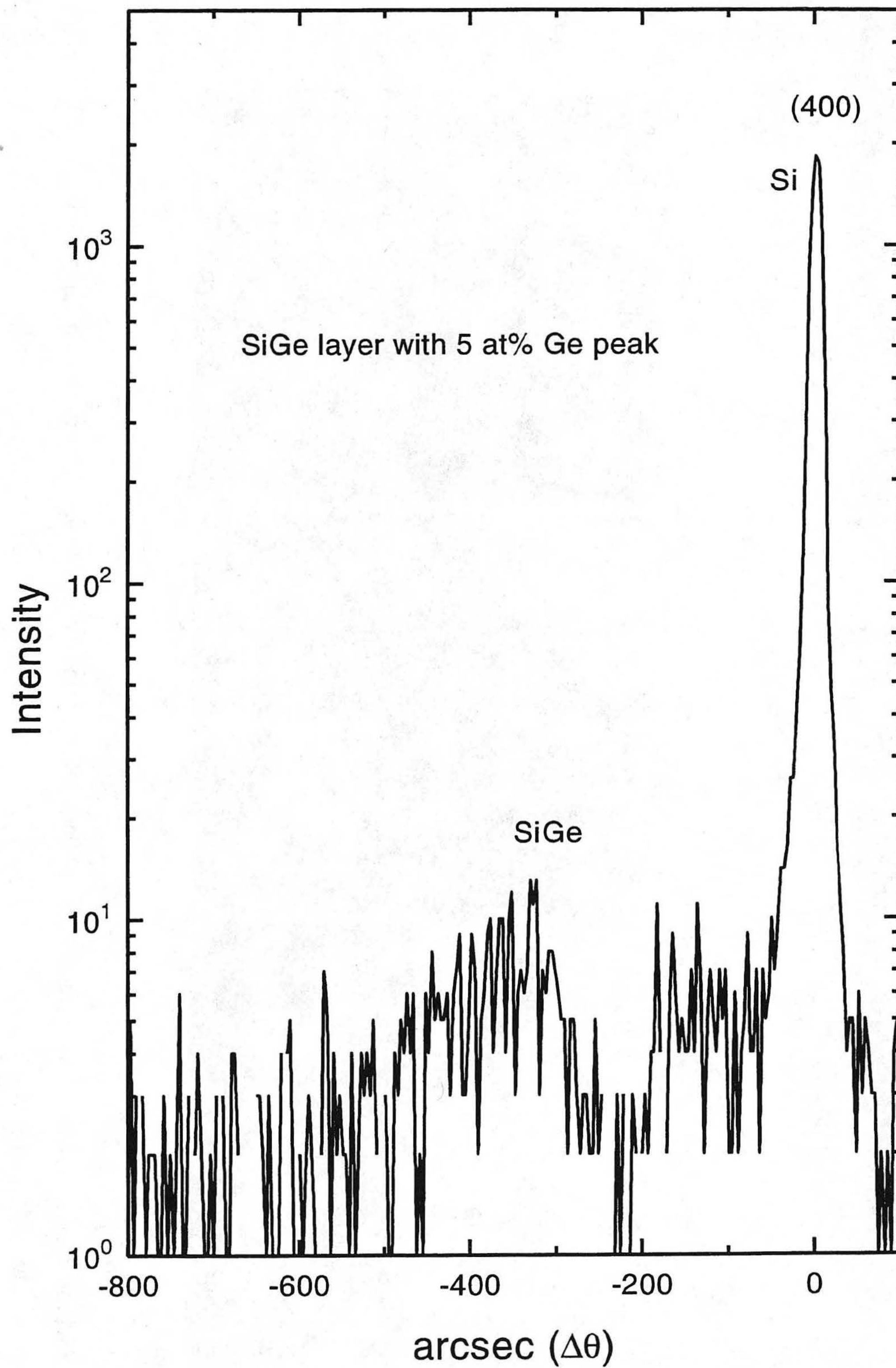

Fig.28 X-ray diffraction results obtained from SPE grown SiGe layer with 5 at% Ge peak. Rocking curve is plotted in intensity vs. arcsec(Δθ).

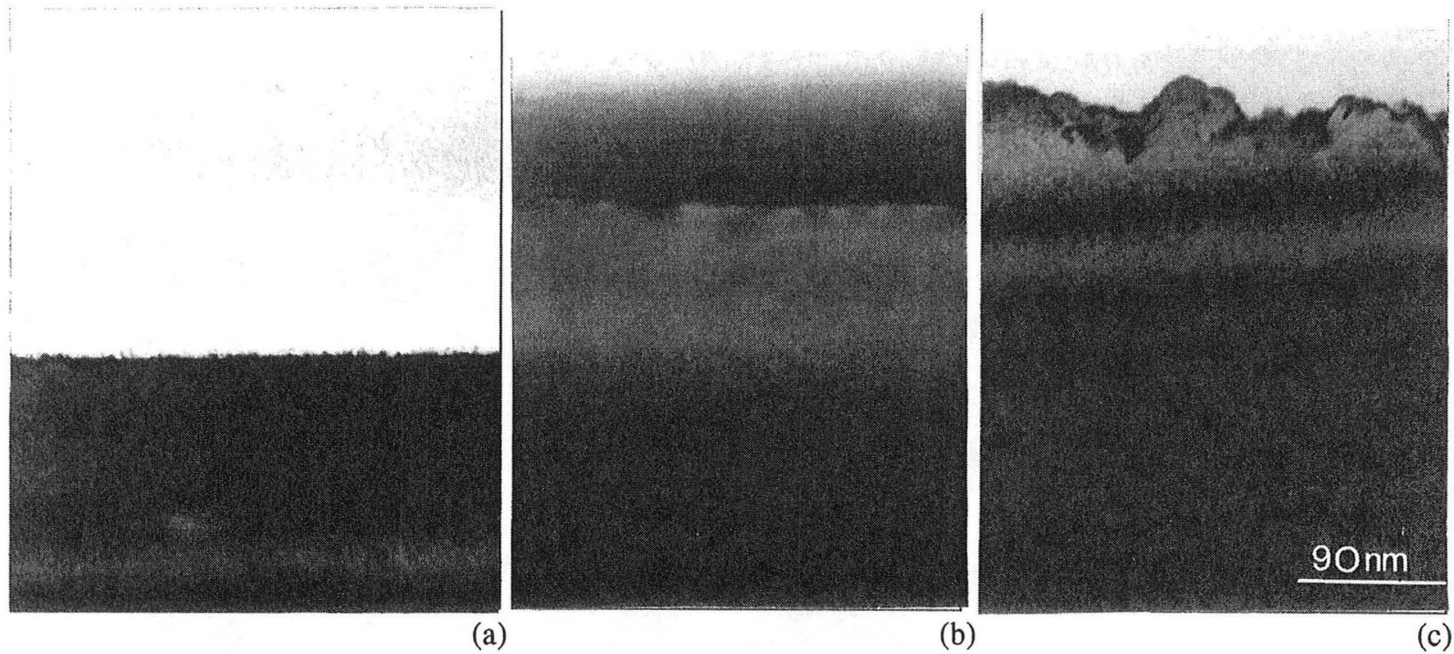

Fig. 29. XTEM micrographs showing the morphological change of the migrating a/c interface during SPE regrowth of SiGe layer with 12 at% Ge peak. The regrowth annealing was done at a temperature of 550°C for (b) 1 hr and, (c) 5 hrs. Micrograph (a) shows the as-implanted amorphous thickness.

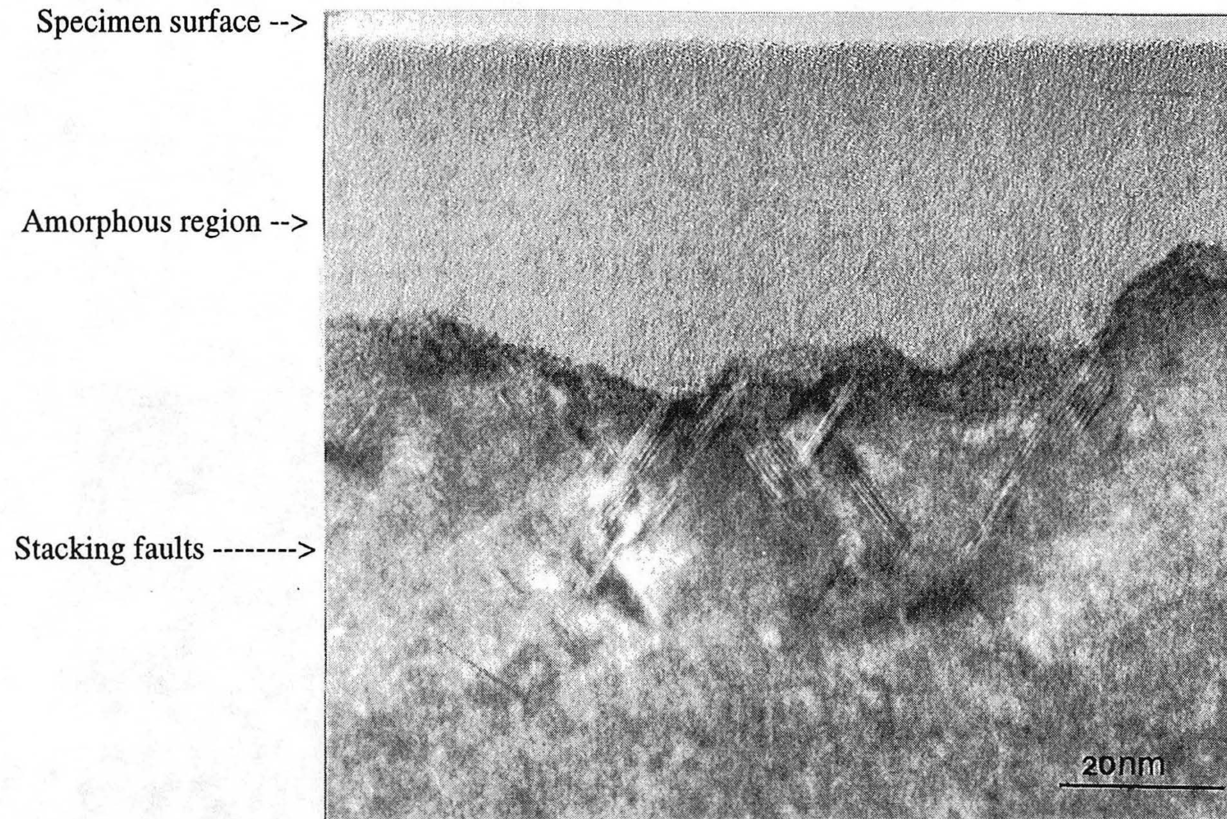

Fig. 30. XTEM micrograph showing partial regrowth of LNT-implanted SiGe layer with 12 at% Ge peak. Annealing condition was 550°C for 5 hours. Stacking faults are observed under the migrating a/c interface.

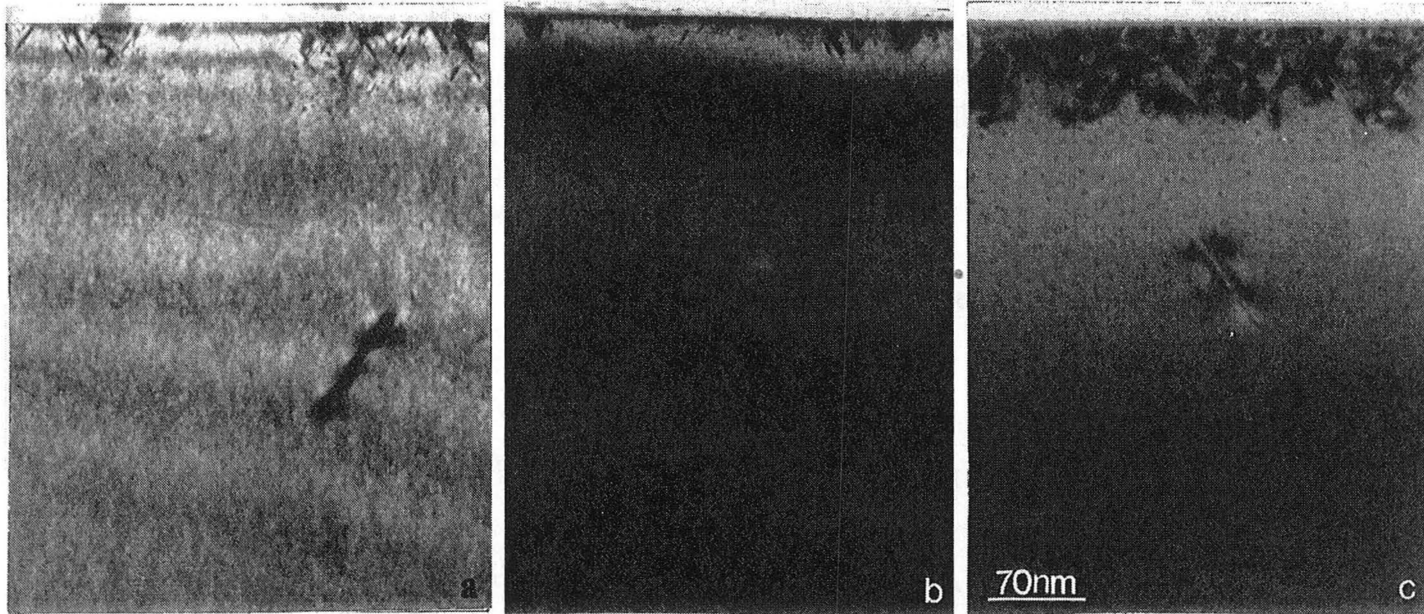

Fig. 31. XTEM micrographs of SPE regrown SiGe layers with 12 at% Ge peak and (a) 0.55 at% C peak, (b) 0.9 at% C peak, (c) no C concentration.

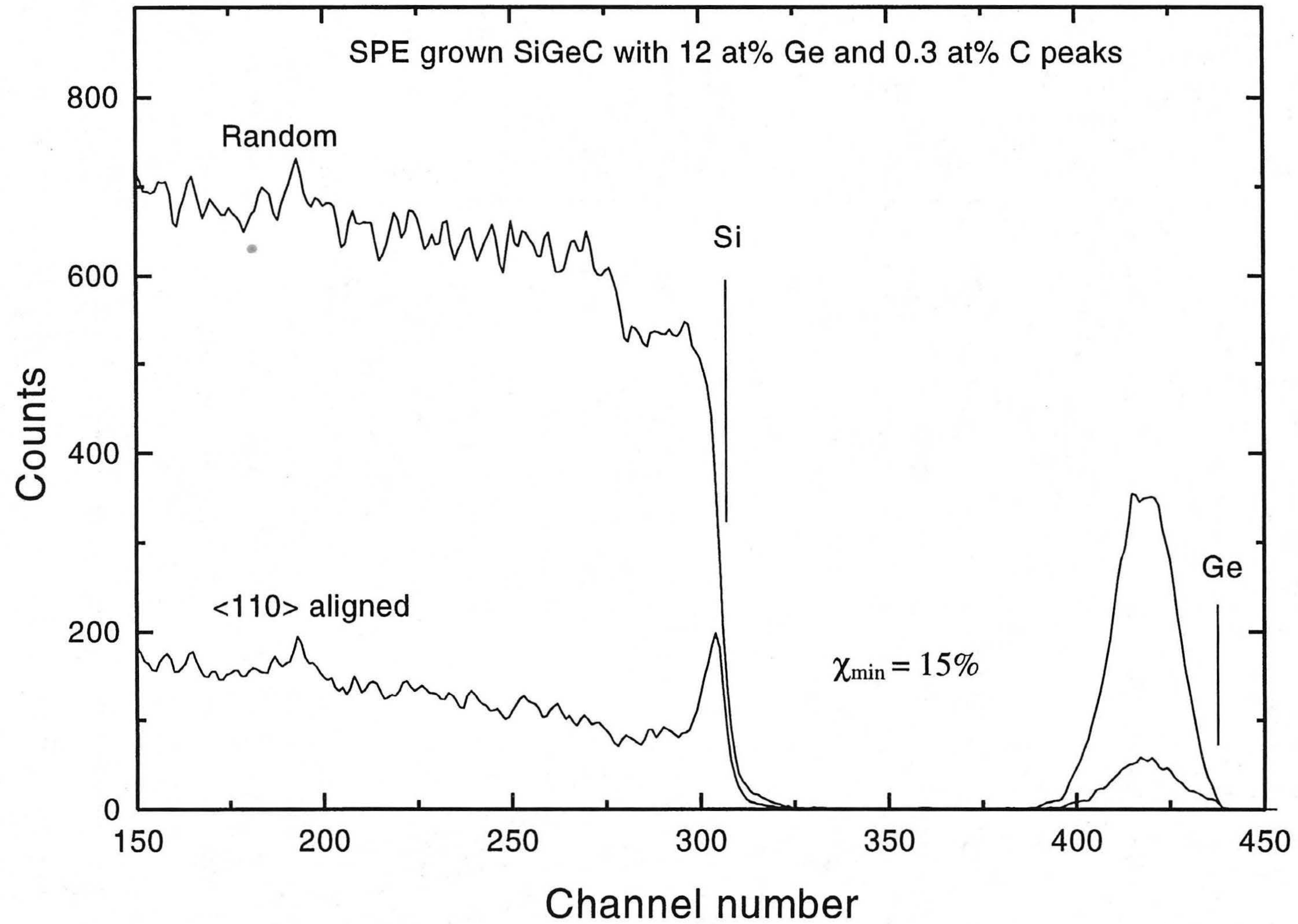

Fig. 32(a). Random and <110> ion channeling spectra of SPE grown SiGeC layer (12 at% Ge and 0.3 at% C peaks).

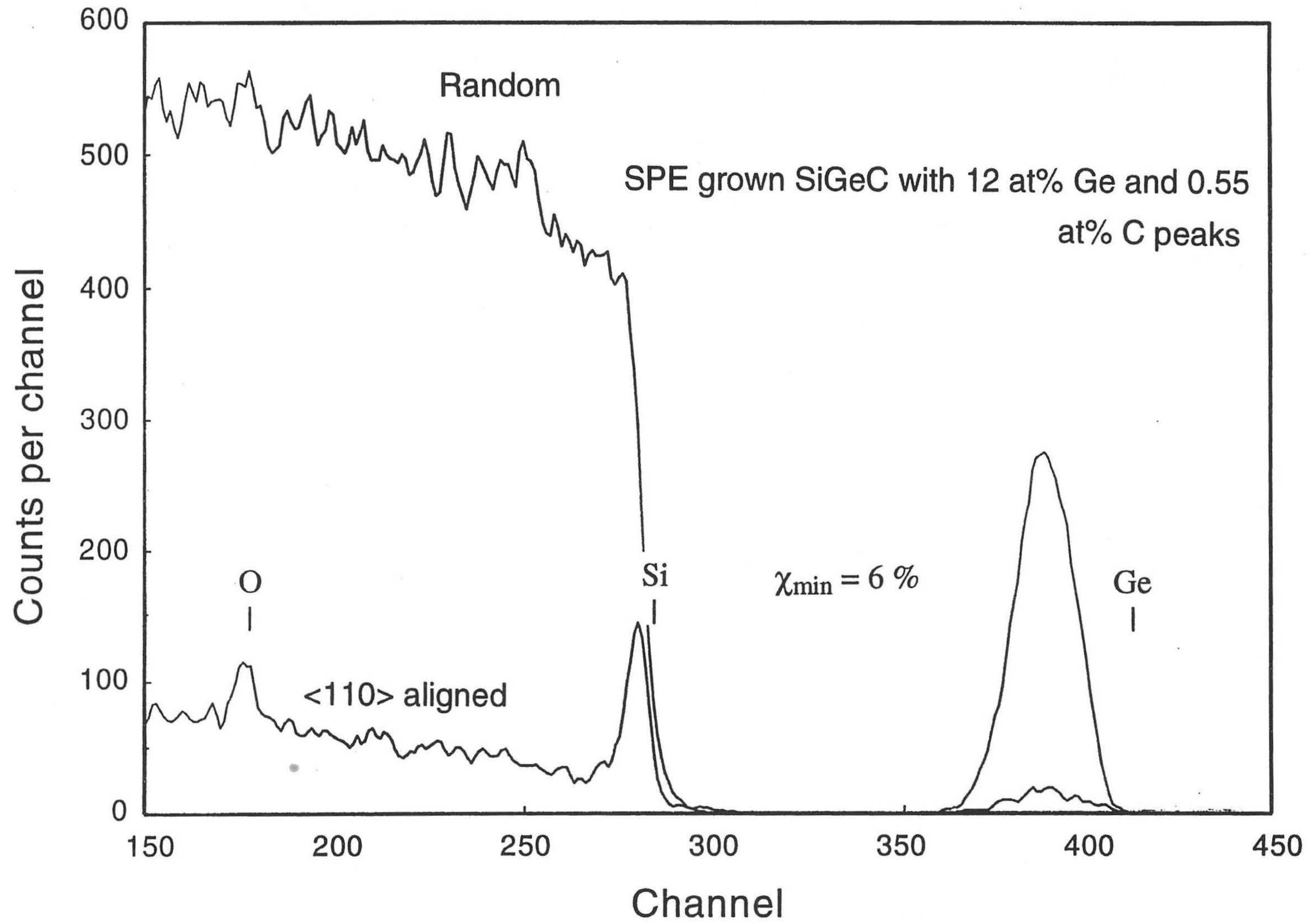

Fig. 32(b). Random and <110> ion channeling spectra of SPE grown SiGeC layer (12 at% Ge and 0.55 at% C peaks).

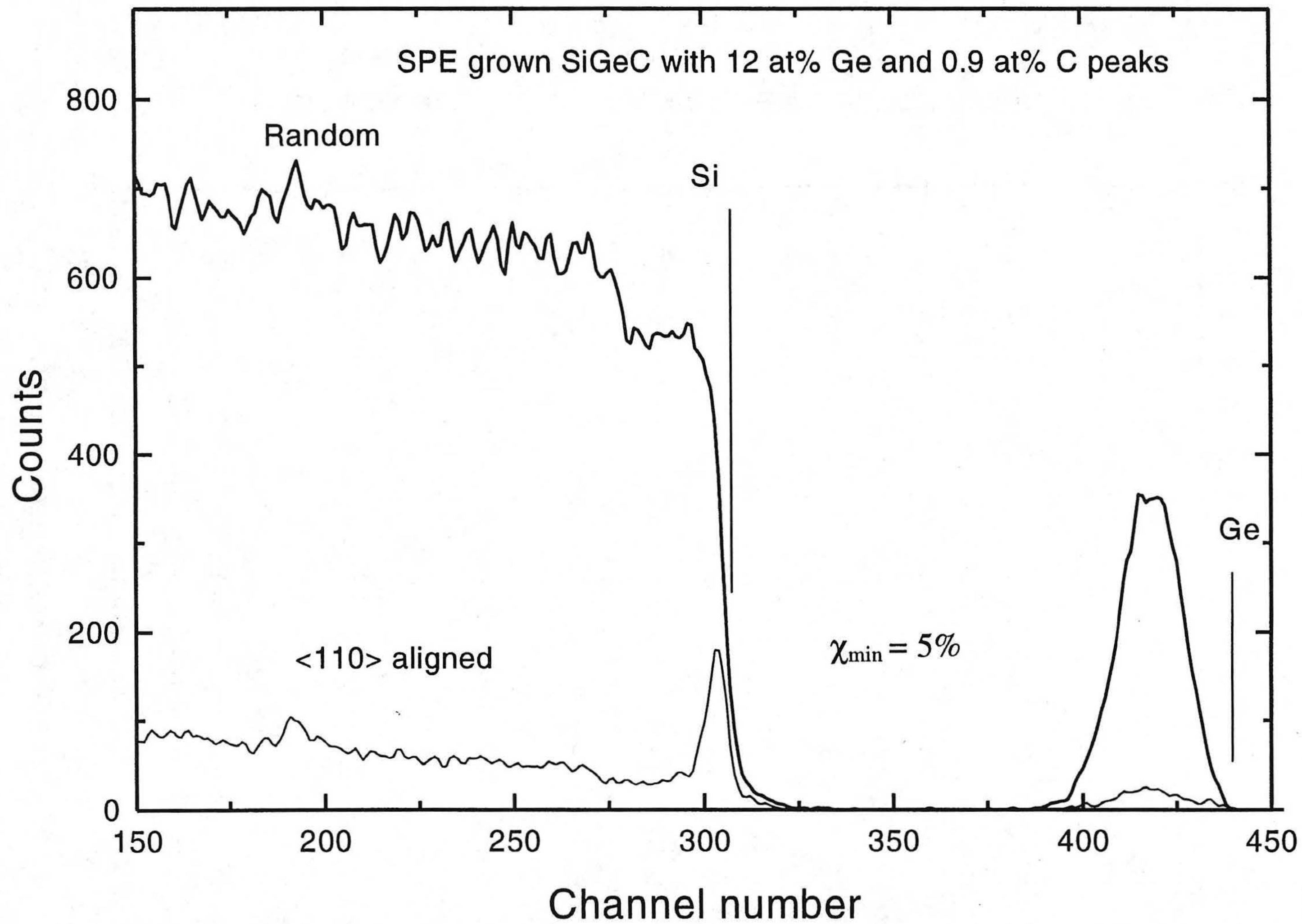

Fig. 32(c). Random and <110> ion channeling spectra of SPE grown SiGeC layer (12 at% Ge and 0.9 at% C peaks).

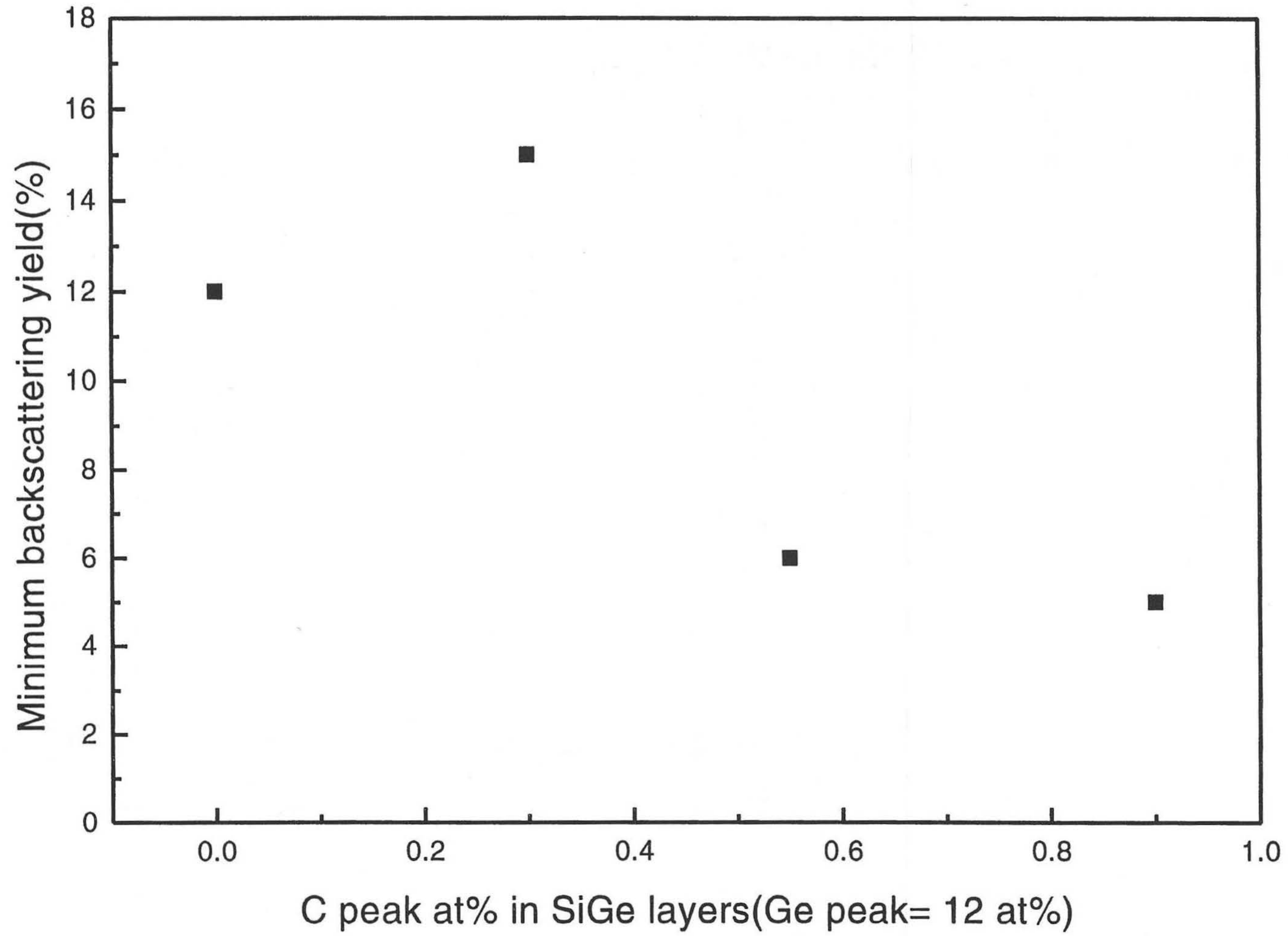

Fig. 33. Plot of χ_{min} vs. C peak concentration in SPE regrown layers with 12 at% Ge peak.

5. Discussion

5.1 EOR dislocation loops

As already discussed in Chapter 2 and Chapter 4, LNT implantation would be expected to considerably reduce the EOR loop density because the density of recoiled Si interstitials is smaller beyond the a/c interface during low temperature implantation. Nevertheless, the reduced amount of dislocations is still not small. The plan view TEM (PTEM) micrograph in fig. 34 shows the density of residual EOR loops after LNT implantation and SPE annealing. Large loops are perfect dislocations while small loops are faulted as indicated in the figure by their characteristic fringe contrast. It is likely that the small faulted loops are Frank loops with a burger's vector of a/3(111), which are "unfaulted" to perfect dislocations of a/2(110) type by reaction with a Shockley partial dislocation of $a/6(11\bar{2})$ type during the thermal annealing process.[25,34] The well-known reaction is expressed as follows:

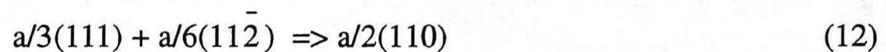

$$a/3(111) + a/6(11\bar{2}) \Rightarrow a/2(110) \qquad (12)$$

This reaction is energetically possible if the stacking fault energy is considered.[25,34] The dislocation density resulting after LNT implantation is still much too large to be used in IC devices. Due to high ion beam current and limited heat-sinking capacity of wafer station, the real wafer temperature may be higher than LNT during implantation. As a result of that, the effective reduction of EOR loop density would be impeded. To maximize the low temperature implantation effect, both optimum control of ion beam flux

and considerate design of wafer station are necessary. According to the literature, EOR loops may be reduced by other methods besides low temperature implantation. [40,41,67] One example is C implantation, so that the C concentration peak is on the EOR region, has been attempted. This method can reduce the EOR loop density by a certain amount although the reduction mechanism is still not clearly understood. It may be, however, possible that Si interstitials are pinned by interstitial C or substitutional C atoms in the same region beyond the a/c interface. Once the interstitials are rendered immobile by the pinning effect, their clustering into lines or planar defects such as EOR loops becomes difficult. In the present work, the C effect on EOR loop density is not clear because the C peak is not located in the EOR region but in the Ge peak region. If as-implanted amorphous layers do not show any extended lattice defects beyond the a/c interface even during RT implantation, it is likely that no EOR loops may come out after SPE annealing. A possible example is a low energy SiF_4 implantation into a Si substrate, which was performed for a study of preamorphization effects on dopant diffusion and ultra-shallow junction formation in a PMOS (p-type metal oxide semiconductor) test structure. [68,69] Low energy implantation at 4 to 6 keV did not lead to EOR defect generation in that study.

5.2 Equilibrium critical thickness and kinetics for misfit defect generation

In order to estimate the SiGe layer thickness before strain relaxation, equilibrium critical thicknesses under which misfit dislocations can not generate or propagate were calculated by modifying classical force balance equations. [70-72] In the classical cases, the

balance equation is shown by equating the dislocation line tension and the shear force working on the dislocation line (perfect dislocation). A schematic diagram in fig. 35 shows the force balance in a heteroepitaxial layer on a substrate. Since the slip system of dislocations in face centered cubic or diamond cubic structure is <110>(111), the dislocation motion must be considered in those orientations. Energetically, the most favorable dislocation in strain relaxation is the 60 degree perfect dislocation which has the largest burger's vector. By assuming the generation of only 60° perfect dislocation as misfit defects, the calculation was performed as follows:

$$\sigma_a = \sigma \cos\theta\cos\phi \tag{13}$$

$$\sigma = 2G\varepsilon(1+\nu)/(1-\nu) \tag{14}$$

$$\text{force on dislocation (VPE)} = \sigma \cos\theta\cos\phi \; b \; (h_c/\cos\phi) \tag{15}$$

$$\text{dislocation line tension} = Gb^2(1-\nu \cos^2\theta) \ln (\alpha h_c/b)/4\pi(1-\nu) \tag{16}$$

where ε is a misfit strain, σ is the compressive biaxial stress, σ_a is an applied stress or a shear stress on dislocation in (111) plane, $\cos\theta\cos\phi$ is a Schmidt factor due to the crystal orientation, G is a shear modulus, ν is about 0.27 as a Poisson's ratio of Si or Ge, α is about 2, a constant related to dislocation core size, h_c is the critical thickness, θ is an angle between the burger's vector and dislocation line and $90-\phi$ is an interplanar angle between the (111) slip plane and the (100) interface plane as shown in fig. 35. When we equate equation (15) and equation (16), h_c is calculated. As shown in the figure, a misfit

dislocation line with a <110> direction is generated in the interface between the SiGe layer and the Si substrate for strain relaxation. However, in actuality, this kind of generation behavior is very rare since the misfit dislocation is usually created from the surface where some higher stress concentration points may exist. Once the misfit dislocation is nucleated, it may grow and migrate to the interface under the biaxial stress conditions as shown in fig. 35. This is one of accepted models for the generation of the threading dislocations which are often observed in various heteroepitaxial layer growth.

In the case of SPE layers, equations (14) and (15) should be reestimated by considering the Gaussian strain profile variation with different heights as follows:

$$\text{misfit strain} = \varepsilon_{misfit} = \delta\, Ge_{peak} \exp(-(Rp_{Ge}-x)^2/2\Delta Rp_{Ge}^{\ 2}) \qquad (17)$$

$$\text{force on dislocation(SPE)} = 2G\,(1+\nu)/(1-\nu)\cos\theta\, b \int_{x_o}^{x_c} \varepsilon_{misfit}dx \qquad (18)$$

$$(h_c = x_c - x_o)$$

where δ (=0.042) is the misfit strain induced by pure Ge in the Si substrate, Rp is 70nm as the projected range for 120 keV Ge^+ ions, ΔRp is about 250Å, the straggle of ions. If the new force on the dislocation from equation (18) is identified with equation (16), the critical thickness for SPE regrown SiGe layers is calculated. The plots in fig. 36 show the comparison of the equilibrium critical thicknesses of SiGe layers with uniform Ge concentration and SiGe layers with Gaussian-distributed Ge (SPE layers), while the

uppermost plot of experimental values of critical thicknesses was obtained from the XTEM micrographs in fig. 25. Using the above equations, equilibrium thickness values of 100 nm, 80 nm, and 65 nm were obtained from the SiGe alloy layers with 5 at%, 7 at%, and 12 at% Ge peak, respectively. SPE grown layers always have larger critical thicknesses due to lower misfit strain on average, and higher Ge compositions always lead to smaller critical thickness due to larger misfit strain. The interesting point in this plot is that even the layer with 5 at% Ge peak may have a critical thickness less than 1500Å. However, it did not show any misfit-induced stacking faults in the experiment. Therefore, as indicated by an arrow in the plot of fig. 36, the layer with 5 at% Ge peak can grow to infinite thickness without any misfit defects generated. For other SiGe layers with 7 or 12 at% Ge peak, the thicknesses before strain relaxation begins were always larger than the calculated equilibrium critical thickness. These considerations may imply that the strain relaxation may not be explained by critical thickness alone, although the equilibrium values of h_c closely approach the experimental values under the present SPE conditions.

Therefore, kinetic limitations on dislocation generation or migration should also be considered because there exists an activation barrier or activation energy to overcome for defect generation. This means that an excess force or energy over the equilibrium condition is necessary for overcoming the barrier. Usually, a thickness larger than the equilibrium critical thickness can be obtained in experimental heteroepitaxy due to this barrier. According to previous work, strain relaxation depends on the epitaxial material and growth conditions. [56,73] Lattice mismatch, elastic constants, crystal orientation and

symmetry, growth temperature and growth rate are the experimental parameters which affect the nucleation or migration of misfit dislocations. The activation energy for migration of 60 degree a/2<110> dislocations is about 2.2eV for Si and 1.6eV for Ge while only 1.0eV for InAs and GaAs for (100) growth orientations. [56,73] These numbers signify that the equilibrium critical thickness is more useful in predicting strain relaxation in GaAs or less rigid compound semiconductors than Si or SiGe alloys having higher elastic constants. It is also clear that higher a growth temperature leads to an equilibrium thickness more readily with assistance of thermal energy. Dodson and Tsao developed a more realistic model for explaining the effects of experimental growth conditions on misfit dislocation nucleation and propagation. [56,73]

5.3 Misfit-induced stacking fault generation and growth kinetics of SPE layer

Typical activation energies for migration of partial dislocations on (110) or (111) planes were recently reported. [56] According to these reports, the activation energy of 90 degree partial dislocation with a burger's vector a/6(112) in (111) oriented SiGe layer with uniform 24 at% Ge is about 1.6eV which is smaller than the activation energy value for migration of 60 degree a/2(110) dislocations in (100) oriented SiGe/Si system(~2.2eV) of which the heteroepitaxial film is under compressive stress. [56] This signifies that if the a/c interface migrating in the direction of <100> has microscopic (111) facets, strain relaxation can be dominated by 90 degree partial dislocations although the burger's vector of the 90 degree partial dislocation, when projected in the (100) interface plane and strain-relieving direction (contrary direction of compressive stress arrows), is only 2/3 of that of

a 60 degree perfect dislocation in terms of effective length for strain relieving. This is because the partial dislocation has a lower activation energy barrier. This may be considered a reasonable explanation about the generation of misfit-induced stacking faults as shown in many figures so far (fig. 25, fig. 30). A high resolution micrograph in fig. 37 shows the a/c interface of an LNT-implanted SiGe layer. Macroscopically, the a/c interface should be flat but microscopically, it has many (111) facets. If a biaxial force acting on the layer is large enough for 90 degree partial dislocations to overcome the activation barrier during SPE regrowth, it is likely that the 90 degree partial dislocations have a chance to nucleate near the most strained region by using (111) planes in the a/c interface. Another factor making it easier to overcome the activation barrier may be the stress concentration effect of the faceted a/c interface. The smaller activation barrier and stress concentration effect may also explain why the experimental critical thickness closely approaches the equilibrium critical thickness (as shown in fig. 36). Unlike SPE growth, MBE and other VPE growth have very smooth, (100) oriented surfaces which usually show 60 degree perfect dislocations in their strain relaxation process. [56,74,75] This fact indirectly supports the generation of stacking faults as the dominant strain relaxation mechanism in SPE regrowth.

Once the partial dislocations with stacking faults are generated, the regrowth rate is retarded because the growth mode is changed microscopically from a (100) mode to a (111) faceted mode, which has the slowest rate of growth as mentioned in Chapter 2. Then, the change of regrowth kinetics shown in the XTEM micrographs of fig. 29 can be

reasonably explained. Moreover, stacking mistakes are repeated due to the nature of (111) growth and the resultant SPE layer would have a high density of stacking faults.[44-46]

5.4 Critical average strain for generating misfit-induced defects

Another fact to consider is the threshold Ge peak concentration for misfit-induced defects as observed in section 4.4. Since the 5 at% peak SiGe layer does not show any misfit-induced defects while the 7 at% peak layer does show a high density of stacking faults, it can be presumed that a threshold Ge peak concentration exists at about 6 at%. In fig. 38, residual strain curves are plotted by assuming a Gaussian distribution of Ge in the SiGe layers. In this simulation, ΔRp and Rp were 250Å and 700Å, respectively. The peak misfit strain for 6 at% Ge peak is about 0.25%. In the figure, it is also indicated by arrows that if residual strain (misfit strain) is over 0.25% in the peak, strain relaxation may occur. Considering equation (17) again, we can define an average critical strain or strain energy for generating strain relaxation as follows:

$$\varepsilon_{crit.ave} = \int_0^H \varepsilon_{misfit} dh / H \tag{19}$$

where H is an effective total thickness of SPE layer which can be fixed at about 1500Å, and the force can be obtained by multiplying H and the elastic modulus to the average critical strain. The average critical strain is found to be about 0.11% using equation (19) and by considering the threshold Ge peak concentration of 6 at% obtained in the present experimental conditions. This average threshold or critical misfit strain may increase if a

lower annealing temperature is employed for SPE. Rather than a critical peak misfit strain, the average critical misfit strain, $\varepsilon_{crit.ave}$ may provide a more general parameter to define a standard strain condition for strain relaxation in SPE layers, even though 0.11% of $\varepsilon_{crit.ave}$ is applied in the present annealing condition only. In other words, even if thicker SPE SiGe layers than the present layers are synthesized by using higher Ge ion energy and doses, the same standard strain condition can be applied for strain relaxation as long as same annealing conditions are given. Since the average misfit strain obtained from the 5 at% peak layer was about 0.14% as shown by the XRD results (fig. 28) of section 4.4 and since the real Ge distribution for the layer is not an exact Gaussian, the average critical strain value, 0.11% obtained from the 6 at% Ge peak layer is somewhat tolerable. It should be also noted that the measured value, 0.14% in 5 at% peak layer is not an average misfit strain value but the maximum local misfit strain value. Therefore, we can conclude that an average misfit strain for strain relaxation is about 0.11% under the present SPE regrowth conditions.

5.5 Strain compensation by C sequential implantation

The lattice parameters of Si and Ge single crystals are 5.43Å(a_{Si}) and 5.66Å(a_{Ge}), respectively. Those of a SiC unit cell and a diamond unit cell are 4.36Å (a_{Si-C}) and 3.45 Å(a_C).[76] Therefore, the formed SiGe layer on the Si substrate should have a compressive strain condition which may nucleate misfit dislocations if the layer thickness is much greater than the equilibrium critical thickness. However, the nucleation of misfit dislocations can be minimized if the misfit strain is compensated by any means. Since C

and C compounds have smaller volumes than the Si and Ge unit cells, the SiGe layer with an optimum amount of C atoms may experience this compensation effect if the C atoms are sitting in substitutional sites of the Si lattice. [77-79] A schematic diagram in fig. 39 illustrates the compensation effect. The atomic radii of C and Ge are 0.77Å and 1.224Å, respectively, the atomic radius of Si is 1.176Å. [80] While the atomic sizes of Si and Ge are not much different from each other, there is a big difference in atomic size between C and Si, suggesting that a very small amount of C atoms may be sufficient to compensate the strain induced by a large amount of Ge atoms. No dislocations may be needed as long as C atoms compensate the volume change due to the presence of Ge atoms in the Si lattice. Another aspect of this strain compensation may be the distribution of C atoms during SPE annealing. Fortunately, previous work has seen only very small changes of Ge and C distribution at the present annealing temperature, 800°C. [34,81,82] Raman spectroscopy results in fig. 40 also support this strain compensation effect showing a vibration peak of Si-C bond at a wave number of $608cm^{-1}$. Laser probing was performed on a SPE grown SiGeC specimen with 12 at% Ge peak and 0.55 at% C peak. The vibration peak from Si-C bond has been reported previously,[66] but a typically-seen Ge-Ge lattice phonon peak at about $300cm^{-1}$ was not observed here. This work does show Si-Si and Si-Ge peaks, however, indicating that the Ge-Ge bond or Ge segregation is too rare to be clearly shown in the present spectra. According to other researches on Raman spectroscopy of SiGe layers, Ge-Ge lattice phonon peak is observable in a SiGe layer with more than 20 at% Ge. [53,54,83] Raman spectra of the SPE SiGeC layer does not show any SiC (silicon carbide) peaks, C-C peaks or interstitial C peaks (920 cm^{-1}). The strain

compensation was confirmed by XRD results in fig. 41. While the SiGe layer with 5 at% Ge peak clearly shows the separation of the (400) peak by 360 arcsec in fig. 28 of Chapter 4, the layer with 12 at% Ge peak and 0.9 at% C peak does not show any peak separation of more than 100 arcsec in $\Delta\theta$. If this XRD result is considered along with the corresponding XTEM micrograph in fig. 32, the lack of peak separation may be explained on the basis of both strain compensation and a small amount of strain relaxation observed near the specimen surface.

5.6 Optimum Ge/C ratio for strain compensation

From the results shown in fig. 31 and fig. 32, we already know that the best crystallinity is obtained from a SiGeC layer with 0.9 at% C peak in the present SiGeC specimen series. However, it is also important to determine a theoretical Ge/C peak ratio for optimum strain compensation. Although previous research has used a linear model of lattice parameter variation in mixing Si, Ge and diamond unit cells to calculate the Ge/C ratio for the strain-free state in MBE-grown SiGe layers with uniform Ge composition, a similar model calculation is performed here to obtain an optimum Ge/C ratio by assuming a random array of Si, Si-Ge and Si-C unit cells in a SiGeC alloy with uniform Ge and C distributions. Lattice parameters of crystals are taken as follows.[76,80,84] :

$$a_{Si}=5.43\text{Å},\ a_{Ge}=5.66\text{Å},\ a_{Si\text{-}C}=4.36\text{Å and } a_{Si\text{-}Ge}=5.53\text{Å},^{84} \qquad (20)$$

where $a_{Si\text{-}Ge}$ means lattice parameter of SiGe with 50 at% Ge. Since the lattice parameter of a Si unit cell, a_{Si} must equal to that of SiGeC alloy for absolute strain compensation,

$$a_{Si}= a_{SiGeC}= 5.43\text{Å} \tag{21}$$

If the fractional concentration of those unit cells is considered,

$$a_{SiGeC}= (1\text{-}x\text{-}y)\ a_{Si} + (x)\ a_{Si\text{-}Ge} + (y)\ a_{Si\text{-}C}\ (y) \tag{22}$$

where 1-x-y, x and y are the fractional concentrations of each unit cell. The ratio, x/y is worked out as follows: x/y= 10.7. The Ge/C concentration ratio will be approximately the same number, 10.7. With a Ge concentration of 12 at% in the layers, 1.1 at% C may most effectively compensate the misfit strain in the case of a layer with uniformly distributed Ge and C.

However, the spatial distributions of the Ge and C are not uniform but Gaussian-like in the present SPE grown layers. Moreover, because the C straggle is broader than the Ge straggle by about 50Å as estimated by TRIM simulation(see Appendix), it would be very difficult to get the ratio of 10.7 throughout the entire depth. Gaussian profiles of Ge and C are shown in fig. 42 and depth profiles of residual strain in layers with different Ge/C peak ratios are simulated in fig. 43 using a strain compensation equation as follows:

$$\text{strain}(\%) = \delta\, Ge_{peak} \exp(-(Rp_{Ge}-x)^2/2\Delta Rp_{Ge}^{\ 2})$$

$$- 10.7\delta\, C_{peak} \exp(-(Rp_{C}-x)^2/2\Delta Rp_{C}^{\ 2}) \qquad (23)$$

where δ(=0.042) is the misfit strain induced by pure Ge in the Si substrate, Rp is 70nm as the projected range for both Ge and C, the ΔRp is the straggle of ions, C_{peak} is the peak concentration of C in at%, Ge_{peak}(=12 at%) is the peak concentration of Ge, and x is the depth from the surface. Note the number 10.7 indicating the compensating effect of C in the second term of the equation. With a C peak concentration of 1.1 at%, tensile stresses are introduced by excess C atoms in the whole layer except for the peak region where the compressive stresses induced by Ge atoms have been compensated(see plot 5 of fig. 43). The layer with the ratio of 13.3(=12/0.9) in the plot 4 of fig. 43 shows both a compressive strain area and tensile strain area. If both of the areas are the same, an optimum strain compensation is obtained because the average strain is zero. Therefore, based on this simple modeling and above experimental results, we conclude that an optimum window of Ge/C peak ratio exists between 11 and 22, which corresponds to 1.1 at% and 0.55 at% in C peak concentration respectively.

The critical average misfit strain($\varepsilon_{crit.ave}$) discussed earlier in section 5.4 can be re-applied to strain-compensated layers. The critical average strain and the peak strain in the Gaussian strain profile were about 0.11% and 0.25%, respectively, as obtained from the

SiGe layer with 6 at% Ge peak in a simulation. This standard is also effective for strain-compensated SiGeC layers. The strain remaining after compensation should be less than 0.11% on average for generating no misfit dislocations in the layers if the standard is valid. A SiGeC layer with 12 at% Ge and 0.55 at% C peaks (which corresponds to plot 3 of fig. 43) begins to show strain compensation with a reduced density of stacking faults as experimentally shown by both XTEM and ion channeling. Plot 3 of fig. 43 probably shows the critical condition for defect generation or strain compensation because the average strain and peak strain obtained from plot 3 were 0.11% and 0.25% respectively. In other words, a threshold C peak concentration to realize the strain compensation effect is equal to 0.55 at% or slightly more than 0.55 at%.

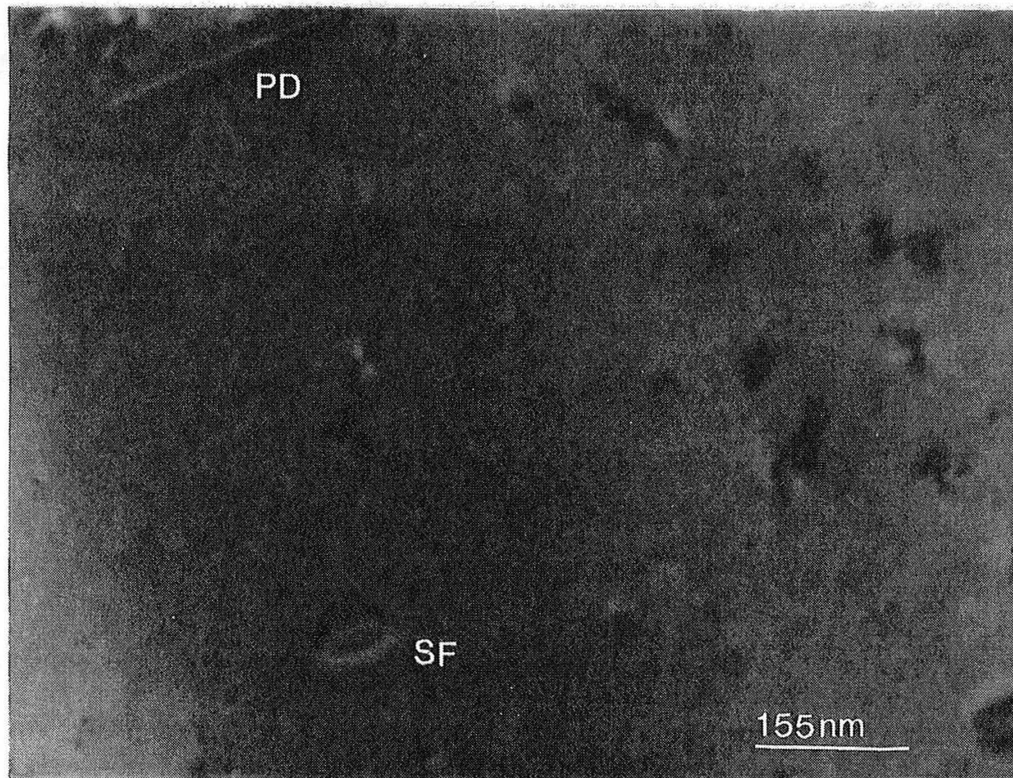

Fig. 34. PTEM micrograph of the SiGe layer with 5 at% Ge peak shows the EOR dislocation loops remaining after LNT-implantation and SPE annealing. Stacking fault loop and perfect dislocation loop are indicated.

(Perfect dislocation loop = PD, Stacking fault loop = SF).

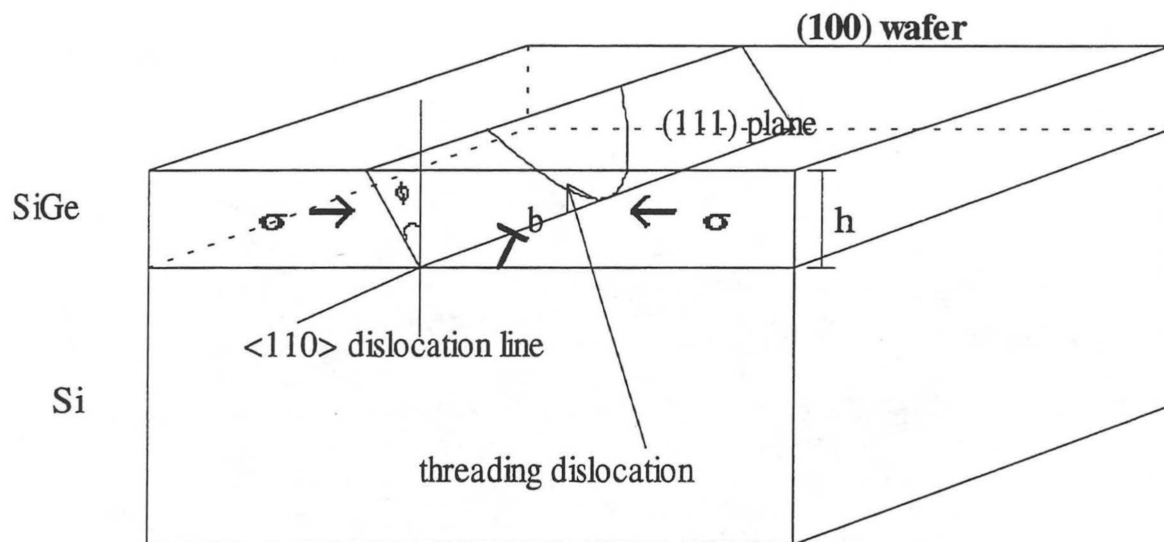

Fig. 35. Dislocation motion in the interface of heteroepitaxial system. Line tension of dislocation will be balanced with the shearing force acting on the misfit dislocation in (111) slip plane. Threading dislocation(misfit dislocation) tends to start from surface.

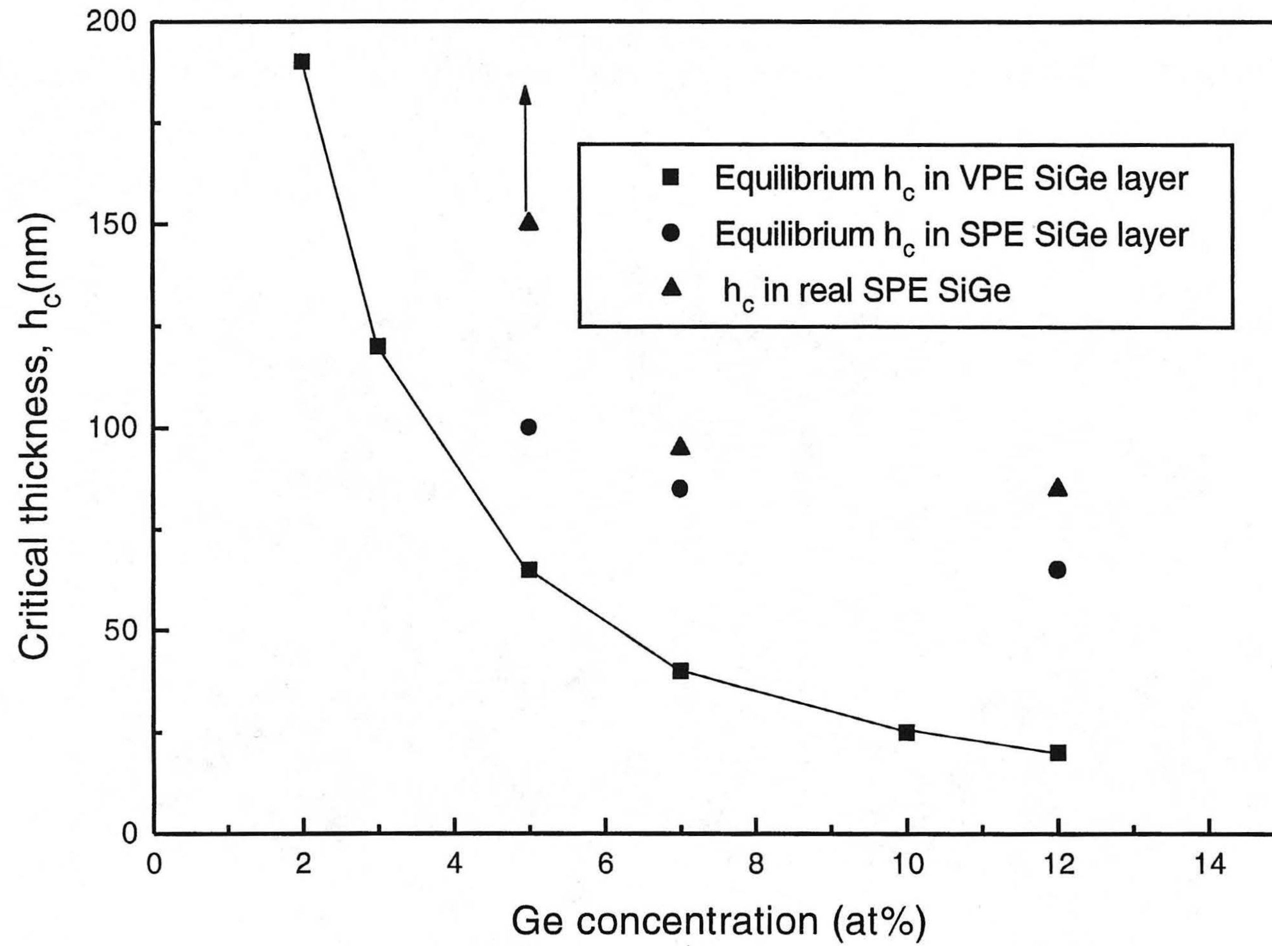

Fig. 36. Equilibrium critical thickness vs. Ge concentration in SiGe layer with uniform or Gaussian distributions of Ge. Peak concentrations are used to plot the critical thicknesses for SPE SiGe layers. Experimental values were also measured from XTEM micrographs and plotted. The critical thickness was infinite in the case of the 5 at% Ge peak layer.

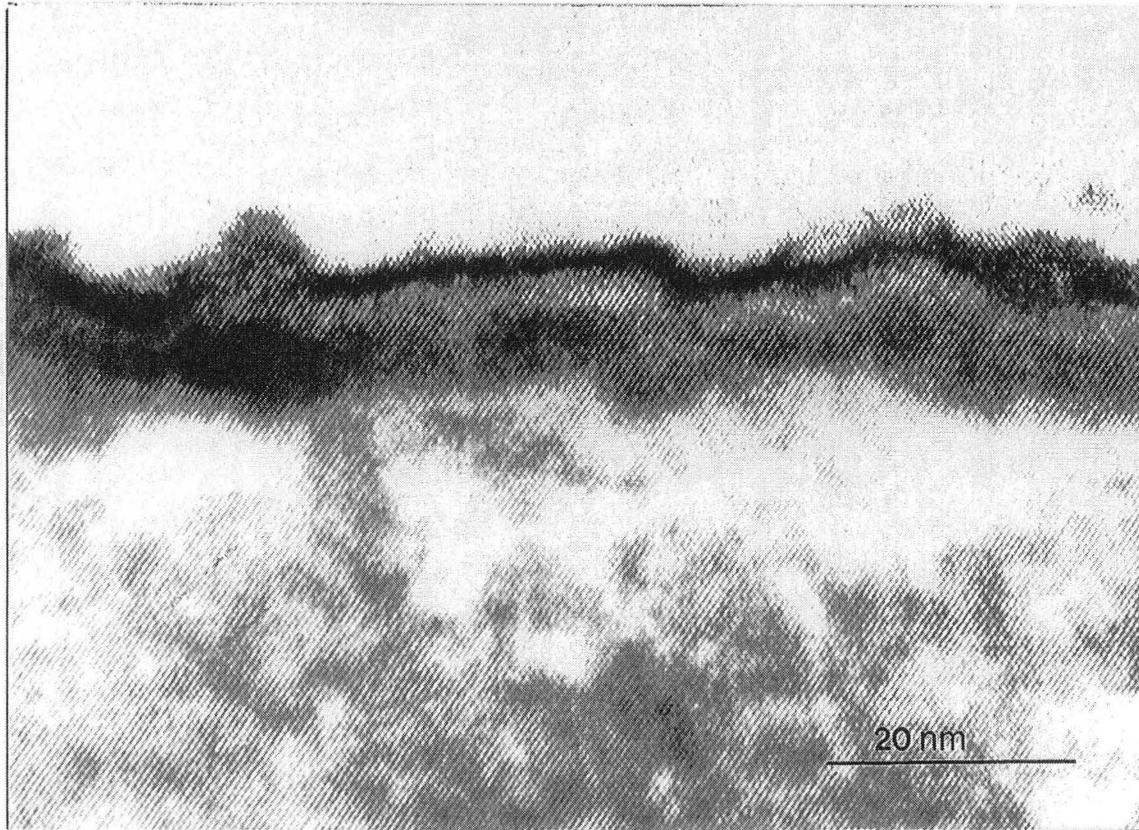

Fig. 37. High resolution XTEM micrograph showing the a/c interface of LNT-implanted SiGe layers. The a/c interface is not microscopically flat in SPE growth and may have (111) planes as well as (100) planes in a certain density.

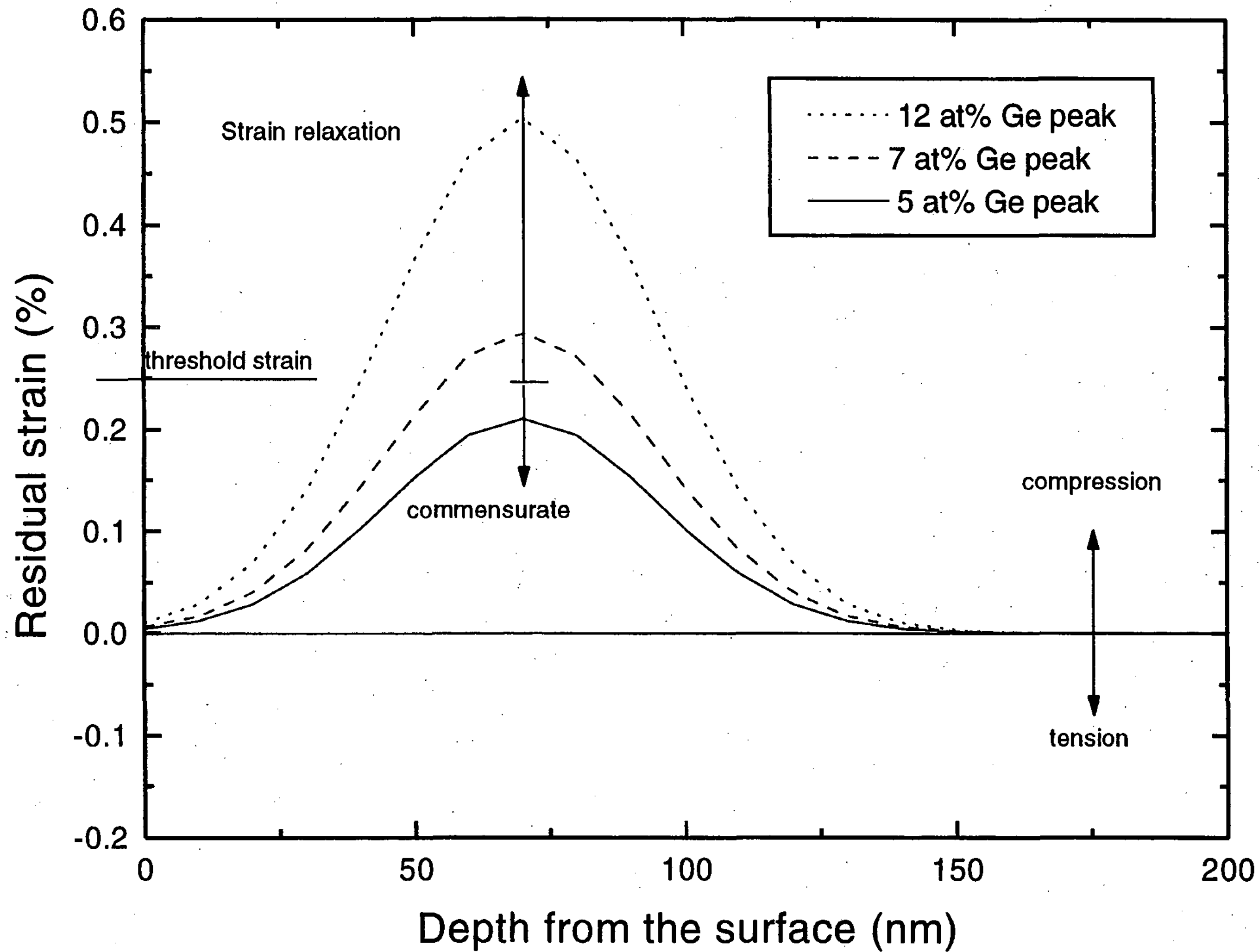

Fig. 38. Simulated depth profiles of residual strain in SiGe layers with various Ge peaks. In experiment, strain relaxation occurred in the SPE layers with 12 and 7 at% Ge peak.

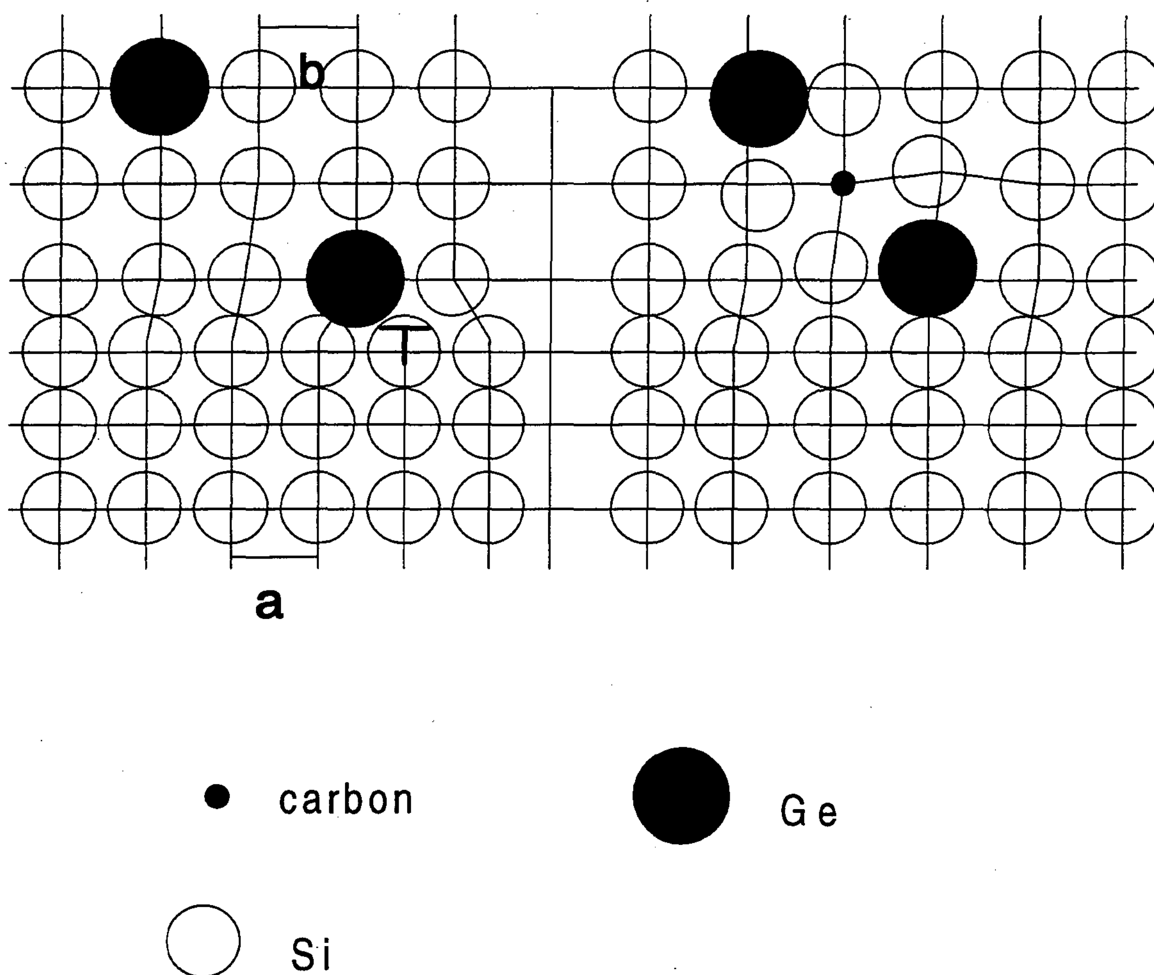

Fig.39 Schematic picture illustrates strain compensation effects of C atoms on strain relaxation induced by Ge atoms which are larger than Si and C atoms.

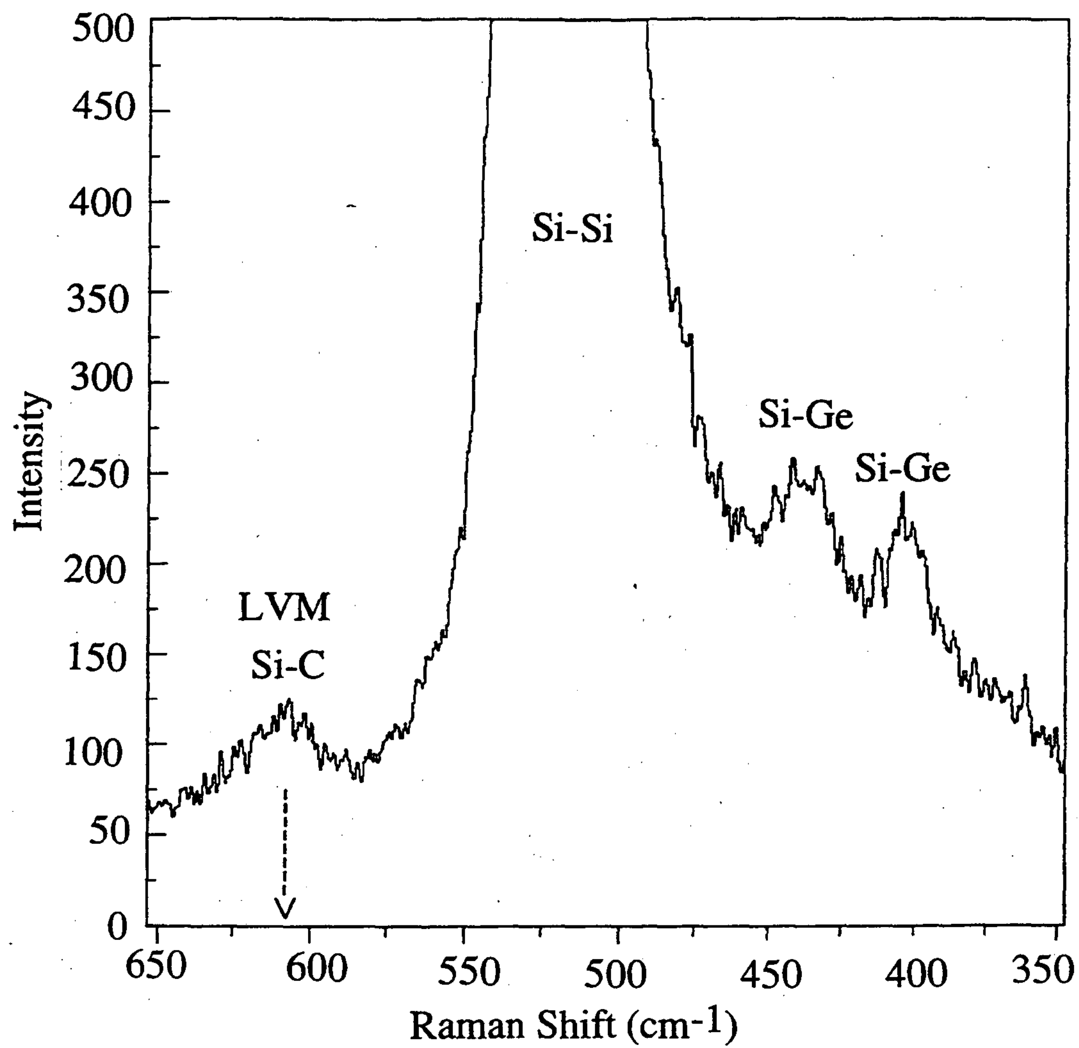

Fig.40 Raman spectra show only Si-Si, Si-Ge lattice phonon peaks and Si-C lattice vibrational mode in a SiGeC layer with 12 at% Ge peak and 0.55 at% peak.

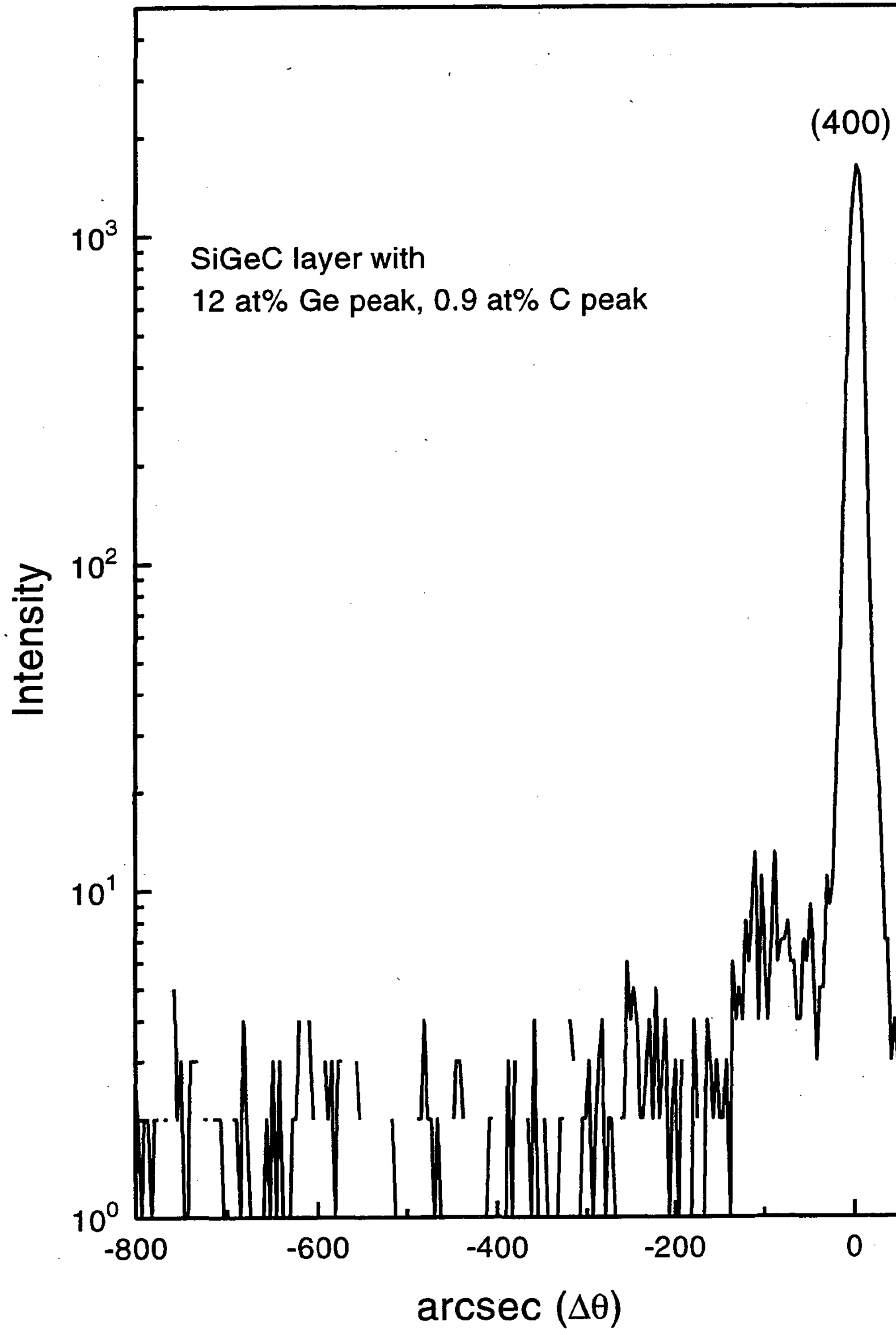

Fig.41 X-ray diffraction results obtained from SPE grown SiGeC layer with 12 at% Ge peak and 0.9 at% C peak. Rocking curve is plotted in intensity vs. arcsec(Δθ).

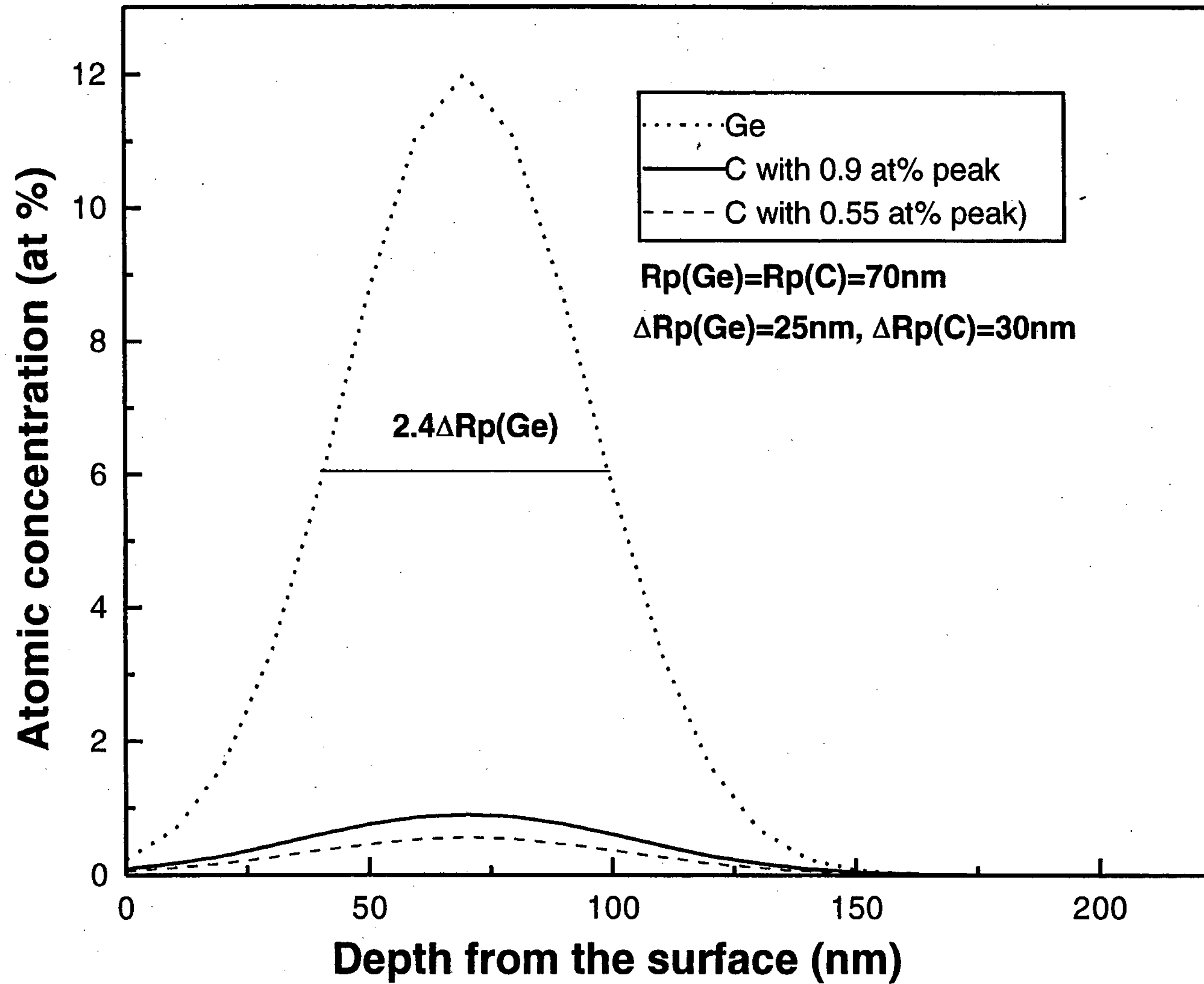

Fig. 42. Gaussian profiles of Ge and C in SiGeC layers. ΔR_p was obtained by using TRIM simulation.

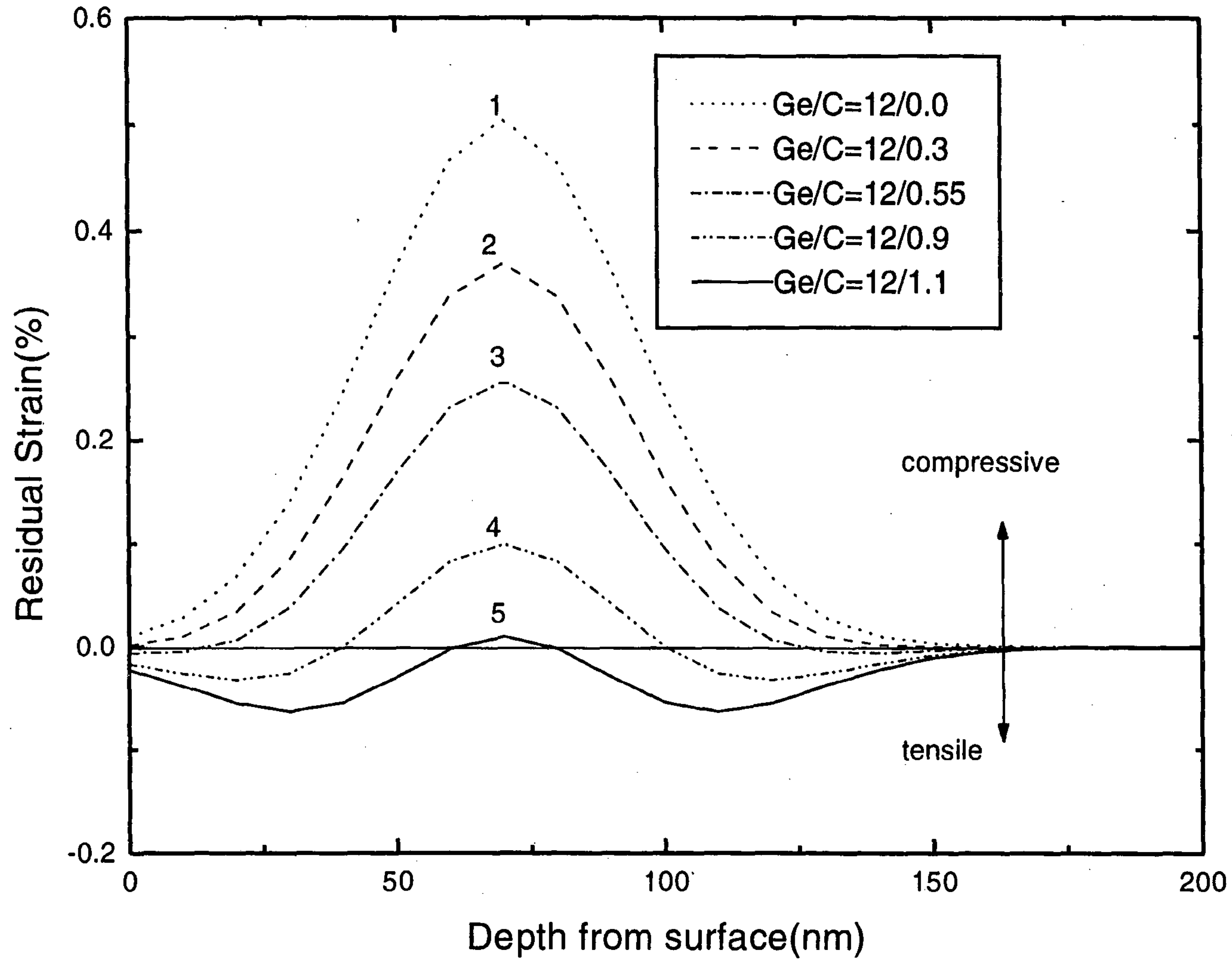

Fig. 43. Depth profiles of residual strain in various SiGeC layers

6. Conclusions

In the present work, a systematic study of the processing procedures required for minimizing structural defects generated during the ion beam synthesis (IBS) of SiGe alloy layers has been performed. The defects are successfully minimized by controlling the relevant processing parameters. To make about 200 nm thick SiGe alloy layers, high doses of Ge ions with the beam energy of 120 keV are implanted in <100> oriented Si wafers. Various Ge peak concentrations have been obtained in the alloy layers from following doses, $2x10^{16}cm^{-2}$, $3x10^{16}cm^{-2}$, and $5x10^{16}cm^{-2}$. After implantation, SPE annealing of amorphized layers has been employed in a nitrogen ambient at 800°C for 1 hour. During the annealing, Ge atoms very slightly redistribute. Two kinds of extended defects have been observed in the layers synthesized with doses over $3x10^{16}cm^{-2}$ at room temperature: end-of-range (EOR) dislocation loops and strain-induced stacking faults. The following conclusions are reached by the present study.

1. Liquid nitrogen temperature (LNT) implantation can considerably reduce the density of end-of-range (EOR) defects while room temperature (RT) implantation always results in the formation of a high density of those defects.

2. Decreasing the implantation dose to obtain 5 at% peak Ge concentration prevents strain relaxation, while those SPE layers with more than 7 at% Ge peak show high densities of misfit-induced stacking faults. Therefore, 6 at% Ge may be a threshold peak concentration, and the associated critical average misfit strain (0.11%) is determined from

Gaussian strain profiles (converted from Ge profiles) as a standard or general condition for strain relaxation.

3. When C sequential implantation is employed following high dose ($5x10^{16}/cm^2$) Ge implantation yielding a 12 at% Ge peak concentration in the layer, stacking faults are effectively reduced in density. When the nominal peak concentration of implanted C is over 0.55 at%, misfit dislocation generation in the epitaxial layer is considerably suppressed. This effect is explained as a result of strain compensation by C atoms in the SiGe alloy lattice. A SiGe alloy layer with 0.9 at% C peak concentration under a 12 at% Ge peak shows the most improved crystallinity compared to layers with smaller C peak concentrations. The experimental results, combined with a simple model calculation, indicate that the optimum Ge/C ratio for strain compensation is between 11 and 22.

4. Equilibrium critical thicknesses for SPE grown SiGe layers are calculated to be nearly close to experimentally obtained values. However, the formation mechanism of misfit-induced stacking faults can not be understood by equilibrium theory, but requires dislocation migration or nucleation kinetics. Stacking faults are dominant in the strain-relaxed SPE layers because 90 degree partial dislocations have a lower activation barrier for nucleation than 60 degree perfect dislocations as long as (111) habit planes in the a/c interface are involved in the SPE growth process.

5. The interface between the amorphous and regrown phases (a/c interface) shows a dramatic morphology change during its migration to the surface. The initial <100> planar interface decomposes into a <111> faceted interface, changing the growth kinetics. These phenomena are associated with strain relaxation by stacking fault formation on (111) planes in the a/c interface.

References

1. Heiner Ryssel and Ingolf Ruge, Ion Implantation, John Wiley and Sons Inc., 1986
2. James, F. Gibbons, Proceedings of the IEEE, **56** (3), 295 (1968)
3. James, F. Gibbons, Proceedings of the IEEE, **60** (9), 1062 (1972)
4. J. A. Davies, MRS Bulletin, June, 26 (1992)
5. James, M. Mayer, and John A. Davies, Ion Implantation in Semiconductors, Academic Press, 1970
6. G. K. Celler and Alice White, MRS Bulletin, June, 40 (1992)
7. King-Ning Tu, James W. Mayer, Leonard C. Feldman, Electronic Thin Film Science for Electrical Engineers and Materials Scientists, Macmillan Publishing Company, 1992, p. 274
8. C. Jaussaud, T. Margail, J. Stoemenos and M. Bruel, Mat. Res. Soc. Symp. **107**, 17 (1988)
9. A.H. Van Ommen, Mat. Res. Soc. Symp. **107**, 43 (1988)
10. C. Jaussaud, J. Stoemenos, J. Margail, A. M. Papon and M. Bruel, Vacuum, **42**(5/6), 341(1991).
11. A.H. Van Ommen,"New Trends in SIMOX", Nuclear Instruments and Methods in Physics Research, **B39**, 194 (1989)
12. K. G. Stephens, K. G. Reeson, B. J. Sealy, R. M. Gwilliam and P. L. F. Hemment, Nuclear Instruments and Methods in Physics Research, **B50**, 368 (1990)
13. C. W. T. Bullie-Lieuwma, A. H. Van Ommen, D. E. W. Vandenhoudt, J. J. M.

Ottenheim, and A. F. de Jong, J. Appl. Phys. 70 (6), 3093 (1991)

14. Alice E. White, K. T. Short, R. C. Dynes, J. M. Gibson, and R. Hull, Mater. Res. Soc. Symp. Proc. **100**, 3, (1988)
15. K. M. Yu, B. Katz, I. C. Wu and I. G. Brown, Nuclear Instruments and Methods in Physics Research, **B58**, 27 (1991)
16. D.C. Paine, D.J. Howard, N.G. Stoffel, J. Electronic Materials, **20**(10), 735 (1991)
17. D.C. Paine, D.J. Howard,J.A. Horton, J. Mater. Res., **5**, 1023(1990)
18. K. M. Yu, I. G. Brown and Seongil Im, Mat. Res. Soc. Symp. Proc., **235**, 293(1992)
19. G.L.Patton, S.S. Iyer, S.L. Delage, S.Tiwari, J.M.C. Stork, IEEE Electronic Device Lett., **9**(4), 165 (1988)
20. G.L. Patton, J.H. Comfort, B.S. Meyerson, E.F. Crabbe, G.J. Scilla, E. De Fresart, J. C. Stork, J.Y. -C. Sun, IEEE Electronic Device Lett.,**11**(4), 171 (1990)
21. Akira Fukami, Ken-ichi Shoji, Takahiro Nagano, Cary Y. Yang, Appl. Phys. Lett. **5**(22), 2345 (1990)
22. Akira Fukami, Ken-ichi Shoji, Takahiro Nagano, Cary Y. Yang, Microelectronic Engineering **15,** 15(1991)
23. Malcom I. Heggie, Bob Jones and Andrey Umerski, Mat. Res. Soc. Symp. Proc. **193** 277 (1990)
24. B. Henderson, Defects in Crystalline in Solids, Edward Arnold Ltd., 1972, p. 117-134

25. D. Hull, Introduction to dislocations, 2nd Edition, Pergamon Press, Oxford (1975)

26. J. Lindhard, M. Scharff, and H. E. Schiotte, Kgl. Danske Videnskab Selskab. Mat. Phys. Medd., 33 (14), (1963)

27. Y. C. Shih, Ph. D Thesis, The Formation of Amorphous Silicon by Light Ion Damage, December 1985

28. J. S. Williams, K. T. Short, R.G. Elliman, M. C. Ridgeway, and R. Goldberg, Nuclear Instruments and Methods in Physics Research **B48**, 431 (1990)

29. J. S. Williams, M. C. Ridgeway, R. G. Elliman, J. A. Davies, S. T. Johnson and G. R. Palmer, Nuclear Instruments and Methods in Physics Research **B55**, 602 (1991)

30. J. P. Biersack and J. F. Ziegler, TRIM (simulation software), Version 90.05, 1989

31. S. Prussin, David I. Margolese, and Richard N. Tauber, J. Appl. Phys. **57** (2), 180 (1985)

32. David K. Brice, Ion implantation Range and Energy Deposition Distribution, Plenum

Press, New York, 1975, Vol. 1.

33. K. S. Jones, S. Prussin, and E. R. Weber, Appl. Phys. **A 45**, 1 (1988)

34. Properties of Silicon, EMIS Data reviews series No.4, published by INSPEC, The Institution of Electrical Engineers, New York, (1988) p. 285-

35. S. Prussin, K.S. Jones, J. Electrochem. Soc., **137**, (6), 1912 (1990)

36. K.S. Jones, D. Venables, J. Appl. Phys. **69**(5), 2931 (1991)

37. D. Venables, K. S. Jones, Nuclear Instruments and Methods in Physics Research **B59/60**, 1019 (1991)

38. E. Ganin, A. Marwick, Mat. Res. Soc. Symp. Proc. **147**, 13 (1989)

39. A.M. Mazzone, Phys. Stat. Sol., (a) **95**, 149 (1986)

40. R. J. Schreutelkamp, J. S. Custer, J. R. Liefting, W. X. Lu, and F. W. Saris, Materials Science Reports **6**, 275 (1991)

41. J. R. Liefting, J. S. Custer, F. W. Saris, Mat. Res. Soc. Symp. Proc. **187** in press.

42. R. W. Olesinski and G. J. Abbaschian, Bull. Alloy Phase Diagrams, 5 (2), Apr. 1984

43. T. W. Sigmon, M. A. Parker, Nuclear Instruments and Methods in Physics Research **B37/38**, 280 (1989)

44. R. Drosd and J. Washburn, J. Appl. Phys., **53**(1), 397 (1982)

45. R. Drosd and J. Washburn, J. Appl. Phys., **51**(8), 4106 (1980)

46. J. Narayan, J. Appl. Phys., 53 (12), 8607 (1982)

47. <u>Ion Implantation and Beam Processing</u>, editted by J. S. Williams and J. M. Poate, Academic Press, Australia, (1984) p. 13

48. Csepregi, L., Kennedy, E. F., Gallagher, T. J., Mayer, J. W., and Sigmon, T. W., J. Appl. Phys., **49**, 3906 (1977)

49. J. S. Williams, R. G. Elliman, Appl. Phys. Lett. **37**(9), 829 (1980)

50. S. U. Campisano, E. Rimini, P. Baeri, and G. Foti, Appl. Phys. Lett. **37**(2), 170 (1980)

51. S. U. Campisano, G. Foti, P. Baeri, M. G. Grimaldi, and E. Rimini, Appl. Phys. Lett. **37**(8), 719 (1980)

52. <u>Epitaxial Growth</u>, editted by J. W. Matthews, Academic Press, 1975

53. S. C. Jain and W. Hayes, Semicon. Sci. Technol., **6**, 547 (1991)

54. Strained-Layer Superlattices: Materials Science and Technology, series in Semiconductors and Semimetals, editted by Thomas P. Pearsall, 33, 3 and 223 (1991)

55. D. J. Howard, D. C. Paine, N. G. Stoffel, Mat. Res. Soc. Symp. Proc. **187**, 279 (1990)

56. R. Hull, J. C. Bean, F. Ross, D. Bahnck and L. J. Peticolas, Mat. Res. Soc. Symp. Proc. **239**, 379 (1992)

57. Ian G. Brown, Nuclear Instruments and Methods in Physics Research **B37/38**, 68 (1989)

58. I. G. Brown, M. R. Dickinson, J. E. Galvin, X. Godechot and R. A. MacGill, Nuclear Instruments and Methods in Physics Research **B55**, 506 (1991)

59. Ian Brown and Jack Washburn, Nuclear Instruments and Methods in Physics Research **B21**, 201 (1987)

60. Wei-Can Chu, J. W. Mayer, Marc-A. Nicholet, Backscattering Spectrometry, Academic Press, 1978

61. Albert Romano, Jan Vanhellemont and Hugo Bender, Mat. Res. Soc. Symp. Proc. **199**, 167 (1990)

62. Gareth Thomas, Michael J. Goringe, Transmission Electron Microscopy of Materials, John Wiley and Sons Inc., 1979

63. Charles Kittel, Introduction to Solid State Physics, p 306, 6th edition, John Wiley and Sons, Inc. 1986

64. M. F. Ashby and L. M. Brown, Phil Mag., **8**, 1083 and 1649 (1963)

65. S. N. Hsu, L. J. Chen, S. S. Lau, Nuclear Instruments and Methods in Physics

Research **B59/60**, 1037 (1991)

66. K. Eberl, S. S. Iyer, S. Zollner, J.C. Tsang and F. K. LeGoues, Appl. Phys. Lett., **60**(24), 3033(1992)

67. M. Tamura, T. Ando, and K. Ohyu, Nuclear Instruments and Methods in Physics Research **B59/60**, 572 (1991)

68. E. C. Jones, Seongil Im and N. W. Cheung, "Ultra-Shallow P+/N Junctions formed by SiF4 Preamorphization and BF3 implantation using Plasma Immersion Ion Implantation," Mater. Res. Soc. Symp. Proc. **279**, 255, (1992)

69. E. C. Jones, Seongil Im and N. W. Cheung, "Characterization of Ultra-Shallow P^+/N Diodes Fabricated using Plasma Immersion Ion Implantation", Proceedings of the Ninth International Conference on Ion Implantation Technology (Gainesville, FL), 373, (1992)

70. J. W. Matthews, J. Vac. Sci. Technol., **12** (1), 126, (1975)

71. William D. Nix, Met. Trans. A., **20A**, 2217 (1989)

72. L. B. Freund, Journal of Applied Mechanics, **54**, 553 (1987)

73. Brian W. Dodson and Jeffrey Y. Tsao, Appl. Phys. Lett. **51** (17), 26 (1987)

74. K. H. Jung, Y. M. Kim, and D. L. Kwong, Appl. Phys. Lett. **56** (18), 1775 (1990)

75. E. Kasper and H. Jorke, J. Vac. Sci. Technol., **A 10**(4), 1927 (1992

76. J. M. Baranowski, J. Phys. C: Solid State Phys., **17**, 6287 (1984)

77. Seongil Im, Jack Washburn, Ronald Gronsky, Nathan Cheung, Kin Man Yu, Joel W. Ager, "Optimization of Ge/C Ratio for Compensation of Misfit Strain in Solid Phase Epitaxial Growth of SiGe Layers", Applied Physics Letters, **63**, 2682 (1993)

78. Seongil Im, Jack Washburn, Ronald Gronsky, Nathan Cheung, Kin Man Yu, "Defect Control During Solid Phase Epitaxial Growth of SiGe Alloy Layers", Applied Physics Letters, **63**, 929 (1993)

79. Seongil Im, Jack Washburn, Ronald Gronsky, Nathan Cheung, Kin Man Yu, Joel W. Ager, "Reducing Dislocation Density by Sequential Implantation of Ge and C in Si", Mater. Res. Soc. Symp. Proc., **298**, 139 (1993)

80. Lawrence H. Van Vlack, Materials Science for Engineers, Appendix B, Addison-Wesley Publishing Company, Inc. 1970

81. G. F. van de Walle, L. J. van Ijendoorn, A. A. van Gorkum, R. A. van den Heuvel and A. M. L. Theunissen, Semicon. Sci. Technol., **5**, 345 (1990)

82. L. J. van Ijendoorn, G. F. van de Walle, A. A. van Gorkum, A. M. L. Theunissen, R. A. van den Heuvel and J. H. Barrett, Nuclear Instruments and Methods in Physics Research **B50**, 127 (1990)

83. F. Meyer, M. Zafrany and M. Eizenberg, J. Appl. Phys. **70** (8), 15 (1991)

84. M. Matsuura, J. M. Tonnerre, and G. S. Cargill III, Phys. Rev. B, **44**(8), 3842 (1991)

Appendix

Table 1. Projected range and straggle of Ge^{+} ion in Si

Ion = Ge (Mass = 74)
Target = Si(100 %)
Density = 2.3210E+00 g/cm3
Stopping Units = MeV / (mg/cm2)

Ion Energy	dE/dx Elec.	dE/dx Nuclear	Projected Range	Longitu. Straggling	Lateral Straggling
10.00 keV	2.619E-01	3.983E+00	125 A	48 A	51 A
11.00 keV	2.746E-01	4.076E+00	133 A	50 A	54 A
12.00 keV	2.869E-01	4.159E+00	141 A	52 A	57 A
13.00 keV	2.986E-01	4.234E+00	149 A	55 A	59 A
14.00 keV	3.098E-01	4.302E+00	156 A	57 A	62 A
15.00 keV	3.207E-01	4.363E+00	164 A	60 A	64 A
16.00 keV	3.312E-01	4.420E+00	171 A	62 A	67 A
17.00 keV	3.414E-01	4.471E+00	178 A	64 A	69 A
18.00 keV	3.513E-01	4.519E+00	185 A	66 A	72 A
20.00 keV	3.703E-01	4.603E+00	199 A	70 A	77 A
22.00 keV	3.884E-01	4.676E+00	213 A	75 A	81 A
24.00 keV	4.057E-01	4.738E+00	227 A	79 A	86 A
26.00 keV	4.222E-01	4.792E+00	241 A	83 A	90 A
28.00 keV	4.382E-01	4.839E+00	254 A	87 A	95 A
30.00 keV	4.536E-01	4.881E+00	267 A	91 A	99 A
33.00 keV	4.757E-01	4.933E+00	287 A	96 A	105 A
36.00 keV	4.969E-01	4.976E+00	307 A	102 A	112 A
40.00 keV	5.237E-01	5.021E+00	333 A	109 A	120 A
45.00 keV	5.555E-01	5.063E+00	365 A	119 A	130 A
50.00 keV	5.855E-01	5.091E+00	397 A	127 A	139 A
55.00 keV	6.141E-01	5.110E+00	428 A	136 A	149 A
60.00 keV	6.414E-01	5.120E+00	460 A	145 A	158 A
65.00 keV	6.676E-01	5.124E+00	491 A	154 A	168 A
70.00 keV	6.928E-01	5.123E+00	523 A	162 A	177 A
80.00 keV	7.407E-01	5.109E+00	585 A	179 A	195 A
90.00 keV	7.856E-01	5.084E+00	648 A	196 A	213 A
100.00 keV	8.281E-01	5.050E+00	711 A	212 A	230 A
110.00 keV	8.685E-01	5.012E+00	774 A	228 A	248 A
120.00 keV	9.071E-01	4.969E+00	837 A	244 A	265 A
130.00 keV	9.442E-01	4.924E+00	900 A	260 A	282 A
140.00 keV	9.798E-01	4.877E+00	964 A	276 A	299 A
150.00 keV	1.014E+00	4.829E+00	1028 A	292 A	316 A
160.00 keV	1.047E+00	4.781E+00	1092 A	308 A	333 A
170.00 keV	1.080E+00	4.732E+00	1157 A	323 A	349 A
180.00 keV	1.111E+00	4.684E+00	1221 A	339 A	366 A
200.00 keV	1.171E+00	4.588E+00	1352 A	370 A	399 A

Table 2. Projected range and straggle of C^+ ion in Si

Ion = C (Mass = 12)
Target = Si(93 %) + Ge(7 %)
Density = 2.5322E+00 g/cm3
Stopping Units = MeV / (mg/cm2)

Ion Energy	dE/dx Elec.	dE/dx Nuclear	Projected Range	Longitu. Straggling	Lateral Straggling
10.00 keV	5.165E-01	4.067E-01	299 A	170 A	180 A
11.00 keV	5.353E-01	4.004E-01	326 A	182 A	193 A
12.00 keV	5.530E-01	3.941E-01	354 A	195 A	207 A
13.00 keV	5.699E-01	3.879E-01	381 A	206 A	220 A
14.00 keV	5.860E-01	3.817E-01	408 A	218 A	233 A
15.00 keV	6.013E-01	3.757E-01	436 A	229 A	246 A
16.00 keV	6.160E-01	3.699E-01	463 A	241 A	258 A
17.00 keV	6.302E-01	3.642E-01	491 A	251 A	270 A
18.00 keV	6.439E-01	3.587E-01	518 A	262 A	283 A
20.00 keV	6.698E-01	3.481E-01	573 A	283 A	307 A
22.00 keV	6.942E-01	3.382E-01	628 A	303 A	331 A
24.00 keV	7.172E-01	3.288E-01	682 A	322 A	354 A
26.00 keV	7.391E-01	3.201E-01	737 A	341 A	377 A
28.00 keV	7.599E-01	3.118E-01	791 A	359 A	399 A
30.00 keV	7.798E-01	3.040E-01	846 A	377 A	421 A

LAWRENCE BERKELEY LABORATORY
UNIVERSITY OF CALIFORNIA
TECHNICAL INFORMATION DEPARTMENT
BERKELEY, CALIFORNIA 94720